ON THE EFFECT OF INITIAL CONDITIONS ON RAYLEIGH-TAYLOR MIXING

A Dissertation

by

SARAT CHANDRA KUCHIBHATLA

Submitted to the Office of Graduate and Professional Studies of
Texas A&M University
in partial fulfillment of the requirements for the degree of

DOCTOR OF PHILOSOPHY

Chair of Committee,	Devesh Ranjan
Committee Members,	Kalyan Annamalai
	Junuthula N. Reddy
	Karen Vierow
Head of Department,	Andreas Polycarpou

December 2014

Major Subject: Mechanical Engineering

ABSTRACT

An experimental investigation of the effects of Initial Conditions (ICs) on Rayleigh-Taylor Instability (RTI) is performed using the Water Channel facility at Texas A&M University. Hot and cold water (with a temperature difference of $\sim$ 5-8 °C) selected as working fluids are unstably stratified initially. The resulting Atwood number for this instability is of the order of 10^{-3}. In this dissertation, effect of the composition of the initial perturbations generated by a flapper mechanism is studied. Using the servo controlled flapper system, initial wavelengths are varied between 2-8 cm and phase angles within 0-180°, and the dependence of ensemble averaged mixing width in the linear and nonlinear stages of growth on low Atwood number Rayleigh-Taylor mixing is studied. The Interaction of multiple (up to 11) modes of the IC is studied by varying the wavelengths and phase angles that are generated at the interface of these fluids.

High resolution Planar Laser Induced Fluorescence (PLIF) images of the flow field indicate that changing the phase angle results in the leaning phenomenon, i.e. the leaning of bubbles and spikes with respect to gravitational acceleration, and relative to each other. Experimental measurement of total mixing width, quality of molecular mixing and scalar dissipation rate are performed using ensemble averaging technique. The results indicate that nonlinear mode coupling of the initial modes affects the rate of mixing as well as the transition to turbulence. Molecular mixing measurements indicate that the molecular mixing rate depends upon the ICs. Particle Image Velocimetry (PIV) data indicates that late-time velocity profiles of the mixing layer depend upon ICs. While the density power spectra indicate independence of ICs in the inertial range, the turbulent velocity statistics indicate that

increasing the number of modes of the IC quickens the transition to turbulence. It also results in greater mixing, which reduces the density gradients as the flow evolves with time. Thus, the memory of the ICs is lost sooner with increasing number of initial modes.

DEDICATION

To my family.

ACKNOWLEDGEMENT

First and foremost, I would like to thank my parents and my brother, Atreya for their encouragement and constant support through all these years away from home. I am most grateful to my research advisor, Dr. Ranjan, for his guidance during the past few years and encouraging me to continue for the Ph.D. I am thankful for his support, monetary and otherwise, which were essential for completing this dissertation. I am also grateful to my dissertation committee members, Dr. Kalyan Annamalai, Dr. J. N. Reddy and Dr. Karen Vierow for their valuable input on improving the dissertation, and Dr. Andrea Strezelec for substituting for the final examination at short notice. A special mention of thanks to Dr. Nick Haehn and Dr. Sung-won Moon of Intel, for supporting and mentoring me during my internship at Chandler.

I am indebted to Bhanesh and Jacob for many discussions regarding research and sharing the resources. Last but not the least, many thanks to help from STAML colleagues, Eric, Robert, Sandeep and Tom, without which I could not have completed this assignment. The interactions I had with the STAML group are memorable and enriched my overall experience at Aggieland. This dissertation was funded by LANL (grant # LDRD-DR20090058DR), DOE-NNSA SSAA program (grant # DE-NA-0001786) and TEES.

NOMENCLATURE

A	Amplitude of initial condition
A_t	Atwood number
B_0	Density fluctuation self-correlation for miscible fluids
B_2	Density fluctuation self-correlation for distinct fluids
c	Concentration
C	Constant of proportionality
d	Diameter of probe
D	Diffusivity
f	Volume fraction
Fr	Froude number
g	Acceleration due to gravity
h	Mixing width
H	Height of test section
k	Wavenumber
l	Time delay (lag)
L	Length of test section
(n, N)	Natural numbers
p	Pressure
Pr	Prandtl number
R	Radius
Re	Reynolds number
Sc	Schmidt number
t	Time

T	Temperature
(u, v, w)	Velocity components
U	Convective velocity
W	Width of test section
(x, y, z)	Spatial coordinates

Greek letters

α	Saturation growth rate constant
β	Phase angle of initial condition
γ	Exponential growth rate
δ	Leaning angle
η	Length-scale
θ	Molecular mixing parameter
λ	Wavelength
μ	Dynamic viscosity
ν	Kinematic viscosity
ρ	density
σ	Surface tension
τ	Time-scale
Ω	Vorticity
ω	Frequency

Superscripts

$*$	Non-dimensional value
$'$	Fluctuating component

Subscripts

0	Initial
∞	Asymptotic
b	Bubble
D	Diffusive
eq	Equivalent
fit	Curve fit
h	Heavy fluid
i	Number of initial mode
l	Light fluid
m	Most dominant mode
nd	Non-dimensional
$peak$	Peak
$mean$	Mean value
mix	Mixing
s	Spike
sat	Saturation
v	Viscous

Acronyms

BD	Buoyancy-Drag
BHR	Besnard-Harlow-Rauenzahn
DNS	Direct Numerical Simulation
FFT	Fast Fourier Transform

IC	Initial Condition
ICF	Inertial Confinement Fusion
KHI	Kelvin-Helmholtz Instability
LES	Large Eddy Simulation
LOS	Line Of Sight
LST	Linear Stability Theory
MW	Moving Window
NIF	National Ignition Facility
PIV	Particle Image Velocimetry
PLIF	Planar Laser Imaging of Fluorescence
RANS	Reynolds Averaged Navier Stokes
RMI	Richtmyer-Meshkov Instability
RMS	Root Mean Square
RC	Ristorcelli-Clark
RT	Rayleigh-Taylor
TAMU	Texas A&M University

TABLE OF CONTENTS

LIST OF FIGURES

FIGURE Page

LIST OF TABLES

1. INTRODUCTION

1.1 Motivation

Rayleigh-Taylor instability (RTI) is a buoyancy driven instability observed when $\nabla \mathbf{p}.\nabla \rho < 0$, i.e. when pressure and density gradient vectors are misaligned. The numerical and experimental study of RTI is essential for understanding the physics of fluid mixing in natural phenomena like fluid mixing in river beds, astrophysics and geophysics. RTI is one of the fundamental sources for mixing. As explained in Andrews & Dalziel (2010) (quotation): "RTI plays an important role in the mixing that results from other natural mixing processes where density surfaces are overturned, e.g. Kelvin-Helmholtz Instability (KHI) and breaking gravity waves. Indeed, not only is the mixing efficiency of RTI higher than that of any other known mechanism, but it has been suggested as an explanation for the much lower mixing efficiencies due to shear or mechanical agitation". These flows are characterized by buoyancy, viscosity and diffusion effects, and exhibit a large range of length and time-scales. RTI is widely prevalent in variable density flows such as astrophysical phenomena (see Kifonidis et al. (2006) and Bell & Marcus (1992)), clouds (see Kelley et al. (1976) and Scannapieco & Ossakow (1976)), sand dunes (see Pelletier (2008)), and spray combustion (see Baumgarten (2006)) etc. Therefore, experimental investigation of such flows must be conducted in order to provide comprehensive information for understanding their behavior. The knowledge gained from these experiments will lead the development of better methodologies for applications like Inertial Confinement Fusion (ICF), spray combustion in engines etc.

The significance of RTI in the feasibility and productivity of the ICF experiment (see Lindl & Mead (1975) and Hammer et al. (1999)) warrants a detailed investigation of the underlying physics of RTI. Scientific outcomes of the studies will have a direct impact on the energy efficiency of the ICF, which could be employed as a standard process of power generation in the future. Some ICF studies at the Lawrence Livermore National Laboratories (LLNL) involve the ablation of a micrometer scale Deuterium-Tritium (DT) fuel spherical pellet encased in a Beryllium capsule. Implosion of the capsule using high-energy LASERs deposits a large amount of energy on the resulting plasma, producing shock waves of high strength. These shock waves act upon the surface imperfections of the capsule resulting in Richtmyer-Meshkov Instability (RMI). Thus, at the initial stages of the fusion process, RMI arising due to impulsive acceleration dominates the flow physics. It was shown using simulations of Schmitt et al. (2001) that RTI dictates flow physics after certain levels of acceleration. RM and RT induced mixing of the Beryllium capsule with the DT fuel results in degradation of fuel quality and affects the yield of the experiment. Thus, RTI has a significant role in feasibility and efficiency of the ICF. Of special interest is the effect of initial perturbations on the evolution of RTI and resultant mixing behavior. The effect of initial conditions on Rayleigh-Taylor mixing must be studied so that mixing of the fuel with other materials in the ICF experiment can be understood. The density gradient is characterized by Atwood number, A_t, given in Eqn. 1.1, where ρ_h is the density of the heavy fluid and ρ_l is the density of the light fluid.

$$A_t = \frac{\rho_h - \rho_l}{\rho_h + \rho_l} \tag{1.1}$$

Shown in Fig. 1.1 is a 2D schematic of the National Ignition Facility (NIF) scale ignition double-shell design from a HYDRA simulation. Details of this simulation can be found in Milovich et al. (2006). In the figure, a cross section of the capsule after the pellet is impinged upon by high energy lasers is depicted. Various material interfaces between the outer Beryllium (Be) capsule and the inner DT fuel, and the resulting finger shaped structures characteristic of RTI are observed. The simulation was initialized using small wavelength multi-mode initial perturbations at the interfaces.

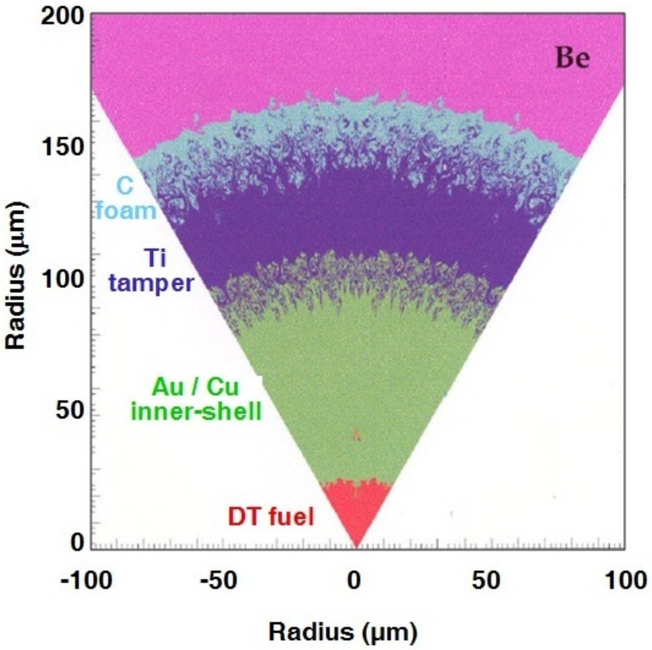

Figure 1.1: 2D cross section of the **Be** encased Deuterium-Tritium fuel pellet from simulation. Figure reproduced from Milovich et al. (2006).

Motivated by the significance of RTI in the ICF application, studies are being performed to study RTI in detail so as to consolidate the scientific community's understanding, and develop a generalized theory that explains and quantifies the underlying physics. An earlier theory by Youngs (1984) and experiments of Snider & Andrews (1994), Dimonte (2000), Waddell et al. (2001) and Huang et al. (2007) establish a self-similar behavior of the fluid at late-times of Rayleigh-Taylor evolution. Recent studies by Dimonte (2004), Olson & Jacobs (2009) and Ramaprabhu &

Dimonte (2005) have suggested that the memory of initial condition persists in the flow even at late-times. This dissertation aims at experimentally investigating the effects of initial conditions (ICs) on the development of RTI in a two-fluid scenario using the Water Channel facility at Texas A&M University.

1.2 Theoretical background

This section gives a working background of RTI, which is observed when a heavier fluid is placed over a lighter fluid in the presence of acceleration. This acceleration could be due driven by gravity, but if the acceleration is impulsive and external such as due to shocks, it is called Richtmyer-Meshkov instability. If the two-fluid interface is accelerated due to shear applied between the fluids, such an instability is called Kelvin-Helmholtz instability (KHI). In RTI, at a given fluid interface with a known density gradient, baroclinic vorticity is initially deposited due to misalignment of the density and pressure gradients ($\nabla \mathbf{p} . \nabla \rho < 0$) where p is the local pressure and ρ is the density of the fluid (see Chandrasekhar (1961)). This can be witnessed in the vorticity equation given in Eqn. 1.2, where vorticity generation due to density stratification can be treated as a source term on the right hand side. Here, $\mathbf{U}$ is the velocity vector and $\mathbf{\Omega}$ is the vorticity vector.

$$\frac{D\mathbf{\Omega}}{Dt} = \nu \nabla^2 \mathbf{\Omega} + \mathbf{\Omega} . \nabla \mathbf{U} + \left(\frac{\nabla \rho \times \nabla \mathbf{p}}{\rho^{\mathbf{2}}} \right) \tag{1.2}$$

The additional term, $\frac{\nabla \rho \times \nabla p}{\rho^2}$ is called the baroclinic vorticity term and is non-zero for a density stratified fluid configuration. The viscous term, $\nu \nabla^2 \mathbf{\Omega}$ and vortex stretching term, $\mathbf{\Omega} . \nabla \mathbf{U}$ are also observed. At time $t = 0$, as viscous effects are negligible, this term drives the velocity field. Figure 1.2 demonstrates baroclinic vorticity generation due to misalignment of the pressure and density gradients.

The schematic shows an initial sinusoidal interface formed due to the stratifica-

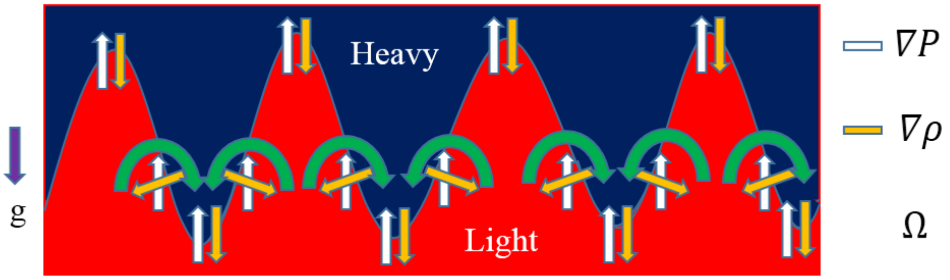

Figure 1.2: Baroclinic vorticity deposition at a two-fluid interface.

tion of heavy fluid atop a light fluid. At the interface, baroclinic vorticity deposition due to the density gradient is also shown. The deposition is strongest where the gradients of pressure and density are perpendicular to each other. An initial perturbation with a small amplitude to wavelength ratio starts to grow under the action of acceleration due to gravity. With this, the interface stretches and vorticity spreads across a larger region. In the current dissertation, perturbations are classified based on the number of modes involved, which is basically the number of wavelengths that compose the perturbation, and the phase difference between the modes. As the flow evolves towards turbulence, a range of wavenumbers and frequencies typically seen in turbulent flows can be observed. At larger wavenumbers, microscopic processes such as molecular diffusion and viscosity become significant in the system in comparison to inertia. Thus, much smaller length and time-scales are observed at late-time.

Each perturbation that is input at the interface at time $t = 0$ grows exponentially according to Linear Stability Theory (LST) by Chandrasekhar (1961) and eventually the growth rate of the perturbation saturates to a terminal velocity. An extensive analysis of various phases of perturbation growth was given by Youngs (1984). The perturbation evolves through four different phases, namely *i*) Exponential regime, where the instability grows exponentially in time, where LST is valid.*ii*) Linear regime, where the acceleration of the interface slows down to a constant.*iii*) Mode coupling or bubble competition, where the adjacent structures compete for evolving dominant wavelengths.*iv*) Saturation regime, where the terminal velocity is achieved and the mixing layer grows parabolically with time.In the linear regime, assuming negligible viscous forces, the growth rate of the most dominant mode is given by Chandrasekhar (1961) as:

$$\gamma_m = \frac{\pi g \left(\rho_c - \rho_h\right)}{l_m \left(\rho_c + \rho_h\right)} \tag{1.3}$$

Here, γ_m is the growth rate of the most dominant mode, whose wavelength is η_m, and g is the acceleration due to gravity. Transition to the nonlinear regime occurs when the linear velocity of a bubble or spike equals the saturation or terminal velocity of the structure. This is when the height of the structure, h equals the wavelength of the perturbation, λ. As the dominant mode evolves into the nonlinear regime, terminal velocity, v_{sat}, for a dominant wavelength is given by Daly (1969):

$$v_{sat} = C_\infty \left(\frac{\left(\rho_c - \rho_h\right)}{\rho_c} g R_b \right)^{0.5} \tag{1.4}$$

where R_b is the bubble radius and C_∞ is a constant. In Rayleigh-Taylor nomenclature, ‘bubbles’ are defined as the typical, cylindrical interfacial projections of the lighter fluid into heavier fluid, while ‘spikes’ are projections of the heavier fluid into the lighter fluid. These bubbles and spikes have characteristic mushroom shape with a neck, rounded tip and a pair of counter rotating vortices emanating from the tip on either side. At low A_t, bubble and spike growth are symmetric, with $C_\infty \approx 0.7$. For the current Water Channel experiments, as the Atwood number is very small, bubble and spike growth rates are highly symmetric. After the nonlinear regime, due to mode coupling, the bubble and spike growths saturate and a self-similar behavior of the mixing layer is observed, and the mixing is described by a similarity solution as given in Eqn. 1.5. Mode coupling is defined as the nonlinear interaction of component modes, which result in the generation of dominant modes. At this stage, since the memory of initial conditions is lost, a quadratic growth of the mixing layer half width, h_{sat} was proposed by Youngs based on dimensional analysis:

$$h_{sat} = \alpha A_t g t^2 \tag{1.5}$$

Here, α is the saturation growth rate constant and t is the time from initialization. Based on many numerical and experimental studies (see Snider & Andrews (1994), Dimonte (2000), Waddell et al. (2001) and Huang et al. (2007)), researchers have come up with different values of α, within a generally accepted range of 0.03-0.1. Details of the different values of α obtained by various studies are given in the literature review, §2. The total mixing width, h, is defined by:

$$h = h_b - h_s \tag{1.6}$$

where h_b is defined as height of the bubble specified at each location where the volume fraction of mixture is 0.95:

$$f_h = \rho^* = \frac{\rho - \rho_l}{\rho_h - \rho_l} = 0.95 \tag{1.7}$$

and h_s is defined as the height of the spike given by $f_h = 0.05$. At late-times, viscous forces becomes predominant and the flow becomes fully turbulent. Various stages of the interface are shown in Fig. 1.3, displaying mushroom shaped ‘bubble’ and ‘spike’ structures characteristic of RTI flows. Secondary structures generated due to KHI, which is a secondary phenomenon, can also be observed.

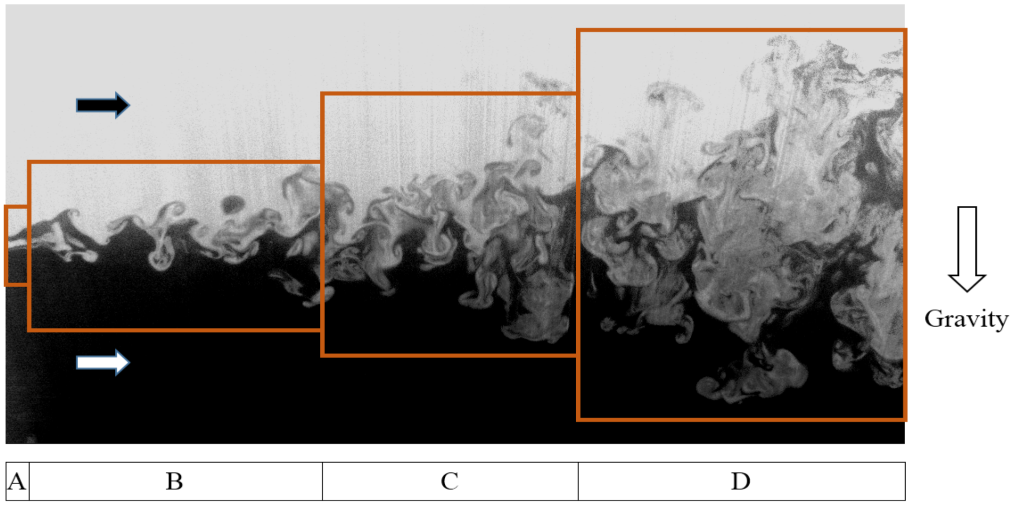

Figure 1.3: Regimes of RTI in Water Channel. (A) Linear growth rate, (B) Nonlinear growth rate, (C) Transition and (D) Turbulence. These regimes are for illustration purposes only, and are not supported by any measurements. The transition to turbulence and nonlinear growth growth rate of the mixing layer may not be observed simultaneously. The fluids mix initially due to diffusion of the hot and cold water. The water streams convect from left to right in the PLIF image above. The top (colder) stream is dyed with Rhodamine, which fluoresces when exposed green light.

Figure 1.3 shows an image of RTI in Water Channel without any flapper motion. The test section with dimensions of 48 in×13 in is visualized. The fluid streams are initially separated by a splitter plate, which is not shown in the figure. Gravitational force accelerates this unstable configuration continuously, enhancing mixing, and stretching and folding the fluid interface with time. The diffusive region is very small compared to the other regions shown in the figure. The LST can be employed to find the most unstable or dominant wavelength in the linear growth rate regime. In the nonlinear regime, mode coupling of the component modes of the IC results in a nonlinear growth rate. The current dissertation aims to study and understand this regime in more detail, by controlling the initial condition, specifically, the initial perturbation, and observing the resultant mixing behavior. The flow eventually evolves to turbulence, showing a wide range of eddy sizes and velocities.

The Water Channel system is a convective setup devised to study the statistically steady behavior of liquid mixing. On the other hand, many experimental setups in literature use the 'box' type RTI setup, in which the fluids are initially at rest and unstably stratified using a certain type of interface separator, that is removed very quickly at the start of the experiments. However, the box type of setups have a challenge with the separator removal, while the Water Channel lacks this challenge owing to its convective nature. One difficulty with the Water Channel setup is that the mixing behavior in a convective system might be dependent upon mean convective speed of the fluid streams. This requires a clear understanding of the effect of convection on the mixing layer. In general, low Atwood number experiments correspond to large experimental observation times. In the Water Channel, the fluid can be visualized for about a total time of about 22-26 s, which is large compared to the largest time-scale of the system. A major advantage with the Water Channel setup is the use of water as working fluid, which significantly reduces the cost of experiments. Several experiments can be performed using full tanks (of 500 gallons capacity each) of hot and cold water. The difficulty in using water as working fluid lies in the low Atwood number achieved, as well as in repeatability of achieving the Atwood number in multiple runs of the experiments. However, in the low Atwood number regime, the RT mixing follows established theory well, and any variations in Atwood number can be incorporated into theory.

1.3 Outline of dissertation

Motivated by the need to study effects of ICs on RTI, an experimental approach using the Water Channel setup equipped with a flapper mechanism is reported here. The outline of the current dissertation is as follows: *a*) A detailed literature review is provided in §2. From the review, aspects of RTI needing further research are identified. *b*) §3 describes the experimental setup and diagnostic techniques employed, including high resolution imaging, thermocouple measurement, PLIF and PIV. *c*) A description of the IC is provided in §4.4.1. *d*) A discussion of the results of these experiments is provided in §4. As several types of analyses are performed on our experimental data, the results are organized by the nature of diagnostic technique employed. *i*) The initial discussion is on the effect of flapper motion when compared with RTI without flapper motion. Flow evolution due to single-mode flapper motion and its effect of mixing parameters is provided in §4.4. *ii*) After gaining a thorough understanding of the effect of the flapper, a study of the effect of variation of phase angle and number of modes of the ICs for up to 3 modes is performed. Using Line Of Sight (LOS) imaging and the ensemble averaging technique, variation of large-scale mixing behavior is reported in §4.2. *iii*) Point-wise density data is extracted and analyzed in §4.3. This section describes the variation of mixing at fine-scales. *iv*) Using PLIF imaging, planar images of the flow are obtained, and a study of large and small scale mixing is reported in §4.5. *v*) To understand the effect of ICs on the development and statistical behavior of Rayleigh-Taylor turbulence, velocity fields obtained using PIV are analyzed and reported in §4.7. By increasing the number of initial modes (up to 11) and by varying the shape of the initial modal distribution (from single-mode to broadband type), valuable insight is gained into the dependence of Rayleigh-Taylor turbulence on the ICs. *e*) A summary of the results is provided in §5. *f*) Additionally, the appendix provides validation and calibration studies performed as a part of this dissertation.

2. LITERATURE REVIEW

Some of the discussion in this section is previously presented in the Masters' Thesis by the author Kuchibhatla (2010). The objective of this section is to understand previously documented research on RT mixing and summarize it. As there is a vast amount of literature on this topic since GI Taylor's experiments in 1951, only some of the relevant and significant literature is reported here. This section provides the literature review of the research previously performed at Texas A&M University and various other facilities around the world. Since a large number of experiments were performed at Texas A&M University over the past years, §2.1 details those experiments using the Water Channel to give a complete overview of the past, present and future of research using the facility with an additional discussion of the uncertainties in these experiments. §2.2 details the relevant research performed at all other locations.

2.1 Literature review of TAMU Water Channel experiments

A list of significant experimental studies performed at Texas A&M University is given here. Two of the main advantages of performing experiments using the Water Channel are the large data collection time and the statistically steady nature of the flow. The size of the facility is also comparatively larger than many RTI facilities, providing a unique capability to observe the flow at higher mixing Reynolds numbers. Thus, the fully turbulent regime can be studied and statistics quantified. The precursor to the current study is the work of Leicht (1997), who studied the effect of binary-mode initial conditions on RTI by studying ensemble averaged mixing characteristics. The binary-mode initial conditions were generated using two variable speed electrical motors which were coupled eccentrically to produce the required phase shift between the modes. Varying the speed of the motor produces required wavelengths, and changing the eccentricity produced the desired phase shift. The difficulty with this setup lies in maintaining a constant phase angle. The phase shift was found to vary during experiments, which is rectified in the present dissertation using a highly controllable servo motor. Mueschke (2004) experimentally measured the initial density and velocity perturbations at the two-fluid interface and performed a parametric study using Direct Numerical Simulation (DNS) approach. He observed that combined effect of the splitter plate and the edge mesh geometries introduced larger wavenumbers into the flow as compared to smaller initial wavenumbers present at the interface. Spanwise velocity fluctuations at the interface were found to be negligible. Molecular mixing at the center plane was decreasing with time, around $t^* = 0.3$, where t^* is defined as the non-dimensionalized time given by

$$t^* = t\left(\frac{A_t g}{h}\right)^{0.5} \tag{2.1}$$

Kraft (2008) studied the effect of a buoyant wake off a cylinder aligned with the horizontal center plane of the Water Channel. PLIF and PIV were employed to measure density and velocity fluctuations at various streamwise locations to study wake interaction with buoyancy driven mixing layer. A mathematical model to describe the decay of vertical velocity fluctuations in the wake region of the RTI was also formulated. Peart (2008) has performed experiments to study the effect of grid generated initial conditions on RTI in the Water Channel facility. Fine, medium and coarse grids with high solidity ratio were chosen and it was observed that the self-similar growth constant, α, decreased with increasing grid size. PIV was used to measure statistical velocity data and the same initial conditions from experiment were input into a numerical model that uses the Besnard, Harlow, Rauenzahn (BHR) model of turbulent transport (see Besnard et al. (1996)). The experiments and numerical simulation results were found to be in agreement in the self-similar region of the flow. Experimental studies on mixing behavior in RTI, KHI and combined KH-RT mixing layers using the Gas Tunnel facility are being performed at TAMU. These experiments are characterized by high Atwood number created using convective streams of pure air and an air-Helium mixture. Details of the Gas Tunnel experiments are provided in Banerjee & Andrews (2009), Kraft (2008) and Akula et al. (2013).

2.2 Literature review of other studies

As described in §2.1, this section provides the review of the research previously performed at various other facilities around the world. The following survey explains the analytical, numerical and experimental advancements and their outcomes. It provides a basic understanding of RTI and a comparison of the mixing characteristics in various studies.

2.2.1 Analytical theories

This section deals with the chronological survey of analytical theories on RTI. Historically, RTI growth due to gravity was first studied theoretically by Lord Rayeligh (1883) and experimentally by Taylor (1950). Chandrasekhar (1961) proposed a linear theory for the development of the interface of two fluids acted upon by acceleration in a direction perpendicular to the interface. This is called the Linear Stability Theory (LST). Based on the experiments conducted by Taylor (also see Lewis (1950)), LST was deemed valid until the amplitude of the modes reaches 0.4 times the wavelength of the mode. The experiments were conducted for a wide variety of density ratios and varying accelerations of the fluid interfaces. Taylor also observed a terminal velocity proportional to the difference in acceleration of the fluid interface and the acceleration due to gravity. However, much of the analysis assumes a potential flow condition, neglecting the effects of vorticity and viscosity at earlier times.

Since the seminal papers of Lord Rayleigh and Taylor, many theories were proposed to lay a foundation for RTI. Analytical theories have provided an idealized, simplified understanding of the problem, and pointed to the shortcomings that need to be further investigated. Layzer (1955) proposed a theory for shape of the fluid interface using a 2D, inviscid, incompressible analytical model. He formulated a stream function for fluid flow within a cylindrical tube due to a sudden removal of an initially perturbed diaphragm at initial time. The fluid velocity at the tip of the diaphragm was calculated and a stream function was formulated corresponding to this velocity. This velocity was found to saturate as a function of radius of the cylinder. Effect of the wall on the flow on a periodic array of cylinders is then calculated and the solution was still found to be valid. Therefore, he surmised that the shape of a typical fluid interface in RTI can be considered as an array of cylinders, and that viscosity and surface tension stabilize the interface. He also observed that interfaces with initially larger amplitudes grow faster but the interfaces with initially smaller amplitudes last longer. The number of bubbles will continually diminish and only the largest wavelengths remain. However, this approach assumed a stream function formulation and a cylindrical shape for the bubbles and spikes, which is found to have a large deviation from the mushroom shaped bubbles and spikes in reality. Goncharov (2002) proposed an analytical model for RTI bubble and spike velocities for the different regimes by using a velocity potential formulation. This model provided a continuous bubble evolution theory from linear to nonlinear regime whereas the Buoyancy-Drag models calculated only asymptotic behavior.

An idealized analytical model proposed by Mikaelian (2003) predicted bubble amplitudes for arbitrary A_t by improving upon Layzer's work. Growth rate in the non-linear regime was analytically integrated using 2D and 3D approaches and a linear variation of growth rate (defined as time rate of change of bubble or spike amplitude, $\frac{dh}{dt}$) was reported in the linear regime. An asymptotic growth rate was reported at late-times. This model was in agreement with models by Fermi et al. (1955), Oron et al. (2001) and Goncharov (2002). Abarzhi et al. (2003) proposed multiple harmonic nonlinear theoretical solutions to account for vorticity generation and secondary instabilities (e.g. KHI). They observed that for smaller initial perturbations, most of the energy is contained in large-scale structures and vice-versa by correlating bubble curvature (defined as $\frac{d^2h}{dt^2}$) to A_t. Their solution matched well with asymptotic bubble curvatures by Alon et al. (1995) and Layzer (1955). For low A_t, bubble curvature flattens out, and saturated bubble and spike velocities are reduced. This theory placed importance on bubble curvature, and experimental data might corroborate their conclusions. Another analytical theory by Dimonte (2004) proposed a general theory for bubble and spike growth for all A_t as dependent on Froude number, Fr, (defined by $Fr = \frac{v_b}{2NR}$ where v_b is the velocity of bubble or spike, N is the characteristic buoyancy frequency and $2R$ is the diameter of bubble or spike) which depends on the shape of the bubble and its environment. Nonlinear coupling of modes was found to have insignificant effect on the growth of broadband initial perturbations. Wavenumbers $k > k_p$ (k_p is the peak wavenumber corresponding to peak growth rate) dominate eventually, and growth rate was found to vary as $\sqrt{A_t g k}$. Terminal velocity calculations were found to be a dependent on A_t, whereas theories by Sohn (2003, 2009) proposed them to be independent of A_t. This is because Atwood number affects the shape of the mushrooms, which in turn affects Fr. Also larger wavenumbers were found to grow faster than smaller wavenumbers, whereas larger wavenumbers saturate faster. Modes closest to the peak or dominant wavenumber grow fastest. Saturation velocities were also computed by setting the growth rates to zero.

2.2.2 Numerical simulations

To account for the shortcomings of analytical theories, numerical simulations were extensively performed and benchmarked with experimental data. Two major theories were proposed to explain observed bubble and spike interactions, namely "Competition" models and "Buoyancy-Drag" (BD) models. Whereas competition or merger models attribute adjacent bubble and spike interactions to explain growth, BD models predict growth rates based on the effective drag on the bubbles and spikes at different regimes of flow development. Some of the major simulations concerning initial conditions and their effects on RTI behavior follow based on complexity of the simulation, i.e. relatively simpler models are listed first.

Freed et al. (1991) have conducted numerical simulations of RTI in the self-similar turbulent regime by taking the 1D incompressible, two-phase model of Youngs (1984) as a starting point and modifying to an Arbitrarily Lagrangian Eulerian (ALE) code. Small amplitude, multi-mode, random noise is applied as initial perturbation and the interface was explicitly tracked. The authors observed a non-dimensional combination of scales and density ratio resulting in a self-similar behavior of the fluid at late-times. Bubble growth rate was found to follow $\alpha A_t g t^2$ whereas considerable numerical noise was observed at the spike tips. Alon et al. (1995) performed 2D numerical simulations of multi-mode RTI by modifying Layzer's theory and observed self-similar bubble and spike growth rates. Power laws for different Atwood numbers were formulated for single-mode sinusoidal initial perturbations imposed on an incompressible flow hypothesis. They proposed that the spike velocity is reduced because of the formation of a rounded-head, which reduces its drag and bubbles grow faster because of a smaller area to volume ratio, i.e. smaller drag. They have also performed simulations with binary-mode initial conditions and reported the following: *i*) For times less than the scale invariant time-scale, which depends on the initial perturbation, any two neighboring bubbles rise independently. *ii*) Later, the larger bubbles expand faster and smaller bubbles are swept in their wake. *iii*) For times much greater than the scale invariant time-scale, an asymptotically periodic array of bubbles and spikes twice the dominant wavelength remains. This bubble competition process is longer for smaller dominant wavelengths as compared to larger ones. The dependence of bubble and spike height at late-times on the wavelength of the initial perturbations for all Atwood numbers is consistently observed. Abarzhi et al. (2003) have studied the dimensional dependence of RTI and RMI on late-time scaling laws in their numerical, 2D and 3D simulations using a BD model. They imposed a multi-mode initial condition with about 300 bubbles and improved upon the previous work by Alon et al. (1995). The dominant wavelength, λ_m, is defined differently as the length of a sample box cross section divided by the number of bubbles present inside the box. Their 3D model predicts increased rates of drag force on the structures and merger of the structures. The growth rate constants, α are smaller than literature. Bubble velocity depends on the dominant bubble size and spike velocity is dependent on bubble motion. It was observed that bubbles reach saturation quicker compared to spikes. These variations are dependent upon the IC, studies of which follow.

Numerical studies using single-mode IC by Dimonte (2004) and Ramaprabhu & Dimonte (2005) showed that although the largest wavelength dominates the initial stages of growth, the nonlinear stage is governed by the largest modes arising out of coupling of the modes. Mode coupling data, especially with regard to the ratio of wavelengths and the phase angles between the initial modes will provide an essential understanding of the nature of interaction of RTI structures and the ensuing mixing process. Researchers such as Steinkamp et al. (1999) and Ristorcelli & Clark (2004) studied the anisotropy of RTI for low Atwood numbers, specifically in the turbulent stage. Livescu et al. (2009) reported DNS of RTI at high Reynolds numbers in the self-similar and turbulent stages. They reported that the larger scales of the simulation are anisotropic, whereas the smaller scales are isotropic. In their self-similarity DNS study of Ristorcelli & Clark (2004), molecular transport effects were ignored, while dissipation effects were included. The point of note here is that numerical simulations and experimental data have not yet attained congruence on the nature of turbulence in RTI flows when compared with classical turbulence (See Abarzhi (2010) for details). Recently, Rollin & Andrews (2010) modeled the effects of initial conditions on RTI using their two-fluid model and compared with results from RTI3D code. They proved the capability of the code in capturing trends in BHR parameters described in Besnard et al. (1996), given an initial broadband spectrum. One of the challenges of these models and simulations lies in their inability to account for mode-coupling, which will need reliable experimental data for validation. To summarize, a better understanding of RTI turbulence would require experimental data on the mode-coupling, molecular transport effects and the flow evolution in the turbulent stage. Studies by Wei & Livescu (2012) reported reacceleration of the bubbles at sufficiently large Reynolds numbers. Although the regimes of RTI depend upon the Reynolds number, the initial shape of the interface had insignificant effect on the asymptotic bubble velocity. From these studies, it can be noted that experimental data regarding molecular transport in miscible fluids will aid numerical simulations in order to improve modeling the physics of the RTI problem. Similarly, validation of Implicit Large Eddy Simulation (ILES) simulations for different ICs is performed by Lim et al. (2010). In their study, the discrepancy in α between experiments and numerical simulations is attributed to the presence of large wavelengths in the experiments, as well as due to numerical mass diffusion. Therefore, the current study provides the diffusion mixing data in a miscible fluid scenario, which can be used to validate codes, such as reported in Glimm et al. (2011) and Andrews et al. (2012). Apart from the above, turbulent models such as by Steinkamp et al. (1999), which use two-point formulations, or by Wilson & Andrews (1999), which use the Reynolds Averaged Navier Stokes (RANS) approach, require the tuning of model coefficients with experimental data for better performance of their models. Therefore, PIV measurements of Reynolds stresses from Water Channel experiments will provide validation for the above codes.

2.2.3 Experiments

Fewer experimental campaigns were performed in the past to study the effect of initial conditions on RTI. Dimonte (2000) and Dimonte & Schneider (1996) used their Linear Electric Motor (LEM) facility to perform these experiments over a wide combination of A_t and acceleration profiles. The experiments employed natural initial perturbations at the interface corresponding to the range 0.1-1 mm and the meniscus of the fluid-solid interaction at enclosure walls served as a source of initial perturbation for some of the experiments. The projectile, which is basically the fluid container that slides along magnetic rails, is controllably accelerated to generate RTI. Observed acceleration profiles had an earlier steep rise and a plateau which are about 90% accurate. Bubble and spike displacements as a function of density ratio of the fluids and self-similar growth rate constant, α were reported. Average diameters at the mixing front location were also reported.

Carles et al. (2006) and Huang et al. (2007) have studied magnetic levitated RTI with specific initial conditions using two immiscible fluids in a Hele-Shaw cell and developed a theoretical model for the same. Here, the fluid interface is stabilized until

$t = 0$ and the magnetic field is suddenly removed, so that density stratification results in RTI. The novelty of their experimental setup is the stabilization of the unstable two-fluid interface in specific sinusoidal shapes for $t < 0$ using the paramagnetic nature of the denser fluid. From these experiments, it was found that fluids of different viscosities behave like a fluid of almost same density averaged viscosity for RTI purposes. Applying single-mode initial conditions at the interface, it was observed that the measurements are in close agreement with LST. Also, measured saturation growth rate constants, α were found to vary from 0.06-0.07 depending upon the wavelength, λ. Waddell et al. (2001) have experimentally studied low A_t RTI with single-mode initial perturbations generated by oscillating the experimental test Channel at a specified frequency. Using PLIF and a high-speed camera that traverses along with the test Channel, they have measured amplitudes of bubble and spikes with time. Their measurements were found to be in good agreement with LST in the early phases and were found to have relatively constant terminal velocities for the bubbles and spikes. Experiments with nearly single-mode and up to 14 wavelengths were performed by Olson & Jacobs (2009). A time-scale suggested in Cabot & Cook (2006), that takes the wavelength into consideration was used to define their RTI stages. While their discussion focused on the shape of the α curve and its asymptotic value, they have observed that decreasing single-mode wavelength decreased asymptotic α because of the shorter time required for saturation. A list of previous research on RTI is given in Table 2.1.

Table 2.1: Literature review of relevant research on RTI. NR means not reported.

#	Reference	A_t	IC type	Methodology	Observations
1	Andrews et al. (2012)	0.5-0.9	Titled rig	Numerical simulation	Calculated molecular mixing parameters and compared with experiments
2	Banerjee & Andrews (2006)	0.035-0.1	RTI and KHI	Experiments	Using Gas Channel, studied mixing behavior
3	Banerjee & Andrews (2009)	0.5	3D RTI	Numerical simulation	Effect of ICs explored using RTI3D code
4	Banerjee et al. (2010)	0.04	Diffuse	Numerical simulation	Evaluated BHR turbulence model for RTI
5	Boffetta et al. (2009)	0.025	Diffuse	Numerical simulation	Observed late-time RTI turbulence
6	Buch & Dahm (1996)	NR	Diffuse	Experiments	Study of fine-scale turbulent structures through scalar dissipation measurement
7	Cabot & Cook (2006)	0.2-1	Diffuse	DNS simulation	Studied evolution of RTIas a function of Reynolds number and Atwood number

Table 2.1 Continued

#	**Reference**	A_t	**IC type**	**Methodology**	**Observations**
8	Carles et al. (2006)	0.027	Planar	Experiments	Measured growth rates of single-mode magnetically levitated RTI
9	Cheng et al. (2000); Cheng & Scannapieco (2005)	0-1	Planar	Theory & Numerical simulation	Simulated density dependence of RTI mixing behavior and developed BD mix model
10	Chung & Pullin (2010)	0.5-0.75	Planar	DNS & LES	Studied late-time flow behavior and scaling
11	Cook & Dimotakis (2001); Cook & Zhou (2002)	0.5	Planar	Theory & DNS	Based on DNS data, identified scaling laws for transition to turbulence, and a discussion of energy deposition in RTI
12	Dalziel et al. (1999)	$2{\times}10^{-3}$	Planar	Theory & experiments	Studied the self-similar behavior of RTI

Table 2.1 Continued

#	**Reference**	A_t	**IC type**	**Methodology**	**Observations**
13	Danckwerts (1952)	NR*	NR	Theory	Quantified the amount of molecular mixing in miscible and immiscible fluids
14	Dimonte (2000, 2004)	0-1	Planar	Theory & simulations	Studied dependence of RTI on ICs, and employed the BD model to explain the observations
15	Doron & Duggleby (2011)	$O(10^{-4})$	Single-mode	Experiments	Measured mixing width using single-mode IC experiments on the Water Channel
16	Goncharov (2002)	1	Single-mode	Theory	Presented a theory on growth rate of bubbles and spikes based on potential flow model
17	Huang et al. (2007)	0.2-1	Single-mode	Experiments	Using single-mode IC, studied mixing behavior for paramagnetic working fluids
18	Ikegawa & Nishihara (2003)	NR	NR	Theory	Study of interaction of adjacent mode interaction in the saturation regime
19	Layzer (1955)	NR	Cylindrical	Theory	Based on a potential flow model, proposed a theory for growth of RTI interface

Table 2.1 Continued

#	**Reference**	A_t	**IC type**	**Methodology**	**Observations**
20	Rayeligh (1883); Lewis (1950); Taylor (1950)	0.10-1	Planar	Theory & Experiments	Pioneered the study of RTI with variable acceleration
21	Lim et al. (2010)	0.333	Planar and multi-mode	Numerical simulations	Studied mode coupling of RTIinitial modes, and simulated molecular mixing
22	Linden & Redondo (1991); Linden et al. (1994)	1×10^{-4}-5×10^{-2}	Planar	Theory & Numerical simulations	Molecular mixing in RTI
23	Livescu et al. (2010, 2011); Livescu & Wei (2012)	0-1	Planar	DNS	Dependence of RTI on Atwood number, gravity, IC simulated and studied behavior at several stages
24	Marinak et al. (1998)	1.0	3D multi-mode	Numerical simulations	Nonlinear behavior observed

Table 2.1 Continued

#	**Reference**	A_t	**IC type**	**Methodology**	**Observations**
25	Milovich et al. (2004)	1.0	Multi-mode small amplitude ICs	Numerical simulations	For ICF experiments, effect of IC studied
26	Waddell et al. (2001); Olson & Jacobs (2009); Tsiklashvili et al. (2012)	< 0.1	Single and multi-mode, arbitrary ICs	Experiments	Using paramagnetic fluids and arbitrary single, multi-mode ICs, saturation behavior of mixing layer studied
27	Ramaprabhu & Andrews (2003); Ramaprabhu et al. (2005)	10^{-4}-10^{-3}	Default modes of Water Channel	Experiments	Using optical diagnostics, measured density and velocity for Water Channel without flapper
28	Read (1984)	0.23-1	Planar	Experiments	Using rocket-rig setup, measured growth of RTI with variable gravitational acceleration

Table 2.1 Continued

#	**Reference**	A_t	**IC type**	**Methodology**	**Observations**
29	Snider & Andrews (1994, 1995)	10^{-4}-10^{-3}	Planar	Experiments	Design and validation of the Water Channel setup equipped with optical diagnostics, for mixing measurement
30	White et al. (2010)	0.46-0.99	Single-mode	Experiments	Using single-mode ICs in paramagnetic fluids, observed immiscible RTI mixing
31	Youngs (1984, 1989, 1994)	0.5-0.9	Single-mode	Numerical simulations	Self-similar behavior of RTI presented

2.2.4 Summary of literature review

To understand the present state of the art of Rayleigh Taylor instabilities, recent work by Abarzhi (2010) is cited (quotation): "Despite significant efforts, the universality of scaling $\frac{h}{gt^2}$ and $\frac{\lambda}{gt^2}$ and the mechanism of mixing process in RT flow still remain open issues". Thus, a need to study details of the saturation regime with regard to the growth rate constant, α and its universality, exists. Similarly, another recent work by Andrews & Dalziel (2010) mentions the importance of low Atwood number experiments with varying conditions as follows: (quotation). "There is still to be more research to be done for small Atwood number RT involving shear and buoyancy, the effects of initial conditions, higher Reynolds number, high Schmidt number effects and cross coupling with chemistry heat release". The above statements emphasize the importance of the present experiments in this campaign in regard to the enhancement of the knowledge of the scientific community.

From the literature review discussed above in §2.1 and §2.2, the current state of the art in RTI is as follows: *i*) Analytical theories were the starting point of RTI analysis. They are simplified, idealized and cannot account for the complex behavior of RTI. *ii*) Some of the theories on RTI have considered the shape of the fluid interface and bubble and spike curvature to describe the evolution of the instability in the linear and nonlinear regimes. *iii*) Many numerical simulations were performed with varying degrees of accuracy and complexity, but congruence with experiments is not established yet. *iv*) The effect of initial conditions were studied in detail, but the effect of initial perturbations on saturation and growth rates is unclear for all Atwood numbers. Growth rates were found to vary from study to study. *v*) Bubble and spike velocities also vary depending upon the model employed for solution and the 2D or 3D nature of the solution domain. *vi*) More experimental data is needed to observe the dependence of multi-mode structures, their competition and growth of the component single-modes.*vii*) The onset and growth characteristics of self-similarity are still to be clarified. Memory effects have to be studied to understand the chaotic or deterministic nature of turbulence. *viii*) Experiments have provided data for validation of some of the numerical models. Multi-mode experiments with controllable initial conditions need to be performed for a range of Atwood numbers such that the physics of the problem can be understood.

2.3 Aspects needing further research

Based on the above literature review, the following questions about RTI require clarification or explanations:

1. The growth of an instability into turbulence involves the constant development of new modes arising out of the interaction between initial modes, until a very large number of modes is attained at very late-times, i.e. until the wavelength decreases to the Kolmogorov scale, because of the nonlinear nature of the governing Navier-Stokes equations. To better understand this evolution pattern, the following activities can be performed:
   (a) A study of modal interaction at early-times might be performed using the Water Channel setup. Using a set of experiments with varying ICs, density data can be used to study the mixing behavior dependence on modal interaction in the nonlinear regimes.
   (b) A study of the total mixing (diffusion + due to velocity fluctuations) as well as diffusion mixing can be performed using density measurements, with the available diagnostic techniques.
   (c) Since the Water Channel setup is uniquely capable of studying the initial

    ‘two-dimensional’ flow as well as the ‘three-dimensional’ late stages, the onset of transition can be studied.

2. As for RTI is anisotropic with strong forcing functions (density gradient, gravity and initial vorticity), is the anisotropy persistent given an almost 2D initial perturbation profile?

    (a) The large-scale structures are highly anisotropic in nature, while the small-scale structures are isotropic. This is evident from the statistics calculated by the DNS of Cabot & Zhou (2013). Their results indicate high degree of anisotropy in the velocity PDFs and the correlation function. Using PIV, this anisotropy can be measured for the current experiments at low A_t.

    (b) Measurement of Reynolds stresses and a study of the turbulent kinetic energy spectrum at the end of the test section might reveal information on anisotropy.

    (c) However, the length of the test section might be a restriction on the maximum mixing Reynolds number attained in the current experiments.

3. From the recent 2D DNS results of Wei & Livescu (2012), the different stages of evolution of RTI are reorganized, along with the observation of the reacceleration and the chaotic stage. Are these stages observed in experiments? Since the perturbation Reynolds numbers, Re_p, of the simulations are of the order of the Water Channel experiments, is it possible to confirm these new stages from experiments?

    (a) A set of experiments may be designed to observe these new stages, however, the physical dimensions of the Water Channel as well as the maximum temperature attainable in this low Atwood number setup, might limit the maximum Reynolds number attainable in the Water Channel experiments.

    (b) From experimental data, the time-scales for each of the stages of RTI can be also extracted.

4. Apart from the above, clarity on the rate of deposition of energy by RTI into different scales of energy, which affects the flow evolution is desired. i.e. large-scale deposition and fine-scale energy deposition.

    (a) The large-scale energy deposition affects the mean flow behavior, which can be studied from the growth rate of flow structures, i.e. bubbles and spikes, and the total mixing width (integral quantities).

    (b) Fine-scale mixing, on the other hand, can be studied by means of gradient measurements such as scalar dissipation and molecular mixing parameters, which are sensitive to the density gradients (differential quantities). Therefore, different experimental techniques that can measure wide field as well as localized variables need to be implemented.

    (c) An analysis of the variation of the two-fluid interface will provide valuable knowledge of the nature of transport from the largest to the smallest scales of the flow.

2.4 Objective of dissertation

The current dissertation attempts to answer the above questions by means of experiments using the Water Channel facility, description of which is provided in §3. The present set of multi-mode experiments are designed to study the effects of ICs on the development of RTI in the Water Channel. The objective of these experiments is to vary the phase difference for a given pair of wavelengths and wavelength variation of the initial perturbation and quantify their effects. Therefore, the expected outcomes of this study are as follows: *i*) Perform a range of experiments with varying phase difference angle and varying wavelengths, such that the effect of magnitude of wavelength and the ratio of component wavelengths of binary and multi-mode initial conditions can be discerned. *ii*) Observe the structures and obtain a relationship between the shape of the structures and the input wavelengths in the early and late-time. Also, understand the physics behind mode coupling between different modes of a multi-mode experiment. *iii*) Measure the amount of total mixing, molecular mixing and fine-scale mixing at different stages of evolution. *iv*) Quantify the late-time density and velocity statistics for different ICs, in order to understand the flow behavior. The ultimate objective of this exercise is to find functional dependence of multi-modal instability physics on the component modes.

3. EXPERIMENTAL SETUP AND DIAGNOSTICS*

This section describes the Water Channel setup and diagnostic techniques used for flow measurement in detail. The setup is designed to support different types of experiments on Buoyancy (RTI) and shear-driven flows. Water Channels are widely used in fluid dynamics research facilities. They typically consist of a rectangular Channel with a developing section and a test (or visualization) section. A schematic of the system setup is shown in Fig. 3.1. Listed in the figure are the components of the system. Previously, the Shock Tube and Advanced Mixing Laboratory (STAML) facility at Texas A&M University Riverside campus was moved to the University Services Building (USB), therefore the setup was rebuilt with many improvements to address the uncertainties and challenges observed with the older facility. The newer facility improved the control of the experiments, as well as provided cleaner Channel walls, resulting in improved optical diagnostics. This two-liquid system employs hot and cold water as working fluids. Temperature difference, ΔT, between these fluid streams is typically within the range of 5-8 °C, which results in Atwood number lying in the range of 6-12$\times 10^{-4}$.

The Channel is made of 0.5 in Plexiglas. The developing section, which is upstream of flapper, is 132 cm, while width of the Channel (W) is 20.32 cm, and height (H) is 33 cm. The length of test section (L) is 122 cm. The splitter plate is positioned at $y \approx 0$ cm, which results in top and bottom section heights of 17.78 cm and 15.24 cm respectively. Two plastic tanks of about 550 gallons store the hot and cold water at controlled temperature. Flow from the tanks to the Channel is

---

*Part of this chapter is reprinted with permission from "Effect of initial conditions on Rayleigh-Taylor mixing" by Kuchibhatla, S. & Ranjan, D., 2013. Physica Scripta, T155, 014057, Copyright 2013 by IOP publishing.

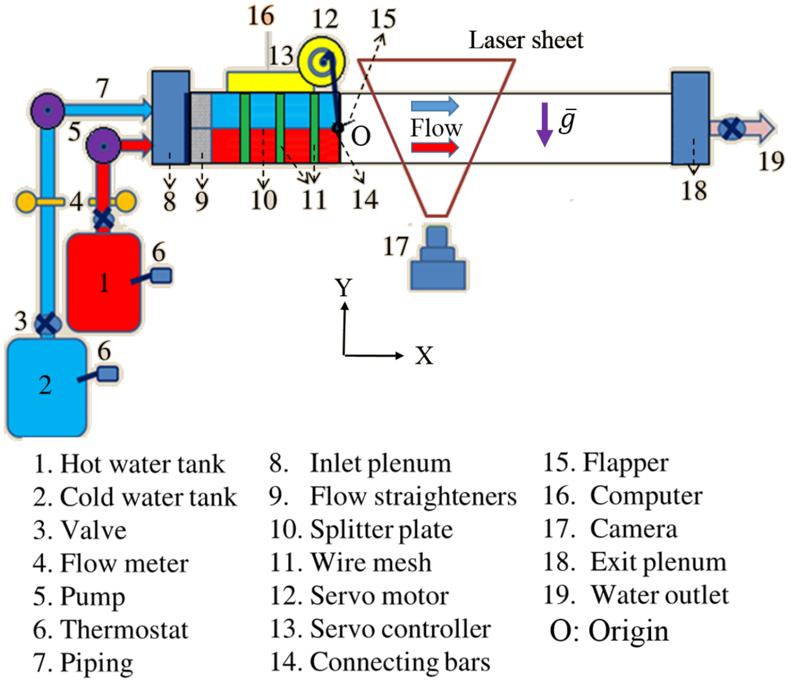

Figure 3.1: Schematic of the Water Channel setup. Figure taken from Kuchibhatla & Ranjan (2013b).

regulated by valves and is measured by using digital flow meters. Two pumps attached to each of these tanks pump water to the Channel at a steady rate. Plenum chambers located at the beginning and end of the Channel serve to smooth the flow of water in and out of the Channel. Flow straighteners placed in the early part of the Channel and wire meshes placed at regular intervals along the Channel are used to regulate the flow. This is intended to create a laminar exit flow off the splitter plate. Splitter plates of different thicknesses have been used in the past, and the latest set of experiments uses a splitter plate of 0.125 in thickness. Any bubbles that are trapped during filling water into the Channel escape through holes provided at the corners of the sections of the splitter plate, which are sealed off before turning on the water pumps. Hot water for the present set of experiments is supplied by using an in-line heater as shown in the schematic. This heater supplies heated water to the hot water tank at a constant temperature. However, the water in the tank is density stratified during filling, because of the gravity. Temperature of the water in both tanks at half the tank height is monitored using an E-type thermocouple with hand-held digital reader. As Chlorine content in the supply water varies on a daily basis, a 2.0 N solution of Sodium Thiosulfate ($Na_2S_2O_3$) is added to neutralize it. This is essential for the successful visualization of the experiment as the color of Nigrosene dye used as fluid marker changes to murky brown in the presence of any non-neutralized acid content in the water. It is to be noted that Nigrosene of 5.0 g is added to the cold water tank for every fill of the tank. This is intended to provide contrast for backlit imaging. The mass of dye is selected such that it lies within the range corresponding to a linear variation of dye absorption with fluid density. Details of calibration procedure can be found in Kuchibhatla (2010). A single axis integrated Ethernet controlled and amplifier, model CDS-3310$^{®}$ by Galil Tools Inc. is used to create the required initial perturbations. This servo unit, as will be called henceforth, consists of a power unit, which supplies the power to the amplifier unit that goes through 4000 counts for each rotation of the axis. The amplifier works on torque mode (torque can be specified as the output), and has a supply voltage of 18-72 V direct current and continuous amperage of 7 A. The motor is equipped with a feedback sensor that reads the actual voltage and position of the axis with time, which can be plotted along with the corresponding error. The software interface of Galil Tools Inc. is used to input commands for specifying motor function. The motor is capable of performing many complicated motions of the single axis, and it is validated for accurate output to input signal in Kuchibhatla (2010). Motion of the single axis is specified by specifying a contour profile that starts at the initial rest position of the flapper to the desired final position, at user specified speed, acceleration and deceleration. Smoothing functions can be applied to reduce high-frequency noise in the system. The user specifies optimized gains for the axis such that the specified contour is followed with the least possible Root Mean Square (RMS) error. Using the interactive scope of aforementioned software, the error bars with time can be checked instantaneously, and the system can be tuned accordingly. An initial perturbation is defined as small only when it satisfies the following approximation: $y = sin(kA) \approx kA$, when $kA \ll 1$.

Mean free stream velocities of the top and bottom sections of the Channel are chosen such that the all the regimes of the development of RTI can be observed at different locations in the test section. Higher free stream velocities quicken the growth rates and the height of the Channel may be inadequate for visualization in such instances. Density of water as a function of temperature, $\rho(T)$, is measured from samples using a Densitometer of high accuracy ($\approx$ 0.01% uncertainty) to replace the correlation by Kulkula (1981), which was used in previous Water Channel experiments. From this measured data, a polynomial best fit for $\rho(T)$ (in gcm^{-3}) is obtained, and A_t is defined by Eqn. 1.1 at temperatures (in °C) within the working range of 15-35 °C. The following polynomial correlation (Eqn. (3.1)) for density is fit to the data:

$$\rho = -8.61 \times 10^{-9}T^3 - 6.50 \times 10^{-6}T^2 - 1.85 \times 10^{-5}T + 1.0023 \tag{3.1}$$

Hot and cold water streams are pumped into the Channel resulting in a steady convective velocity (U_{mean}) of 4.6 cms^{-1} ($\approx$ 1.24% uncertainty). The mean convective speed is calculated from repeated digital flowmeter measurements and measured cross sectional area of top and bottom sections. The flapper mechanism is a novel servo-controlled mechanism (Doron & Duggleby, 2011) devised in order to impose precisely repeatable, controllable initial conditions at the joining of the two fluid streams. A stainless steel flapper, which is a knife edge 5.08 cm long and 0.32 cm thick, runs along the width of the Channel, and is coupled to the servo mechanism using connecting rods. Details of the Water Channel experiments using optical diagnostics, and mixing measurements using the ensemble averaging technique are presented in Kuchibhatla & Ranjan (2013a). In this dissertation, the servo system is used to precisely control the amplitude, A, phase angle, β, and frequency, ω, of the initial waves, up to a maximum of 11 modes. Details of the flapper validation are provided in Kuchibhatla & Ranjan (2013b). The knife edge flapper is coupled to the servo mechanism using connecting rods as shown in Fig. 3.2. A side view drawing showing the profile of the flapper is also shown in the figure.

The system is equipped with a Light Emitting Diode (LED) backlight, which produces a uniform monochromatic background. Images of the background are taken at different intensity levels and color modes and validated, in Kuchibhatla & Ranjan (2013b). Maximum uncertainty in backlight intensity is calculated to be $\approx$

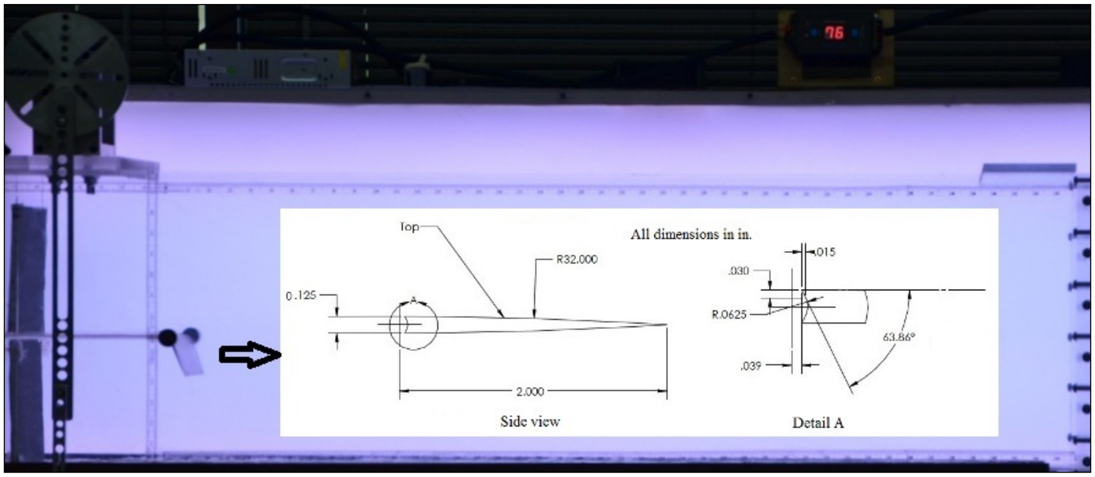

Figure 3.2: Image of Water Channel and detailed profile of flapper. Figure taken from Kuchibhatla & Ranjan (2013b).

8.15%. Nigrosene dye (concentration of 3.66 gm^{-3}) is used as marker for the top-fluid stream. A calibration procedure as previously specified in Banerjee & Andrews (2006) and Ramaprabhu & Andrews (2004) is employed to validate a linear density variation of water density with dye intensity, the plots of which are provided in Kuchibhatla & Ranjan (2013b). A thorough discussion on uncertainty analysis and parallax error for Water Channel experiments is given in Snider & Andrews (1995) and Doron & Duggleby (2011).

In the current dissertation, three types of techniques are employed for density measurement: *a*) Ensemble averaging of high resolution ($\approx$ 14 MPx) widefield, LOS images taken with low temporal resolution (1 Hz), *b*) Planar Laser Fluorescence images (PLIF) of different smaller regions of the central plane ($z = 0$) taken at higher temporal resolution (15 Hz) and relatively lower spatial resolution ($\approx$ 1.4 MPx), and *c*) Temperature measurement at different points in the domain, using thermocouples, with lower spatial resolution ($\approx$ 0.635 cm), but high temporal resolution (1 kHz). Lastly, velocity fields in planar sections of the flow are measured using Particle

Image Velocimetry (PIV). Using these techniques, density and velocity statistics are obtained at different flow regimes. A discussion of these results is given in §4.

3.1 Ensemble averaging

For backlit images, a calibration procedure similar to Ramaprabhu & Andrews (2004) and Mueschke et al. (2006) is used to validate a linear variation of water density with dye intensity. It uses a calibration wedge to measure pixel intensity vs. dye concentration, and Beer-Lambert's principle relating pixel intensity vs. solute concentration. About 400 images of the flow field are taken using a Nikon-D7000® digital SLR camera, one second apart. Contours corresponding to the 5% and 95% volume fraction of cold water are extracted from the averaged image, and mixing width is calculated from the difference. Details of this technique employed in the Gas Channel experiments could be found in Banerjee & Andrews (2006). Further description of the setup, validation of the flapper mechanism and uncertainty measurements of velocity, temperature, dye calibration and background corrections can be found in Kuchibhatla (2010).

3.2 Thermocouple measurements

In order to address the low temporal resolution of the imaging techniques, pointwise density is calculated from temperature measurements that are made using high temporal resolution thermocouples. A thermocouple profiler or rake consisting of 7 high-speed thermocouple probes is constructed. A NI DAQ® system that can measure up to 3.3×10^5 samples per second equipped with built-in cold junction compensation is utilized. The thermocouples are of T-type (Constantan-Copper junction) with tip diameter of 0.0012 cm. The small size of these thermocouples allows almost non-intrusive measurement of the flow temperature at high temporal resolution, thus, enabling the measurement of small time-scale effects, especially at high mixing Reynolds numbers. This technique is therefore used for quantifying the density spectra, discussed in §4.3.

Point-wise density is calculated using Eqn. 3.1. A description of the physical variables used in the current study is specified below. Spatial coordinates are non-dimensionalized with H, whereas time is non-dimensionalized by $\tau = \sqrt{H/A_t g}$. An equivalent definition of time in convective systems is obtained using Taylor's hypothesis, i.e. $t = x/U_{mean}$. Other parameters are defined as follows: $\rho^*(x,y,z,t) = (\rho(x,y,z,t)-\rho_h)/(\rho_c-\rho_h)$ is the non-dimensionalized instantaneous density, $T^*(x,y,z,t) = (T(x,y,z,t)-T_c)/(T_h-T_c)$ is the non-dimensional temperature, where T_h and T_c are the hot and cold water temperatures. $\Delta T = T_h - T_c$ is the maximum temperature gradient, whereas $\Delta\rho = \rho_c - \rho_h$ is the maximum density gradient. Variables related to the molecular mixing phenomenon are defined as follows. $< f_h >=< \rho^* >$ is the volume fraction of heavy fluid, $f_l = 1 - f_h$ is the volume fraction of light fluid, $B_0 = \lim\limits_{T\to\infty} \frac{1}{T}(\rho'^2 dt/\Delta\rho^2)$ (Linden et al. (1994) and Steinkamp et al. (1999)) is the density fluctuation self-correlation for similar fluids, $B_2 = f_h f_l$ is the density fluctuation self-correlation for two distinct fluids, and $\theta = 1 - B_0/B_2$ is the molecular mixing discussed in 1. Details of the step-wise calculation of above mixing parameters can be found in Wilson & Andrews (2002). Here, $<>$ indicates the time mean defined by $\frac{1}{T}\int\limits_0^T \phi dt$, where T is the total time of observation and ϕ is any scalar function of time. Correspondingly, $< \rho^* >$ and $< T^* >$ are the time-mean non-dimensional density and temperature respectively. We define $\rho'(x,y,z,t) = \rho(x,y,z,t)- < \rho(x,y,z) >$ as the instantaneous fluctuating density at any given location.

3.3 PLIF imaging

Planar Laser Fluorescence Image (PLIF) images of the center-plane of the Channel for single, binary and multi-mode cases at a single streamwise location of $x_{im,1}$ = 1 in are taken for different cases and presented in §4.5. In all experiments, the top water stream is dyed with Rhodamine, which fluoresces when exposed to 532 nm green slight. A TSI Powerview® camera with 1.4 MPx resolution is used to take flow images at a steady frequency of 15 Hz. For each experiment, a total of 2250 images are taken to reduce statistical uncertainties. A study of the variation of uncertainty in density measurement from PLIF images with the number of images is provided in Ramaprabhu (2003). From this study, it is deduced that a high number of images reduces the uncertainty drastically, therefore, 2250 images are taken for each case, which is much greater than for previous Water Channel studies.

It should be noted here that some of the advantages of the PLIF technique over the ensemble averaging include: *a*) Greater temporal resolution, which means that structural features that may not be captured in ensemble averaging can be captured with this technique, *b*) This ability improves the accuracy of mixing statistics, by capturing intermediate time-scale features, in contrast to ensemble averaging, which loses all fine-scale features, *c*) Planar nature of images (width of the laser plane $\approx$ 2 mm), which reduce greatly the smearing observed in LOS images, (viz. due to boundary layer effects, among others), and *d*) PLIF imaging enables the capturing of 3D effects in the flow field, e.g. by comparing the planar images at different spanwise locations.

3.4 PIV measurements

Particle Imaging Velocimetry (PIV) technique is used for measuring the two-dimensional velocity distribution in XY planes (i.e. plane formed by the streamwise and crosswise directions). Use of PIV for measuring velocity in incompressible flows such as in water RTI is a common practice and is reliable. Silver coated hollow glass spheres (SGHS) of 10 μm size and neutral buoyancy are inserted into the tanks and mixed thoroughly using sump pumps. About 1.2-1.5 g of particles are used for each tank. The exact amount of particles are added to both tanks measured using table scales with a least count of ± 0.01 g. For simultaneous measurement of density and velocity fields, $\sim$ 0.12-0.22 g of Rhodamine 6G is added to the cold water tank during each experiment.

Planar measurement of these regions is taken using two Nd-YAG lasers that pulse alternatively at 15 Hz each and a time delay of 0.033 s, resulting in an effective imaging frequency of 30 Hz.Images of the flow fields are ensemble averaged to get the average velocity field in the XY plane. For PIV, a bandpass filter of 532 nm ± 7 nm is used for PIV imaging to capture the scattered light only. For PLIF measurements, very small concentrations (0.1 mgl^{-1}) of Rhodamine 6G are used with a high camera aperture to take flow images at 15 Hz. Such low concentrations are required for using fluorescence intensities as a measure of density. This is due to the nonlinearity in light attenuation at higher concentrations, as well as for less interference or cross talk between the PIV and PLIF images. A notch filter that rejects incident laser illumination of 533 nm ± 2 nm is used during PLIF imaging, so that only the fluoresced illumination is captured in images. A CCD camera with 1.4 MPx resolution is used to take PLIF images, while the PIV camera had a resolution of 1 MPx. For all cases, background images, dye and spatial calibration images are taken and used for subtracting image noise from images and for ensuring both PLIF and PIV cameras record the same region in space.

For the 520 PLIF images, white noise caused $\approx 0.4\%$ uncertainty. Background images are taken for all cases and subtracted in order to remove artifices of the imaging system such as non-uniformities in the laser plane due to optical alignment issues. As the Schmidt number of Rhodamine dye in water, Sc of the dye is ≈ 1500, a thorough mixing of the dye with water is achieved to avoid lumps of dye that would trail the water surrounding them. About 520 PLIF images and 1040 PIV images could be recorded, limiting the total time of observation to ≈ 34 s.

4. RESULTS AND DISCUSSION*

The effect of initial conditions on Rayleigh-Taylor instability (RTI) is investigated using a set of experiments (called ‘cases’ in this study).

4.1 Quantification of initial condition

4.1.1 Mixing due to ICs in the absence of RTI

In the current dissertation, different diagnostic techniques are employed to quantify the IC, such that an accurate estimate of the flapper motion can be derived. Therefore, experiments are performed for the following scenarios: *a*) Wake flow due to the splitter plate, where the top and bottom water streams have the same temperature, and the flapper is motionless. *b*) Single-mode IC without density gradient, where the top and bottom water streams at the same temperature are subject to mixing in the presence of single-mode ICs. Here, the cumulative effect of the interaction of IC with the wake can be observed. Table 4.1 lists the parameters for this set of experiments. Here, $A_t = 0$ for all cases.

Table 4.1: Experimental parameters for IC study without RTI.

Case #	λ (cm)
1A0	0
2A0	2
3A0	4
4A0	8

Sample images of the flow field for each case are shown in Fig. 4.1, depicting

---

*Part of this chapter is reprinted with permission from “Effect of initial conditions on Rayleigh-Taylor mixing” by Kuchibhatla, S. & Ranjan, D., 2013. Physica Scripta, T155, 014057, Copyright 2013 by IOP publishing.

an area of $\sim$ 11×9 cm^2. For case 1A0, structures arising off the wake of the splitter plate can be visualized, while for cases 2A0-4A0, orderly structures due to the input IC can be seen. While the flow structures corresponding to cases $\lambda = 2$ cm and $\lambda = 8$ cm are increasing with downstream distance due to the nonlinear mode coupling with inherent Water Channel modes, the structures corresponding to $\lambda = 4$ cm seem to be growing very little with streamwise distance. Perhaps this can be due to the similarity of the wavelengths, i.e. mode-coupling is minimal due to the inherent wavelength of the Water Channel, $\lambda_m \approx 4$ cm. From 2D DNS simulations of Mueschke (2008), it is calculated that $\lambda_m \approx 3.78$ cm.

Contour plots of ρ^* for these cases in Fig. 4.2 visualize the increasing mixing layer thickness with initial wavelength. Plots of molecular mixing parameters along the centerline of the mixing layer in the streamwise direction are shown in Fig. 4.3. Finally, to compare the effect of increasing wavelength, λ, centerline plots of B_0, B_2, θ and χ^* are presented in Fig. 4.4.

Significant observations include: *a)* From the Fig. 4.4(a), it can be seen that B_0, which is a measure of the standard deviation of density fluctuations, increases with wavelength, λ. The larger the wavelengths correspond to greater fluctuations are observed across the mixing layer. *b)* B_2, on the other hand, does not follow a clear trend. However, it can be clearly seen from the plot 4.4(b) that case 1A0 has very slow mixing layer development, because of the absence of flapper motion. Only the wake of the Water Channel is responsible for mixing, and therefore, less mixing is observed. From the Fig. 4.4(c), we see that the variation of θ is strongly in accordance to the variation of B_0, and weakly with respect to B_2. This observation is

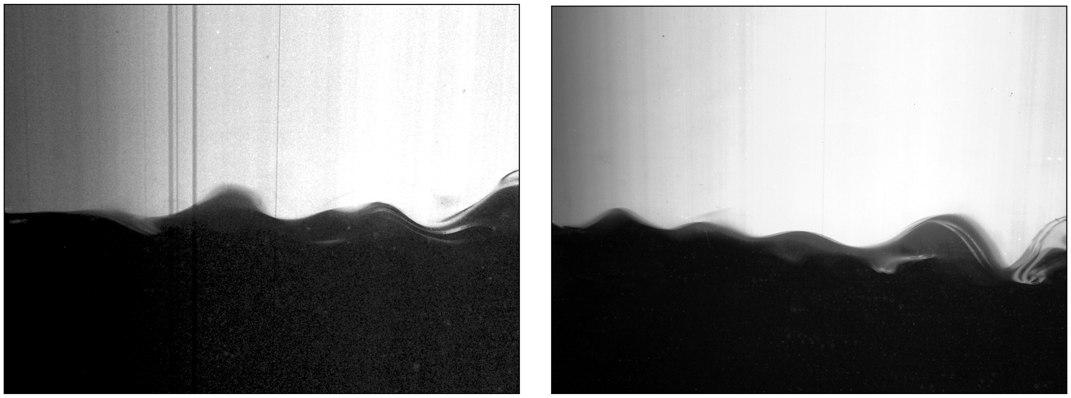

(a) Case 1A0 (b) Case 2A0

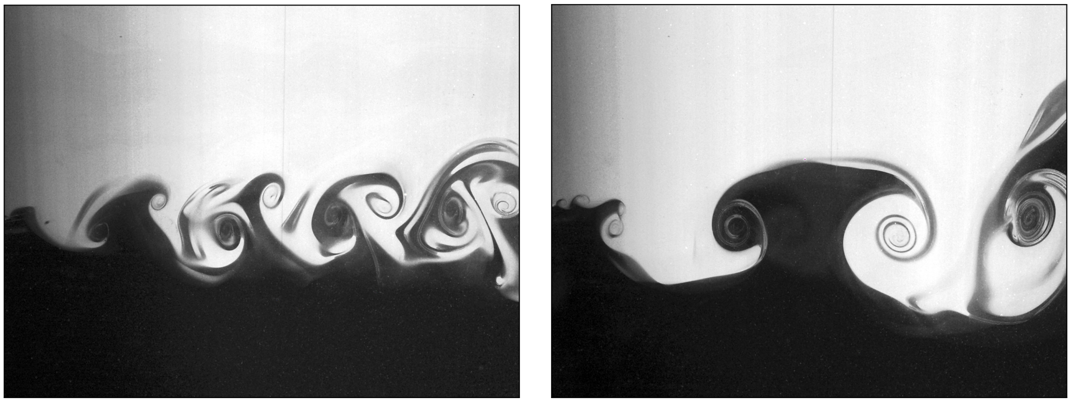

(c) Case 3A0 (d) Case 4A0

Figure 4.1: Instantaneous flow images for all cases without RTI.

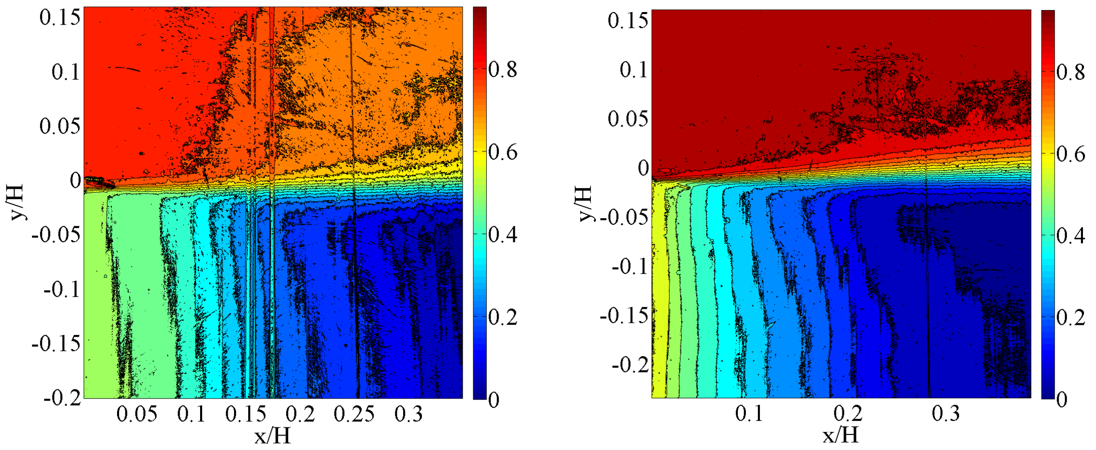

(a) Case 1A0 (b) Case 2A0

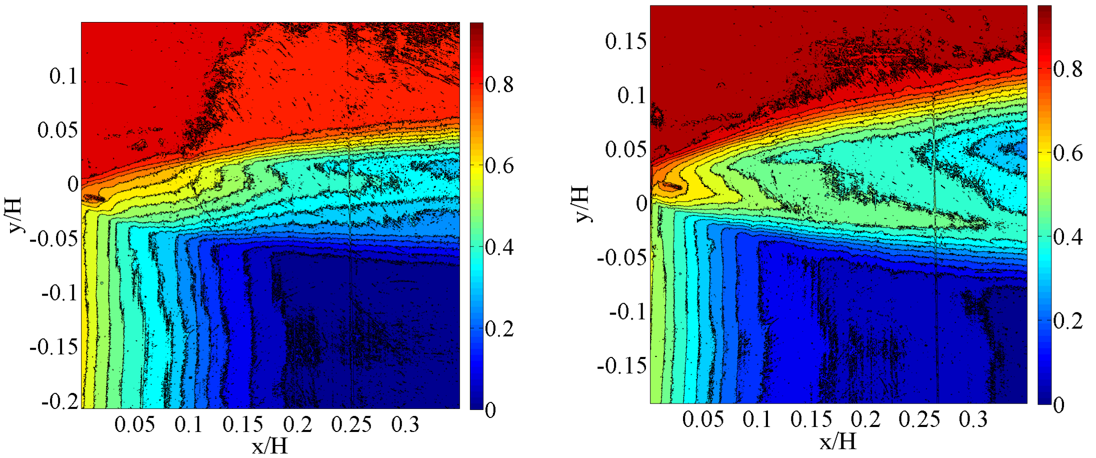

(c) Case 3A0 (d) Case 4A0

Figure 4.2: Contour plots of ρ^* for all cases without RTI.

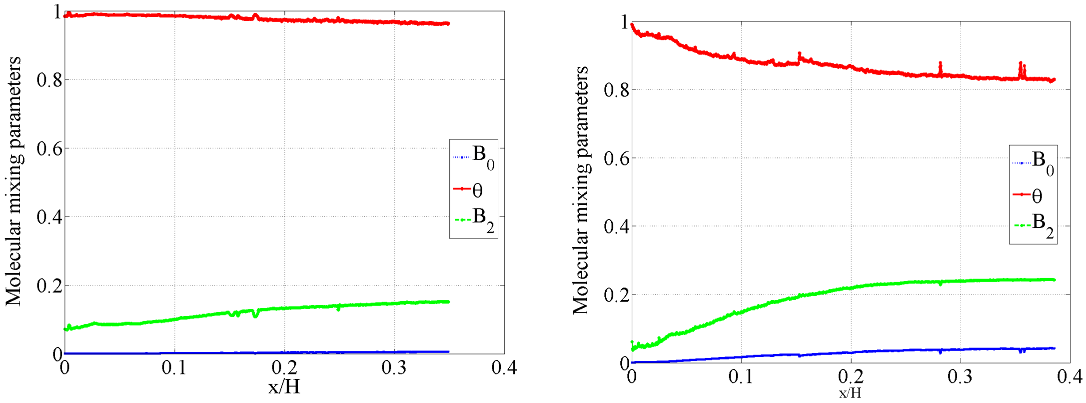

(a) Case 1A0 (b) Case 2A0

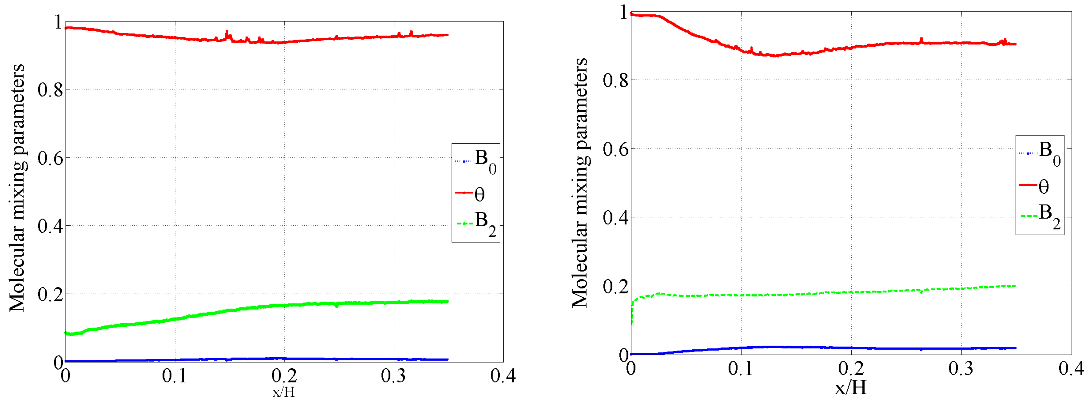

(c) Case 3A0 (d) Case 4A0

Figure 4.3: Centerline plots of mixing parameters for single-mode cases without RTI.

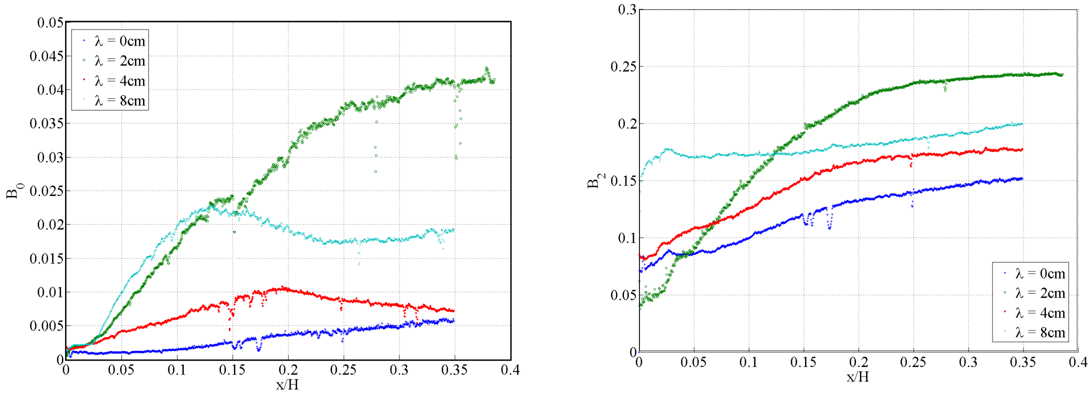

(a) B_0 (b) B_2

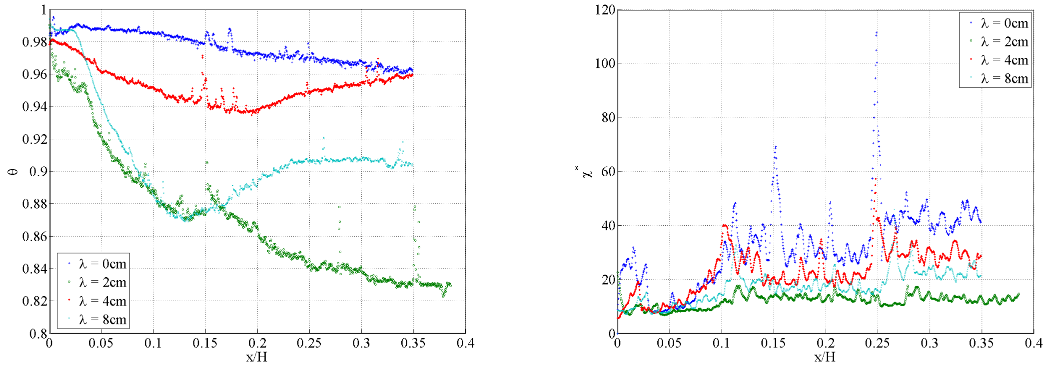

(c) θ (d) χ^*

Figure 4.4: Comparison of mixing parameters for no-flap case without RTI.

consistent with measurements of molecular mixing for other experiments, that follow in this dissertation. $\theta = 1$ at the edge of the splitter plate, and tapers down very slowly. From the plot of θ, it is proposed that B_2 reaches a constant value much faster than B_0, therefore, there exists a lowest value for θ. As the wavelength is increased, the lowest value is reached must faster. A similar trend is observed in the data of Ramaprabhu et al. (2005). *c)* Plots of the scalar mixing rate, χ^*, indicate that the fine-scale mixing occurs slowly in the presence of large wavelengths. As such, this could be attributed to the occurrence of fine-scale mixing at the point where the flapper changes its direction, i.e. where the flapper introduces a change in the direction of vorticity. *d)* Lastly, the case corresponding to $\lambda = 2$ cm behaves in a peculiar way. Because of the very small perturbation wavelength, the IC acts to enhance mixing of small scales as well as the moderate scales. Therefore, while mixing rate increases in the centerline, mixing parameter B_0 increases very rapidly, resulting in lower values of θ. Thus, small wavelengths cannot significantly increase the molecular mixing, while they are efficient in increasing fine-scale mixing. *e)* From the plots of non-dimensional density, ρ^* in Fig. 4.2, for all cases, we see that the imaging technique introduces an uneven lighting for the bottom section of the image. Due to this, the mixing width for the bottom section (hot water) can be erroneous. Therefore, it is suggested that by taking the upper half of the image, an analysis of the growth rate can be performed, because of the symmetric nature of mixing layer growth at such low Atwood numbers.

4.1.2 Effect of wake of the splitter plate

Plots of mixing parameters, B_0, B_2, θ and χ^* for the cases of Water Channel without and with RTI are given in Figures 4.5(a), 4.5(b), 4.5(c) and 4.5(d), respectively. From the plots, it can be deduced that the impact of RTI in the initial stages is insignificant, hence, the initial stages are strongly dictated by the IC input into the system. The boundary layers above and below the splitter plate combine to form the wake region, which has a velocity deficit, as can be seen from the flow PIV data presented later in this dissertation. However, the magnitude of this deficit is smaller than the velocity induced by the ICs into the flow field. Therefore, it is surmised that the ICs employed in this study are very large compared to the size of the splitter plate, and hence, for all further purposes, it is assumed that the effect of the wake is insignificant in the evolution of the instability.

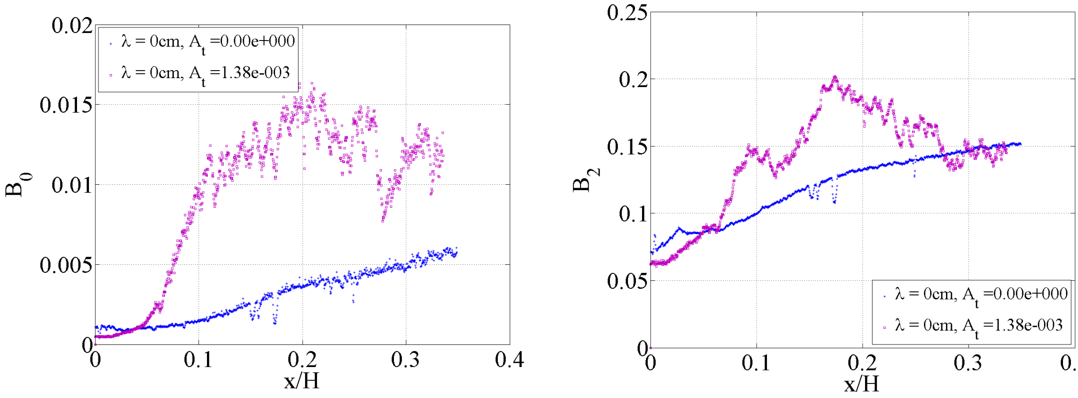

(a) Centerline variation of B_0 (b) Centerline variation of B_2

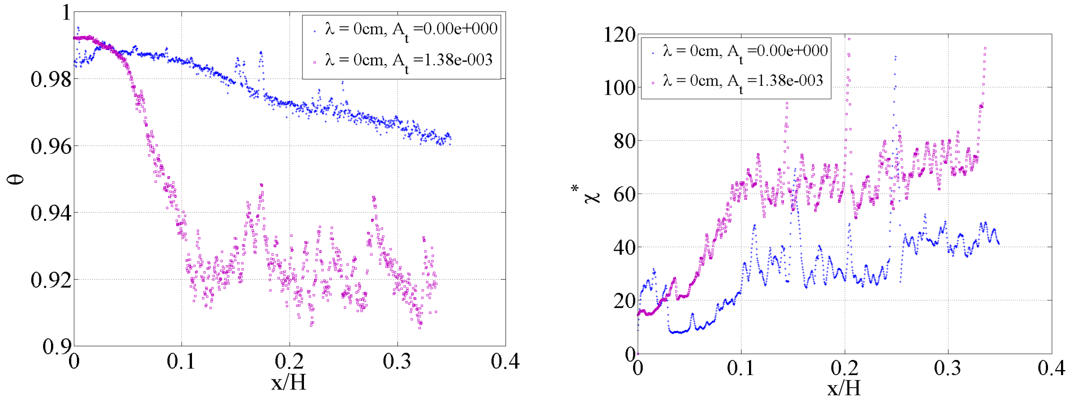

(c) Centerline variation of θ (d) Centerline variation of χ^*

Figure 4.5: Comparison of mixing parameters with and without RTI. The flapper remains motionless for both cases.

4.1.3 Linear growth rate study

The discussion in the above section details the mixing due to large initial perturbations, which are of comparable to the size of the maximum possible wavelength of the system. The initial amplitude for all ICs is significantly smaller than the wavelength of the IC, i.e. $A_i/\lambda_i = 0.1$, so that it corresponds to the linear regime. Therefore, a study of the linear regime, where growth of the mixing width is exponential, is proposed.

The following methodology is used: *i)* As seen from the time averaged PLIF images, the illumination of the pictures is much more uniform in the upper half of the pictures than the lower half. Therefore, only the top half of the mixing layer is used to calculate the half mixing width, assuming high degree of symmetry of the mixing layer. This is a fair assumption given the low Atwood numbers and single-modes employed in this LST. For binary and multi-mode ICs, the leaning of the structures makes the structures asymmetric. *ii)* The half mixing width is used to calculate the exponential growth rate constant, γ_{fit}, using a polynomial fit to non-dimensional time, t/τ, within the range of 0.05-1.0. *iii)* This curve fit growth rate, γ_{fit}, is then compared to the analytical γ from LST and reported in Table 4.2. The following set of equations is used (Equations 4.1 and 4.2):

$$ln(\frac{h}{h_0}) = e^{\gamma_{fit} t} \tag{4.1}$$

$$\gamma_{nd} = \gamma_{fit} \tau \tag{4.2}$$

Table 4.2: Linear growth rates of PLIF single-mode data.

Case #	λ (cm)	A_t ($\times 10^{-3}$)	γ_{fit} (s^{-1})	γ_{nd}
1	0	0.386	0.646	5.916
2	2	0.648	0.219	1.549
3	4	0.866	1.586	9.696
4	6	1.368	0.664	3.228
5	8	1.341	1.171	5.754

4.1.4 Three dimensionality of ICs

Some of the greatest challenges in using convective setups for Rayleigh-Taylor experiments are the following: *a)* Initial velocity gradient between streams: In spite of controlled water flow rates, the nature of experimental convective streams results in a small velocity gradient in the streams. This results in a degree of shearing in the flow, that will affect mixing. However, for low flow velocities such as in the current study, the shear effect will be small. *b)* Wake flow: The wake of the splitter plate interacts with the Rayleigh-Taylor mixing layer, affecting overall mixing. This is an artifact of the experimental setup, which is not witnessed in the conventional box type of Rayleigh-Taylor setups. *c)* Jet flow: The presence of wire screens and meshes upstream of the flapper results in jet-like flow structures, that have wavenumbers depending on the screen mesh spacing. These jets also develop with time, and interact with the Rayleigh-Taylor mixing. *d)* Boundary layer: The thermal and velocity boundary layers adjacent to the Water Channel walls tend to affect the flow diagnostics that employ LOS techniques. Using planar imaging techniques might reduce uncertainties due to the front and back wall boundary layers. However, the boundary layers at the top and bottom walls of the Channel do not greatly affect the core of the Rayleigh-Taylor mixing layer, which might be away from the walls. This is especially true for near incompressible setups, such as the current one.. To check the 3D effects, density profiles are measured at 9 locations in the spanwise direction (z), at 7 crosswise (y) locations and 2 streamwise (x) directions using high-speed T type thermocouples (sampled at 1 kHz). Location 1 corresponds to $x_1 = 1$ in right off the splitter plate, while $x_2 = 10$ in lies downstream of it. A polynomial correlation for the density of water as a function of temperature, T, is given in Eqn. 4.3 is used. This correlation is generated from measurements of water density in gcm^{-3} using a high accuracy Densitometer.

$$\rho = -8.61 \times 10^{-9} T^3 - 6.50 \times 10^{-6} T^2 - 1.85 \times 10^{-5} T + 1.0023 \tag{4.3}$$

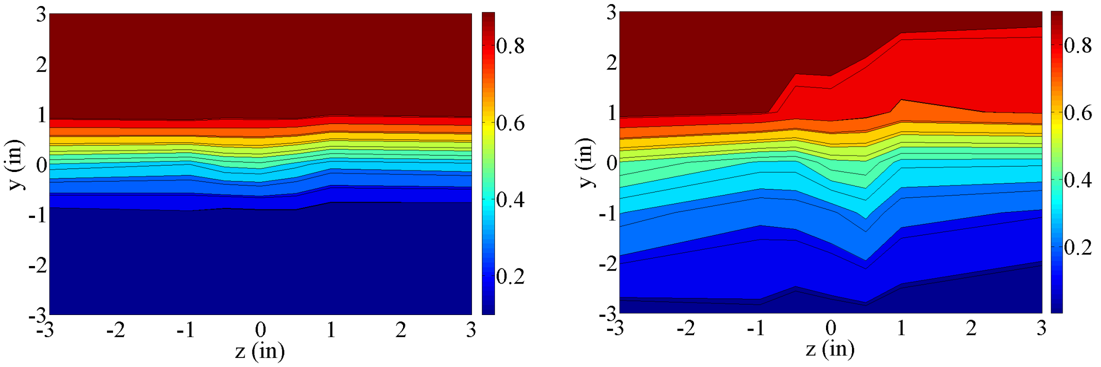

(a) $x_2/H = 0.769$

(b) $x_1/H = 0.0769$

Figure 4.6: Contour plot of $f_h = \rho^*$ for case 3.

For sample case 3, contour plots of the non-dimensional density, ρ^* shown in Fig. 4.6 show an almost uniform variation of the density profile with z. However, there seems to be an offset in the positioning of the thermocouples at location x_2, where the density profiles are skewed with y. Apart from this, the region corresponding to $z/H = 0$ in both plots shows a certain degree of variation in the density profile, which may be due to the presence of spanwise Rayleigh-Taylor modes due to the constraining walls of the Water Channel. Beta probability distributions of non-dimensional density are also provided, in Fig. 4.7 for the same case. they indicate a slightly skewed distribution right off the splitter plate with the y direction, which indicates an offset in the position of thermocouples along the y axis. This resulted in the central point being shifted to a region of about $y \approx 0.005$ in. However, the distributions indicate that the mixing layer tends to get more symmetric with downstream distance.

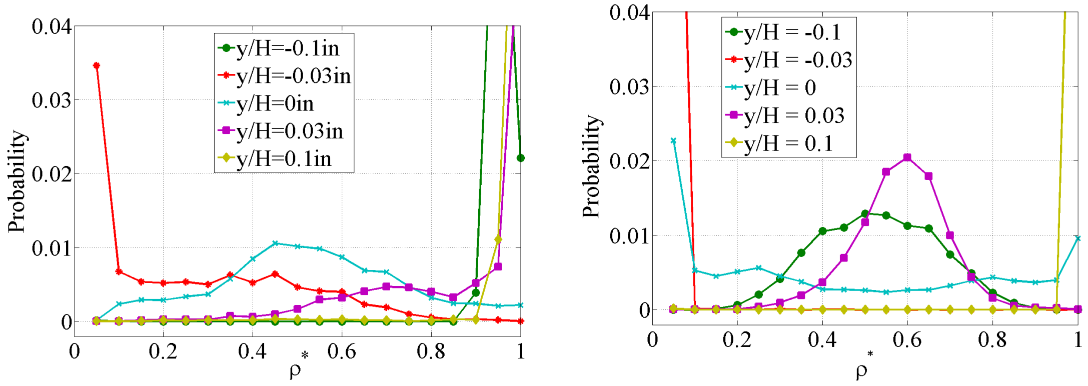

(a) $x_1/H = 0.0769$

(b) $x_2/H = 0.769$

Figure 4.7: Probability of $f_h = \rho^*$ vs. y for case 3. Figure taken from Kuchibhatla & Ranjan (2013b).

4.2 LOS imaging results

Some of the discussion and figures in this subsection are reproduced from Kuchibhatla & Ranjan (2013b) by permission from Institute Of Physics (IOP). This section details the measurement of mixing width obtained from images of the entire test section using the Single Lens Reflex (SLR) camera, using LOS imaging, while §4.5 details similar measurements using PLIF technique. Ensemble averaging is performed for only the first eleven cases, while images of flow structures are taken for all twelve cases. Experimental parameters for each case are listed in Table 4.3. It should be noted that the Atwood number is different for each case. An initial condition of the type specified in Eqn. 4.4 is imposed (with $A_i/\lambda_i = 0.1$) by the flapper for all cases. β_{i-1} is the phase angle of the ith mode with respect to the first mode. In this set of experiments, four sets of cases are defined: *i*) Cases corresponding to single-mode wavelengths ($\lambda = 0$ cm, 2 cm, 4 cm and 8 cm), *ii*) Binary-modes vs. component single-modes, *iii)* Binary-mode with varying phase difference angle ($\beta = 0°$, $45°$, $90°$ and $180°$) and *iv)* Multi-mode case (case 10) vs. its component binary-mode and single-mode cases. Also, the equivalent wavelength (λ_{eq}) for each IC is the largest wavelength among the individual modes.

Table 4.3: LOS experimental parameters. Table taken from Kuchibhatla & Ranjan (2013a).

Case #	λ_1 (cm)	λ_2 (cm)	λ_3 (cm)	λ_{eq} (cm)	β_1 (°)	β_2 (°)	A_t ($\times 10^{-3}$)	
							Flow visualization	Ensemble averaging
1	0	-	-	0	-	-	1.28	1.54
2	2	-	-	2	-	-	1.60	1.61
3	4	-	-	4	-	-	1.65	1.83
4	4	2	-	4	45	-	1.62	1.84
5	4	4	-	4	45	-	1.50	1.50
6	8	-	-	8	-	-	1.81	1.81
7	8	2	-	8	0	-	1.54	1.54
8	8	2	-	8	45	-	1.63	1.63
9	8	2	-	8	90	-	1.72	1.72
10	8	4	2	8	45	90	2.08	1.54
11	8	4	-	8	45	-	1.81	1.85
12	8	2	-	8	180	-	1.81	-

$$y_i = \sum A_i \sin(\omega_i t + \beta_{i-1}) \tag{4.4}$$

A montage of flow structures and square of density gradients given below provides some interesting insights. For each of the cases, an area of about 74 cm×25 cm is photographed and shown in Figures 4.8(a), 4.8(c), 4.8(e), 4.8(g), 4.9(a), 4.9(c), 4.9(e) and 4.10(a), while instantaneous square of density gradients is shown in Figures 4.8(b), 4.8(d), 4.8(f), 4.8(h), 4.9(b), 4.9(d), 4.9(f) and 4.10(b). The images are organized in the order of single-mode cases followed by binary-mode cases, and the multi-mode case. Adjacent to each flow image, the corresponding contours of square of density gradients are provided. For the single-mode cases of λ = 0-8 cm (Figures 4.8(a), 4.8(c), 4.8(e) and 4.8(g)), the amplitude of the IC is increasing, and larger bubbles and spikes are observed as the flow evolves with time.

For a binary-mode IC, a smaller wave is imposed on the larger wave, characterized by a smaller mushroom emanating from the larger mushroom. As the instability develops, smaller secondary structures arise from the primary and secondary mushrooms, due to KHI mechanism after initial stages. Leaning of the small spike and bubble with varying αs can be observed (Figures 4.9(a), 4.9(c) and 4.9(e)). For binary-mode cases 8-9, varying the phase angle β from 45° to 180° results in the leaning of the smaller spikes with respect to the larger spikes' orientation (by the leaning angle, δ). This leaning of the smaller spikes can be treated as an equivalent amount of shear being applied in the horizontal direction. Analysis of the variation in δ with very small increments in β, for different wavelength ratios λ_1/λ_2 is required for a complete understanding of this phenomenon.

Image of the multi-mode initial condition instability (Fig. 4.10(a)) shows the bubbles and spikes for 3 initial modes. The intermediate wavelength of 4 cm interacts with the largest wavelength in such a way that the largest spike appears to lean to the right. The smallest wavelength of 2 cm interacts in a similar manner with respect to the intermediate wavelength.

As mentioned in §1, a study of the dissipation of scalars, such as temperature or concentration, is required because they affect mixing by reducing buoyancy. Whereas the traditional approach (for obtaining scalar dissipation contours) is based on instantaneous wide-field images of thin planar slices of the flow domain, instantaneous images of the LOS images are used in this current dissertation. The LOS images contain the aggregate information of all planes perpendicular to the optical axis. The LOS images of the Water Channel mixing experiments when compared with planar images (such as obtained by Planar Laser Induced Fluorescence (PLIF)) are similar to each other in the early-time, where the flow is largely two-dimensional in nature, but are significantly different from each other at late-times, due to the three-dimensional nature of turbulent flow structures. Therefore, the square of density gradients from LOS images at late-time is greater than traditional scalar dissipation, because of the greater density gradients in LOS images compared to planar images. Plots of square of density gradients or mixing rate (χ) obtained from these instantaneous images of concentration are given in Figures 4.8(b), 4.8(d), 4.8(f), 4.8(h), 4.9(b), 4.9(d), 4.9(f) and 4.10(b). Scalar dissipation rate is defined by $\chi(x, y, t) = D(\nabla c.\nabla c)$, where D is the molecular diffusivity of two miscible fluids (such as in the current scenario) and $c(x, y, t)$ is the instantaneous concentration from images. The instantaneous concentration maps are normalized based on the maximum and minimum concentration, and are equivalent to instantaneous volume fraction maps. A similar approach is adopted by Tomkins et al. (2008) for shock-bubble interactions wherein they tried to estimate the amount of mixing due to concentration gradients as a function of time. Scalar dissipation rates are used for quantifying the fine-mixing in shear flows, e.g. by Buch & Dahm (1996). They are used to identify the amount of molecular mixing and the effect of Schmidt number ($Sc = \nu/D$, where ν is the kinematic viscosity) on fine-scale mixing. Accordingly, square of density gradients can be treated as an equivalent form of scalar energy per unit mass, therefore providing a measure of fine-scale mixing. As both heavy and light fluids are water, the mass coefficient of diffusivity for this pair will be the kinematic viscosity, ν_{mean}, hence the Schmidt number, $Sc \sim 1$. The kinematic viscosity for each case is calculated by $\nu_{mean} = 2\mu_{mean}/(\rho_c + \rho_h)$ to account for the mean dynamic viscosity and mean density of the flow. Mean dynamic viscosity, μ_{mean}, at the mean temperature $(T_c + T_h)/2$ is interpolated from Kestin et al. (1978) within the temperature (T in °C) range of 0-40 °C, and given in Eqn. 4.5:

$$\begin{aligned} log_{10}(\frac{\mu(T)}{\mu(20\ ^{\circ}C)}) =& [1.2364 \times (20 - T) - 1.37 \times 10^{-3}(20 - T)^2 \\ & + 5.7 \times 10^{-6}(20 - T)^3]/(T + 96) \end{aligned} \tag{4.5}$$

From the contours of square of density gradients provided, it should be noted that the concentration gradients induced by the mixing layer are much larger in comparison to any concentration gradient due to shear in the convective streams because of the uniformly dark backgrounds in most images. However, plot 4.10(b) shows some comparable background gradients. All provided contour plots of instantaneous square of density gradients are qualitative and show some interesting trends. Smaller wavelength cases (cases 1-2 in Figures 4.8(b) and 4.8(d)) exhibit strong gradients in the mixing layer, whereas larger wavelengths exhibit weaker gradients spread out over larger areas of the mixing layers (cases 5 and 4 in Figures 4.8(f) and 4.8(h)). For the binary-mode cases with phase difference (cases 8, 9 and 12 in Figures 4.9(b), 4.9(d) and 4.9(f)), asymmetric mixing rates (with respect to the horizontal) are visible. Also, the instantaneous mixing rate depends upon the phase angle, β, as supported by the images. For the multi-mode case (case 10 in Fig. 4.10(b)), concentration gradients are much smaller but spread over a wider area. From all the contours, the mixing rate tends to become uniform towards later times, i.e. after $t^* = 3.5$. As the square of density gradients is effective in quantifying fine-scale mixing that is observed in RTI only at the later times, a discussion of the mean mixing rates and their asymptotic behavior is provided later in this section.

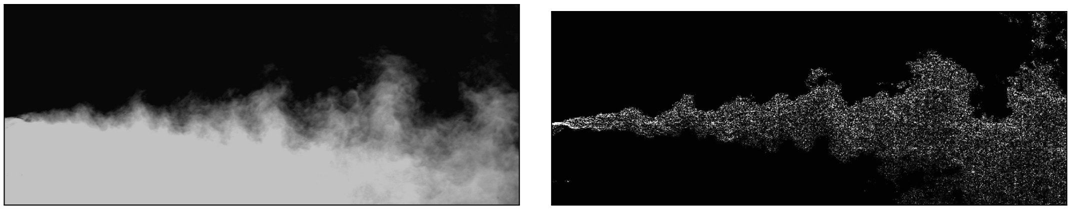

(a) ρ^* for no flap case (b) χ^* for no flap case

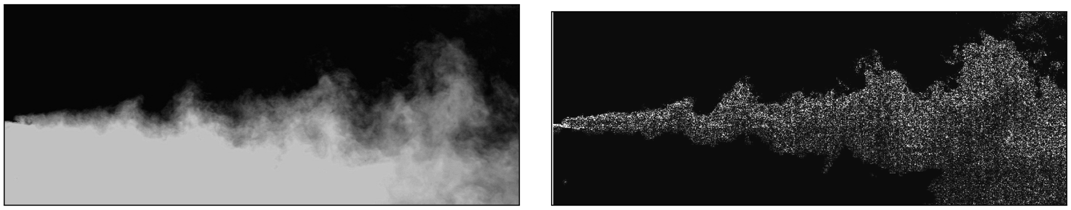

(c) ρ^* for case 2: $\lambda = 2$ cm (d) χ^* for case 2: $\lambda = 2$ cm

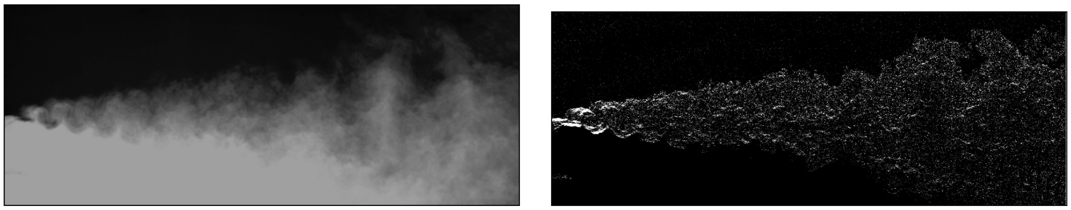

(e) ρ^* for case 3: $\lambda = 4$ cm (f) χ^* for case 3: $\lambda = 4$ cm

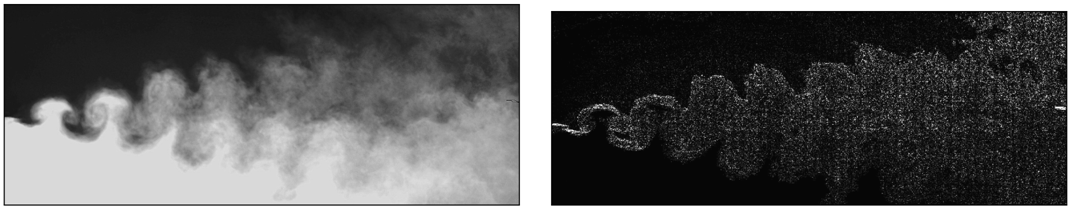

(g) ρ^* for case 6: $\lambda = 8$ cm (h) χ^* for case 6: $\lambda = 8$ cm

Figure 4.8: Contour plots of single-mode cases. Non-dimensional density is given in the left column, while square of gradient is provided in the right column. Figure taken from Kuchibhatla & Ranjan (2013a).

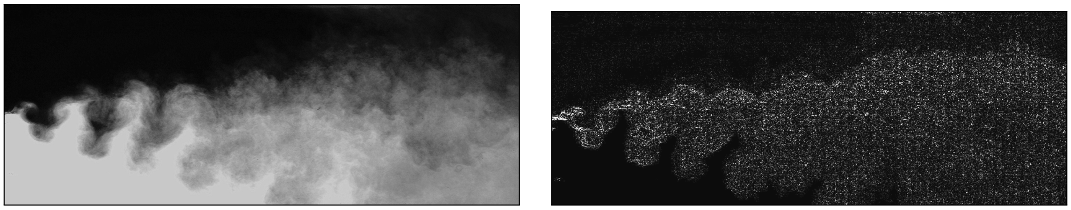

(a) ρ^* for case 8: $(\lambda_1, \lambda_2, \beta)$ = (8 cm, 2 cm, 45°)

(b) χ^* for case 8: $(\lambda_1, \lambda_2, \beta)$ = (8 cm, 2 cm, 45°)

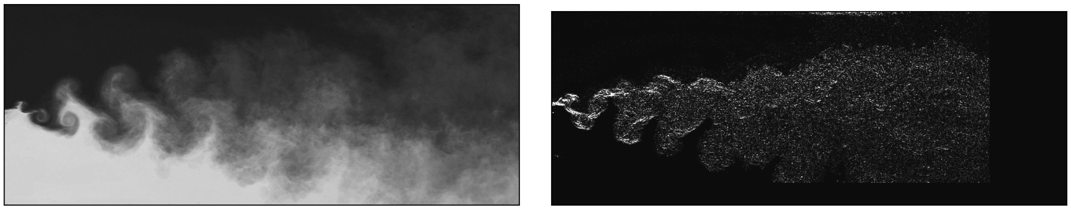

(c) ρ^* for case 9: $(\lambda_1, \lambda_2, \beta)$ = (8 cm, 2 cm, 90°)

(d) χ^* for case 9: $(\lambda_1, \lambda_2, \beta)$ = (8 cm, 2 cm, 90°)

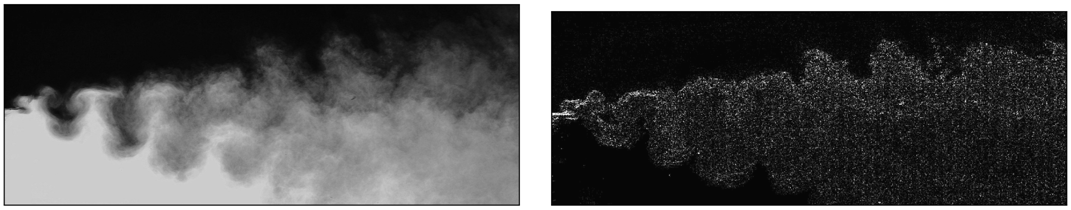

(e) ρ^* for case 12: $(\lambda_1, \lambda_2, \beta)$ = (8 cm, 2 cm, 180°)

(f) χ^* for case 12: $(\lambda_1, \lambda_2, \beta)$ = (8 cm, 2 cm, 180°)

Figure 4.9: Contour plots of binary-mode cases. Non-dimensional density is given in the left column, while square of gradient is provided in the right column. Figure taken from Kuchibhatla & Ranjan (2013a).

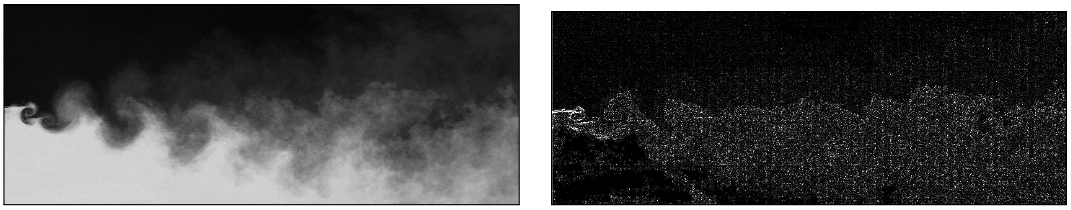

(a) ρ^* for case 10: $(\lambda_1, \lambda_2, \lambda_3, \beta_1, \beta_2)$ = (8 cm, 4 cm, 2 cm, 45°, 90°)

(b) χ^* for case 10: $(\lambda_1, \lambda_2, \lambda_3, \beta_1, \beta_2)$ = (8 cm, 4 cm, 2 cm, 45°, 90°)

Figure 4.10: Contour plots of multi-mode case. Non-dimensional density is given in the left column, while square of gradient is provided in the right column. Figure taken from Kuchibhatla & Ranjan (2013a).

Using the ensemble averaging technique, contour lines corresponding to mean volume fraction of heavy fluid, $< f_h > = 0.05$ and 0.95 are extracted from the average image, and mixing width defined as the crosswise distance between these two contours, is plotted in Figures 4.11(a)-4.11(d) for different sets of cases. At low A_t such as used in this current work, the mixing layer can be considered symmetric about the splitter plate centerline. Therefore, bubble and spike mixing width are equal to half the total mixing width.

For single-mode cases in Fig. 4.11, one can observe that the mixing width increases with increasing wavelength from 0 cm to 8 cm. For binary -mode case 8 in Fig. 4.11(b), mixing width is greater for all times compared to the component single-mode cases of 8 cm and 2 cm. Similarly, from Fig. 4.11(d), increasing the number of modes from binary to multi-mode shows higher mixing width as compared to the component cases of 11 and 2, i.e. binary-mode of 8 cm and 4 cm wavelengths, and a single-mode of 2 cm wavelength. Therefore, it can be inferred that increasing the number of modes of the initial condition increases ensemble averaged mixing width. For the selected wavelength ratio of 4:1, changing β from 0° to 45° to 90° appears to have insignificant effect on mixing width, as shown in Fig. 4.11(c). Although leaning of the primary and secondary spikes and bubbles is observed in these cases 7-9, the time averaged mixing width is observed to be very similar.

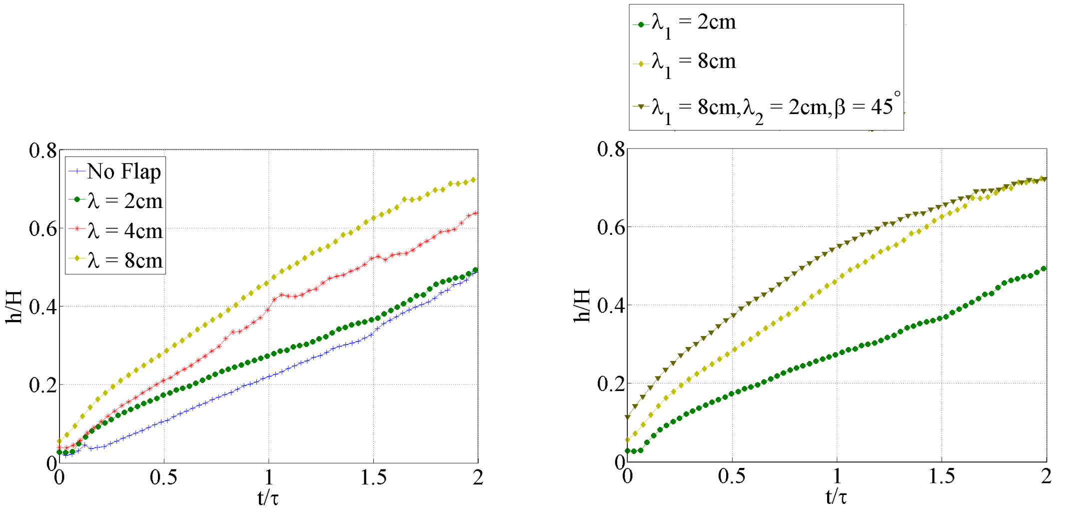

(a) Single-mode cases

(b) Binary-mode *vs.* component single-mode cases

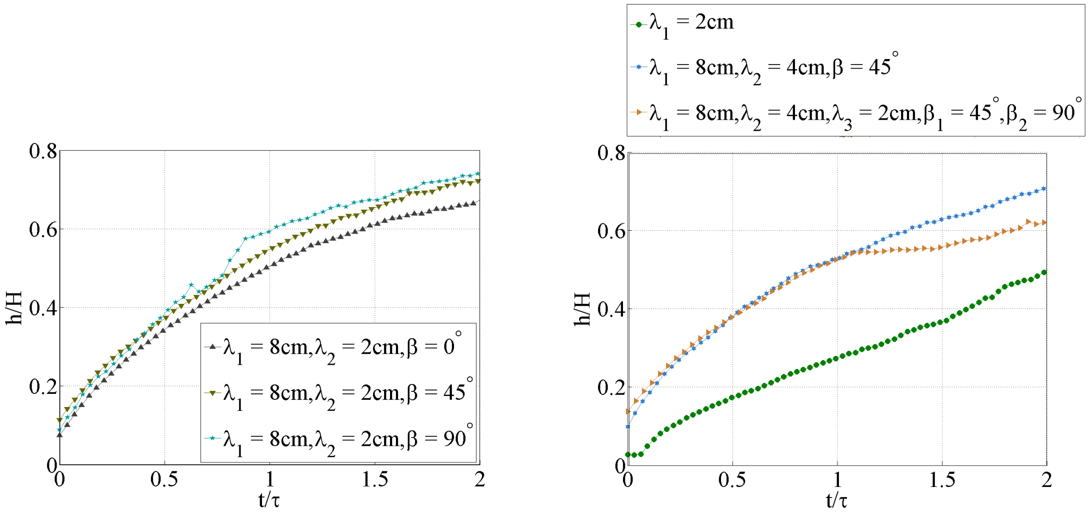

(c) Binary-mode mixing widths with varying phase angle, β

(d) Mixing width for multi-mode *vs.* component single and binary-mode cases

Figure 4.11: Calculated mixing with (h) vs. non-dimensionalized time. Figure taken from Kuchibhatla & Ranjan (2013a).

A discussion of the mixing rate is provided here. The mean square of density gradients or mixing rate is calculated from non-dimensional concentration (see Su & Clemens (2003)), or equivalently, density plots obtained from ensemble averaged images. It is defined as $\chi_{mean} = \int_0^x \int_0^y \chi(x, y, t) dx dy = nU_{mean} \int_0^y \chi(y) dy$ (units of $\mathrm{cm}^2\mathrm{s}^{-1}$) for the total ensemble averaged image, using the Taylor's hypothesis ($x = U_{mean} t$). From the analytical mixing model of Abarzhi et al. (2005) for miscible fluids at low Atwood numbers, a definition of the non-dimensionalized mean square of density gradients rate on dimensional grounds can be defined such that $\chi^*_{mean} = \chi_{mean}/\nu_{mean}$ depends only on the non-dimensional density field. The total time of imaging is equal to the number of images, n, as they are taken one second apart. Plots of χ^*_{mean} are shown in Figures 4.12(a)-4.12(d). Tomkins et al. (2008) and Jacobs (1992) used a formulation for vortex induced mixing in shock-bubble interactions based on Marble (1985). Measuring the velocity field induced by the flapper would provide a good measure of the vorticity effects introduced by the flapper. In the presence of high vorticity induction by the flapper mechanism, the time-scales defined by Marble (1985) might become comparable to the RTI time-scale, and the flow physics might be effecting the RTI development significantly.

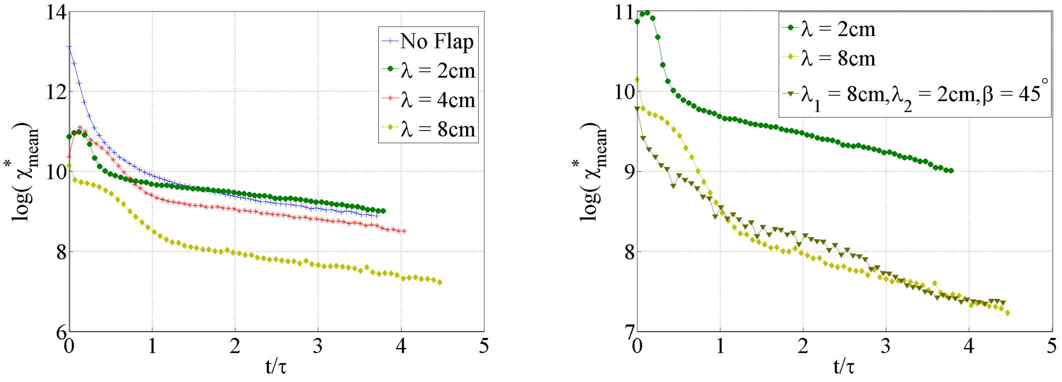

(a) χ^*_{mean} for single-mode cases

(b) Binary-mode χ^*_{mean} vs. component single-mode cases

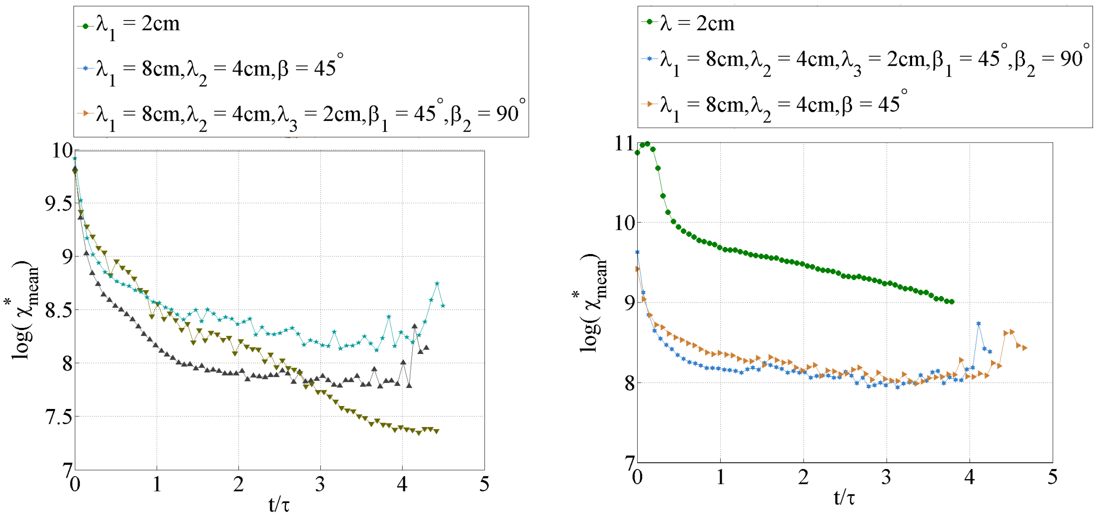

(c) Binary-mode χ^*_{mean} with varying phase angle, β

(d) χ^*_{mean} for multi-mode vs. component single and binary-mode cases

Figure 4.12: Calculated mixing rate (χ^*_{mean}) vs. non-dimensionalized time. Figure taken from Kuchibhatla & Ranjan (2013a).

The total mixing rate data is smoothed using a local regression (with a span of 21 pixels), so that the noise is filtered and data can be better visualized. It can be observed from Fig. 4.12 that the total scalar mixing rate is greatest at the beginning of the mixing layer, i.e. in the vicinity of the splitter plate, and drops down exponentially. This drop continues until the mixing rate is proportional to the viscous mixing rate governed by the kinematic viscosity. As the plots are only provided until $t^* = 3.5$, the mean mixing rate steadily drops towards viscous mixing rate governed by ν_{mean}. Also, it can be seen from Fig. 4.12(a) that the mixing rate is initially larger for the smaller wavelengths, as there is a steep concentration gradient over a small region, i.e. greater propensity for mixing. Case 1, which corresponds to no flapper motion, does not follow the pattern because of the inherent wavelengths in the Water Channel system. As observed in the work of Mueschke (2004), the dominant wavelengths in the Water Channel system (without any flapping of the interface) is around 3.78 cm, based on DNS simulations of scalar concentration and temperature RTI. Thus, case 1 corresponds to a quicker mixing rate than that of case 2, which has an input wavelength of 2 cm. From Fig. 4.12(b), the presence of the smaller wavelength results in decreasing the mixing rate rapidly at the initial stages, such that the larger wavelength dominates the mean mixing rate at later times. From Fig. 4.12(c), the effect of phase difference is observed by the slight variations in mixing rate with time. For the cases 7-9, Fig. 4.12(d) shows some differences between the mean mixing rates computed from ensemble averaged images.

The mean mixing rate varies with phase angle β in the earlier stages, as well as in later stages. Whereas, for $\beta = 0°$ the mixing rate seems to flatten out asymptotically at later times, the slope of the asymptotic mixing rate for $\beta = 45°$ is negative, while that for $\beta = 90°$ is positive. From Figures 4.9(b) and 4.9(d) that the spikes are leaning opposite to the direction of the convective flow for $\beta = 45°$, while they are leaning forward for $\beta = 90°$. As mentioned earlier, the leaning angle, δ results in an equivalent shear on the convective flow. It is proposed that scalar dissipation at late-time increases because of the equivalent shear applied in the direction of the convective flow, whereas it is reduced when equivalent shear is in the direction opposite to the convective flow.

Figure 4.12(d) showing multi-mode mixing rate is in agreement with the observations from binary-mode, i.e. the smaller wavelengths decrease the mixing rates quickly at initial times. A linear fit to log χ^*_{mean} with non-dimensional time, t^*, given in Eqn. 4.6, is performed for each case within the time range of $t^* = 2.0$-3.5, and the values are reported in Table 4.4.

$$\log(\chi^*_{mean}) = d_1 t^* + d_2 \tag{4.6}$$

Table 4.4: Mixing rate analysis: Linear fit parameters. Eqn. 4.6 is used for cases in Table 4.3. Table taken from Kuchibhatla & Ranjan (2013a).

Case #	Max. χ_{mean} ($\times 10^3$ cm^{2}s^{-1})	Min. χ_{mean} (cm^{2}s^{-1})	Slope, d_1	Ordinate, d_2
1	1.765	50.150	-0.289	9.947
2	1.036	47.518	-0.252	9.981
3	1.051	29.180	-0.261	9.584
4	0.465	23.784	-0.282	9.338
5	0.244	9.844	-0.395	8.775
6	0.210	10.291	-0.280	8.513
7	0.159	18.574	0.043	7.746
8	0.152	12.160	-0.382	8.914
9	0.171	26.128	0.060	8.094
10	0.132	22.319	0.105	7.765
11	0.103	23.330	0.106	7.810

The slopes of the single-mode cases stay almost constant within the range of -0.289 to -0.252. From the binary-mode cases, addition of a smaller wavelength decreases the slope, whereas changing the phase angle changes the slope considerably. The larger wavelengths require longer times to reach asymptotic values, and therefore, large amount of errors are associated with these cases. For cases 7-11, there is considerable fluctuation in the mixing rate, and therefore, the linear fit might not be an accurate estimate of asymptotic mixing rate. By measuring the total mixing rate from concentration fields, an estimate of the density distribution and rate of mixing due to the nature of IC is obtained. Using larger initial wavelengths results in smaller scalar mixing rates, but the magnitude of the wavelength does not affect the scalar mixing rate for single-mode cases. From Fig. 4.12(b), the addition of second wavelength reduces the initial scalar mixing rate, but does not significantly affect the mixing rate at later times. Whereas mixing rate is independent of phase angle at $t^* < 0.1$, there seems to be distinction in mixing rate at other times, as supported by Fig. 4.12(c). Overall, a clear trend in mixing rate variation due to phase difference cannot be achieved from the figure. Figure 4.12(d) shows the multi-mode scalar mixing rate vs. its component binary-modes. The trend is very clearly in agreement with the earlier observations made from figure 4.12(b), i.e. the overall mixing rate seems to be following the binary-mode case closely.

4.2.1 Comparison with potential flow model

Using Goncharov's model for bubble evolution (4.7), bubble growth is calculated for single-mode ICs, given by the Equations 4.7, 4.8 and 4.9. The comparison in Fig. 4.13 shows that Goncharov's model predicts a higher growth rate compared to experimental data, which may be ascribed to the nature of experimental ICs, i.e. the presence of inherent modes. Also, the symmetry of the experimental bubbles is broken due to the convective nature of the flow along the streamwise direction. However, it must be remembered that Goncharov's model assumes the potential flow behavior, which is an idealization. Apart from this, the Taylor's hypothesis is also assumed in the current study, which is valid for low shear rates only.

$$h(x,t) = h_0(t) + h_2(t)x^2 \tag{4.7}$$

$$\begin{aligned} \ddot{h_0}(t)\frac{k^2 - 4A_t k h_2(t) - 12A_t h_2(t)^2}{2(k - 6h_2(t)} &= -A_t g h_2(t) \\ &\quad - \dot{h_0}(t)^2 k^2 \frac{(4A_t - 3)k^2 + 6(3A_t - 5)k h_2(t) + 36A_t h_2(t)^2}{2(k - 6h_2(t)^2)} \end{aligned} \tag{4.8}$$

$$h_2(t) = -\frac{k}{6} + \left[\frac{k}{6} - h_0(t)\frac{k^2}{2}\right] e^{-3k[h_0(t)-h_0(0)]} \tag{4.9}$$

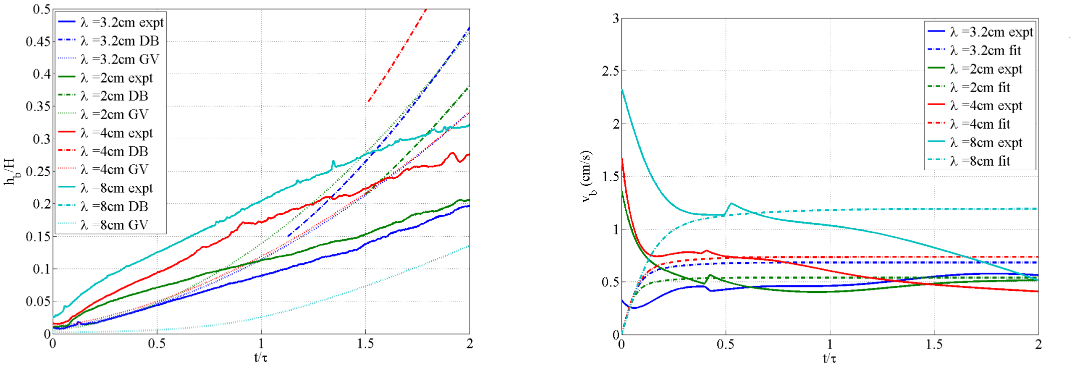

(a) Bubble growth

(b) Bubble velocity

Figure 4.13: Comparison of h for single-mode cases.

4.2.2 Scales of the flow

From the plots of mixing width in Fig. 4.11, plots of variation of Reynolds number based on mixing width, as given in Cabot & Cook (2006) is calculated by $Re = (h\dot{h})/\nu_{mean}$, given the mean kinematic viscosity, v_{mean}. Since mixing width is obtained from image analysis, in spite of the presence of a very uniform image background, any fluctuations in the image data correspond to very large fluctuations in the gradient of h. To address this difficulty, the mixing width data is smoothed once using the robust LOESS (Local regression using linear least squares and a 2nd degree polynomial model) in MATLAB® where local regression of data is performed using linear least-squares and a second order polynomial. Further, $\dot{h}$ is obtained by taking a central difference approach: the neighboring values of h are used for calculating the gradient. Plot of Re for single-mode cases shown below in Fig. 4.14 for single-mode cases shows increasing mixing width with initial wavelength.

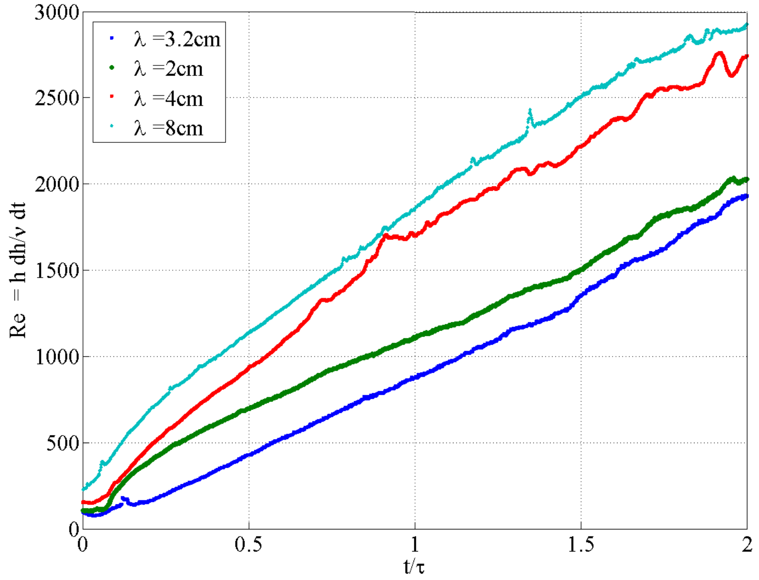

Figure 4.14: Mixing Reynolds number for single-mode cases.

4.2.3 Saturation behavior

Saturation growth rate constant, α calculated from mixing width is reported here. Calculated α from height data is plotted for the above categories of cases in the Fig. 4.15. As can be seen, towards the end of the saturation region, the profile relatively flattens out. The two different methods for calculating α are the Ristorcelli-Clark (RC) method and the Moving Window (MW) method. Using the MW method is highly inconsistent, since the size of the window affects the values by a significant amount. Also, the measured αs using this method are consistently lower than for the RC method, for cases 6-10.

In the saturation growth stage, where the bubble/spike height varies as $h_b = \alpha A_t g t^2$, α is calculated by the MW method, which calculates a local, moving average within the window width. Thus, this technique is subjective to the number of pixels comprising the width of the window, and maybe inaccurate. For all cases, variation of α with time is shown in Fig. 4.15. From these plots, the region of saturation for each case can be identified, leading to a discussion of the onset of saturation as a function of initial modal composition. A plot of case-wise variation of α for all cases using the MW method is given in Fig. 4.15. It can be seen that α values lie around 0.02-0.09. From Ramaprabhu et al. (2012) and Lawrie & Dalziel (2011), experimental αs are greater than those predicted numerically in general. This is attributed to the three-dimensionality of the ICs in experiments, uncertainties in experimental data and the inaccurate diffusion mixing in simulations. A previous measurement of α for Water Channel experiments based on high-resolution LOS images also recorded values within the range of 0.06-0.10 (see Kuchibhatla (2010)).

Saturation regions in ensemble averaged volume fraction images are identified from the variation of α by the RC method. A quadratic curve is then fit to the total

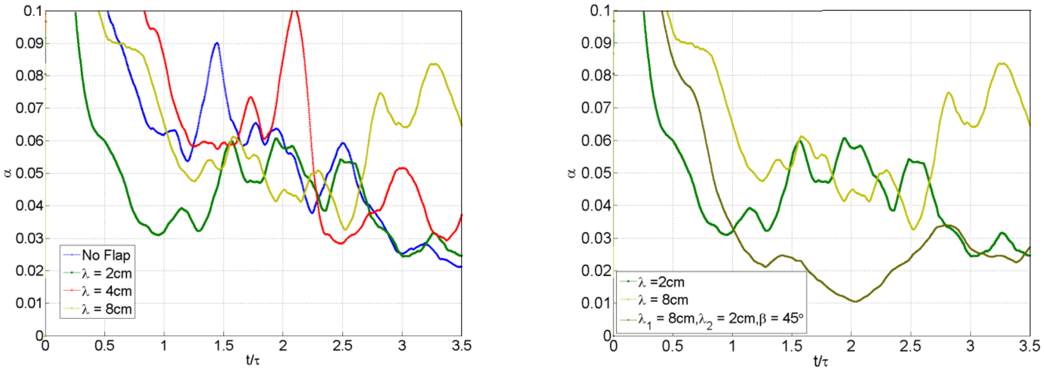

(a) Single-mode cases

(b) Binary-mode vs. its component single-mode cases

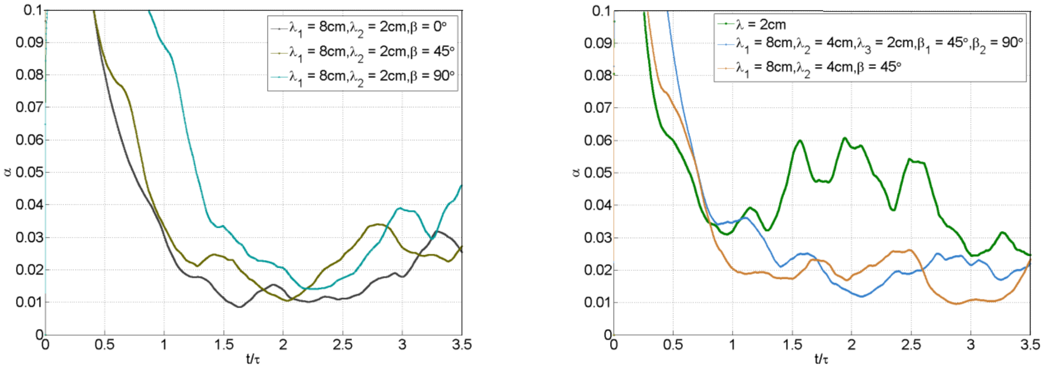

(c) Binary-mode with varying phase angle, β

(d) Multi-mode vs. its component binary and single-mode cases

Figure 4.15: α variation for select cases.

mixing width in the saturation region, to get the form $h_{sat} = c_1x^2 + c_2x + c_3$. Using Taylor's hypothesis, and using $x = U_{mean}t$, parameters α and time corresponding to beginning of saturation region (where $h_{sat} = 0$) can be obtained from this fit. The coefficients and parameters are presented in Table 4.5, while the variation is plotted in Fig. 4.16.

Table 4.5: Coefficients of the parabolic fit to the saturation regime, $h_{sat} = c_1x^2 + c_2x + c_3$.

Case #	C_1 (cm^{-1})	C_2	C_3 (m)	t_{offset} (s)	α_{fit}
1	0.0018	0.1929	1.0694	2.261	0.0254
2	0.0100	0.8923	7.7006	4.450	0.1342
3	0.0050	0.5870	1.6987	4.171	0.0581
4	0.0052	0.8203	8.3977	5.710	0.0600
5	0.0068	0.7321	1.7154	4.448	0.0965
6	0.0034	0.5331	6.5209	4.544	0.0407
7	0.0100	0.3905	9.514	3.540	0.0423
8	0.0105	0.9362	1.31642	4.571	0.1377
9	0.0061	0.6414	6.9671	4.095	0.0764
11	0.0041	0.5310	6.5507	4.126	0.0578
12	0.0006	0.2418	10.6232	4.940	0.0069

Jacobs (1992) and Tomkins et al. (2008) obtained a formulation for time for a vortex interaction with an incoming shock (based on Marble (1985)) that depends upon the distance between the vortex and annulus being mixed, and the vortex strength. They observed an inverse dependence on vortex diameter and -2/3rd power dependence on vortex strength. Even though it is assumed that the flapper motion increases local fluid stream speeds minimally, measuring the circulation induced by the flapper would provide a good measure of the vorticity effects introduced by the flapper. In the presence of high vorticity induction by the flapper mechanism, the time-scales defined by Marble (1985) might become comparable to the RTI time-scale

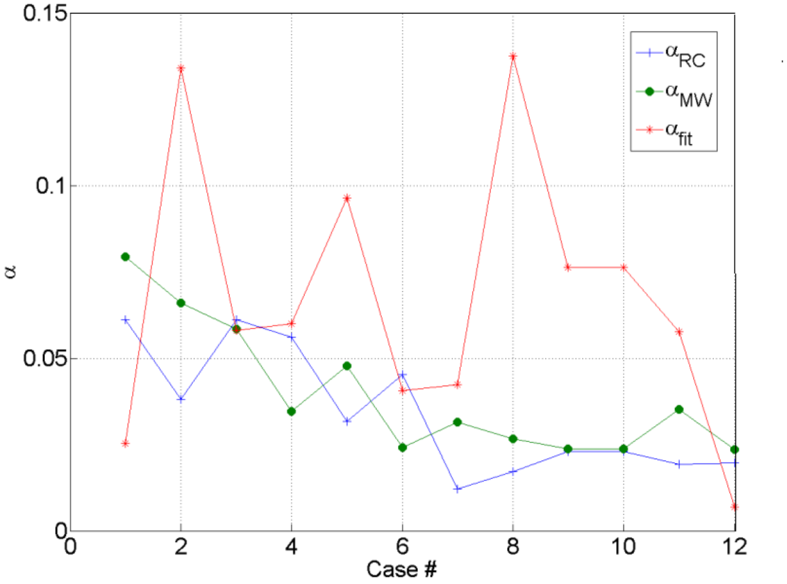

Figure 4.16: Variation of α with IC type using different methods.

(defined later in this dissertation), and the flow physics might be effecting the RTI development significantly.

4.2.4 Buoyancy-Drag (BD) model study

Using the Buoyancy-Drag (BD) model, a study of the mixing behavior is reported here. Experimental parameters for each case are listed in Table 4.6. However, plots are presented only for single-mode cases. Cheng et al. (2000) have performed an analysis of the dependence of bubble and spike α on the drag coefficient, C, and added mass diffusion coefficient, k_b, and concluded that the shape of the bubble or spike will affect growth of the RTI mixing layer, and therefore, α. The ratio α_s/α_b (i.e. of spike and bubble) is found to vary with A_t. It is well documented that the ratio is very close to 1 for low Atwood numbers such as in this dissertation, *i.e.* bubbles and spikes are assumed to grow symmetric with respect to the splitter plate. The definition of drag coefficient, $C = (A_t - 1 - k_b - k_b A_t + 1/\alpha_b)/(2(1 + A_t))$, is used for cylindrical and spherical bubbles with $k_b = 1.0$ for a cylinder. Here, C, k and α for bubbles and spikes are used interchangeably. Drag coefficients for phase difference cases are listed below, with some interesting points of note. C is largely dependent on the added mass coefficient, k and α. The saturation growth constant obtained by the RC, MW and curve fit methods are all subjective to the smoothing technique applied, the window size employed and identification of the saturation regime. The Rayleigh-Taylor mixing layer developing due to multi-modal initial conditions exhibits leaning of the flow structures. Thus, bubbles and spikes are asymmetric, causing a variation in drag coefficient.

In previous studies using the coupled BD formulation, viz. by Youngs (1989), the drag coefficients are required from experimental data. Kucherenko et al. (1991), Dimonte (2000) and Cheng et al. (2000) used the 'Tube model' of Rayleigh-Taylor mixing that assumes the bubbles and spikes as being independent cylinders. Youngs proposed the use of added mass-coefficient, k_b, which depends on the shape of the bubbles and spikes. Dimonte (2000) calculated $C = 3.67$ from a coupled model, whereas using the tube model, C is determined to be 5.5 for the case of no initial input perturbations at the interface. Due to molecular mixing in the current experiments and the inherent characteristic wavenumbers of the Water Channel setup, greater drag coefficient values are predicted. Further, for multi-modal cases, greater drag coefficients are predicted due to the shape approaching elliptical features. Table 4.6 shows the data is consistent with the prediction.

Experimental mixing width data is compared with analytical models in literature, such as by Abarzhi (2010) and Dimonte (2004). While the model by Abarzhi assumes a Momentum Balance approach to calculate the height of the bubble or spike at each A_t, Dimonte's approach is based on the BD approach, where the simplified Navier-Stokes equations are used to calculate the bubble/spike height with varying shape and thereby, viscous drag. A comparison of the single-mode bubble height between experiments and these two models is presented in Fig. 4.13. While calculating h_b by the BD model, C is obtained from an approximate formulation by Clift et al. (2005) for an elliptical bubble in an ambience. The shape of the bubbles given in Figures 4.49, 4.50 and 4.51 are used to calculate the ellipticity, e, which is then used for the drag coefficients, along with the density ratio, $R = \rho_h/\rho_l > 1$. Table 4.6 lists the BD model parameters for each case.

Table 4.6: Drag coefficients.

Case	Drag coefficient, bubble			Drag coefficient, C		
#	RC	MW	Curve fit	RC	MW	Curve fit
1	7.16	5.29	18.69	6.66	4.79	18.19
2	12.07	6.56	2.72	11.57	6.06	2.22
3	7.15	7.52	7.60	6.65	7.02	7.10
4	7.87	13.44	7.32	7.37	12.94	6.82
5	14.69	9.44	4.17	14.19	8.94	3.67
6	10.03	19.65	11.27	9.53	19.15	10.77
7	40.07	14.80	10.80	39.57	14.30	10.30
8	28.02	17.67	2.63	27.52	17.17	2.13
9	20.33	19.93	5.54	20.16	19.43	5.04
11	24.90	13.16	7.64	24.40	12.66	7.14
12	24.35	20.11	70.89	23.85	19.61	70.39

A Comparison of this data with a recent study on Rayleigh-Taylor experiments by Tsiklashvili et al. (2012), where a broadband multi-mode initial condition is employed for paramagnetic liquids, is given in Fig. 4.17. Froude number in the self-similar region is a measure of the terminal velocity of the mixing layer when compared with gravitational accelerated velocity of a particle in vacuum, after the same duration of time. It is calculated from $Fr = v_b\sqrt{\frac{(1+1/A_t)}{gd}}$, where v_b is defined above. d is the bubble diameter, which can be treated as equivalent to the wavelength of the IC, hence $d = \lambda$ is used. The cases corresponding to higher wavelength have not completely saturated yet.

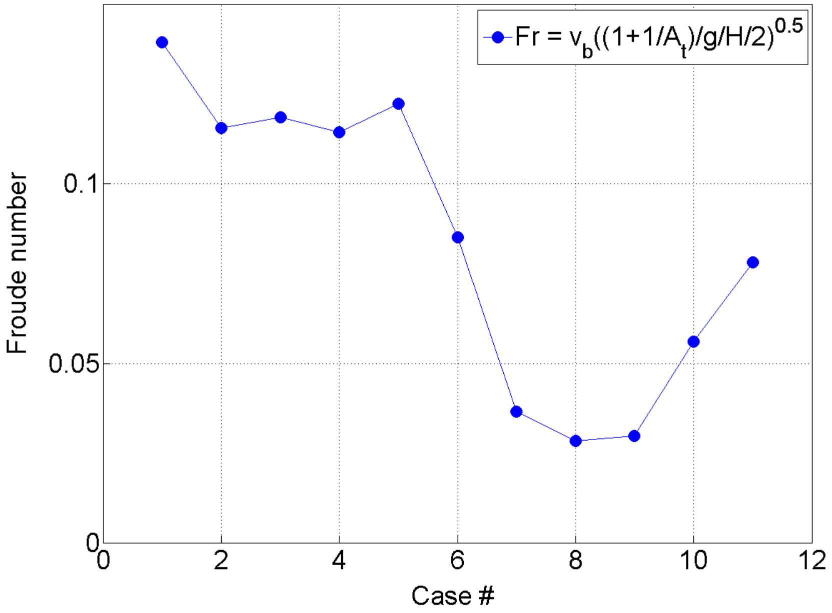

Figure 4.17: Variation of Fr with IC type.

4.3 Thermocouple measurement results

Table 4.7: Experimental parameters for thermocouple measurements.

Case #	λ_1 (cm)	λ_2 (cm)	λ_3 (cm)	λ_{eq} (cm)	β_1 (°)	β_2 (°)	A_t ($\times 10^{-3}$)
1	0	-	-	0	-	-	1.28
2	2	-	-	2	-	-	1.60
3	4	-	-	4	-	-	1.65
4	4	2	-	4	45	-	1.62
5	4	4	-	4	45	-	1.50
6	8	-	-	8	-	-	1.81
7	8	2	-	8	0	-	1.54
8	8	2	-	8	45	-	1.63
9	8	2	-	8	90	-	1.72
10	8	4	2	8	45	90	2.08
11	8	4	-	8	45	-	1.81
12	8	2	-	8	180	-	1.81

Using thermocouples, the initial set of experiments are performed to compare molecular mixing due to the thinner splitter plate with previously published data, whereas the next set of experiments focused on power spectra for the initial condition study. As part of the initial study, instantaneous temperature is obtained for two points at each streamwise location, at two locations of $x/H = 0.077$ and 0.908 respectively, for ten cases in all, as specified in Table 4.7. For these cases, a temperature difference of $\Delta T = 7.0$ °C is setup. Parameters f_h, f_l, B_0 and B_2 are calculated at each point for the list of initial conditions specified in §4.7.

Corresponding to a Reynolds number based on mixing layer given by $Re_{mix} = h\dot{h}/2\nu$ in Youngs (1984) and Snider & Andrews (1994), the Kolmogorov microscale for RTI is given by $\eta_v = hRe_{mix}^{-3/4}/2$ (see Wilson & Andrews (2002)). Also, the Batchelor thermal diffusive length-scale is related to the Kolmogorov viscous length-scale by $\eta_D = \eta_v Pr^{1/2}$, where Pr is the Prandtl number for water (≈ 7). For all experiments it is necessary to resolve η_D in order to measure mixing completely. The maximum frequency associated with this smallest scale to be resolved is given by $\omega_{max} = U_{mean}/2\eta_D$. As the thermocouple probe diameter (d_{probe}) is 0.0076 cm and the smallest Batchelor scale for the worst case is 0.0026 cm, the thermocouple is not small enough to capture the smallest Batchelor scale (as $2d_{probe} > \eta_D$). Thus, the Nyquist criterion for spatial resolution is not satisfied at $x/H = 0.908$. For this location, we can assume that all scales of significance will not be measured during experiments. Table 4.8 lists these parameters for the worst-case scenario (corresponding to the smallest Batchelor scale to be measured, which is for case 3 in table 4.7 at location 1 of $x/H = 0.077$ and location 2 with $x/H = 0.908$, in order to check the temporal resolution required to resolve the Batchelor scales.

Table 4.8: Viscous (Kolmogorov) and thermal diffusive (Batchelor) length-scales for case 3.

Parameter	Value
A_t	1.80×10^{-3}
h at $x/H = 0.908$	16.24 cm
$Re_{mix},_2$	3.14×10^{3}
$\eta_v,_2$	0.0069 cm
$\eta_D,_2$	0.0026 cm
$\omega_{max},_2$	882 Hz

To validate the new Water Channel setup and observe the effect of thinner splitter plate, plots of f_h, B_0, B_2 and θ are compared to data from Wilson & Andrews (2002) and Ramaprabhu & Andrews (2004), and are presented in the appendix, for case 1 in table 4.3.

Centerline values ($y = 0$ and $z = 0$) of θ for each of the cases at streamwise

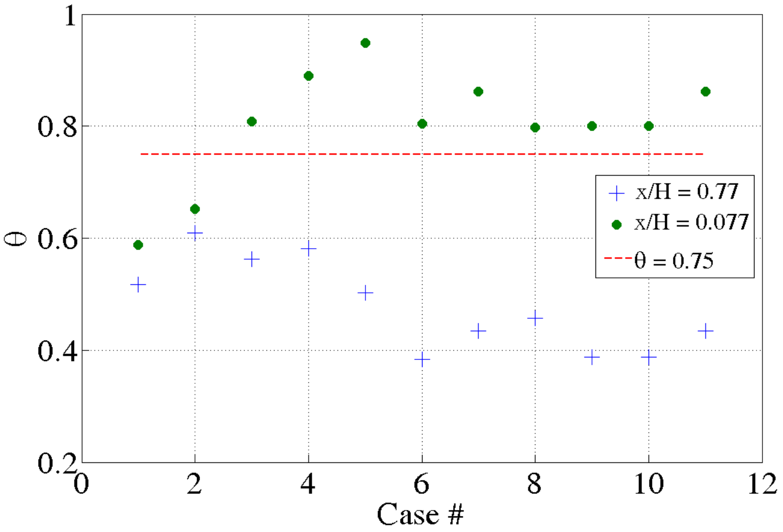

Figure 4.18: Casewise variation of molecular mixing parameter, θ.

locations given by $x/H = 0.077$ and 0.77 respectively are plotted in Fig. 4.18. The corresponding t^* at each of these locations lies within the ranges $t_1^* = 0.13$-0.16 and $t_2^* = 1.33$-1.57, because the Atwood numbers are different between cases. At early-times, i.e. t_1^*, less molecular mixing is measured for all cases, which increases with time, in agreement with literature (see Andrews et al. (2012)). For the no-flap case, measured θ is in good agreement with previously reported asymptotic values as specified earlier. The deviation of the rest of the cases from the case with no initial condition is primarily due to the streamwise locations. Only cases 1-4 have saturated towards the end of the Channel, with the no-flap case 1 saturating earliest. For cases 2-5, more measurements downstream of the splitter plate are required to obtain asymptotic θ. For the rest of the cases 6-10, the larger wavelengths need a wider test section for the Channel, for the flow development into the saturation regime. At any x/H, for single-mode cases, increasing the wavelength decreases θ as observed from Fig. 4.18 (cases 1-3 and 6). This is because the larger wavelength cases corresponding to $\lambda = 8$ cm has not saturated, as observed during the experiments. For binary-mode initial conditions, adding an additional smaller wavelength increases θ (e.g. case 4 vs. case 3, case 7 vs. case 6, case 10 vs. case 6). This is in agreement with total mixing width measured during experiments.

4.3.0.1 Quality of mixing

Sample temperature data measured by thermocouples at downstream locations x_1 and x_2 is given in Figures 4.19 and 4.20 respectively. A discussion of the addition of a second smaller wavelength to the single-mode produces an interesting behavior. As the smaller wave is superimposed, leaning of the structures is observed, which delays the saturation regime, and therefore observed θ at the same non-dimensional time is smaller. This could be attributed to the time-scale, τ, being independent of initial λ. Therefore, a suitable time-scale needs to be defined that takes into account the variation in θ as well as β. Traditionally, the largest wavelength is selected as the dominant one (see Mueschke et al. (2006) and Dimonte (2004)). It is suggested to use a time-scale as used in Cabot & Cook (2006). The interesting case of addition of a second comparable wavelength (such as in case 5 vs. case 3) maybe explained due to competition among the modes resulting in less molecular mixing. Finally, multi-mode θ is less than the component binary and single-mode θ (from case 9 vs. cases 2 and 10). The same logic for binary-mode cases can be extended to multi-mode.

In order to check the symmetry of the mixing layer, plots of the skewness of temperature, $S_T = \langle T'^3 \rangle / \langle T'^2 \rangle^{3/2}$ is calculated and presented in Fig. 4.21. Similarly, kurtosis given by $K_T = \langle T'^4 \rangle / \langle T'^2 \rangle^2$ is given in Fig. 4.22. Molecular mixing parameters are reported in Table 4.9. The asymptotic θ reaches ~ 0.75 for the no-flap case at location x_2, while the rest of the cases show greater molecular mixing

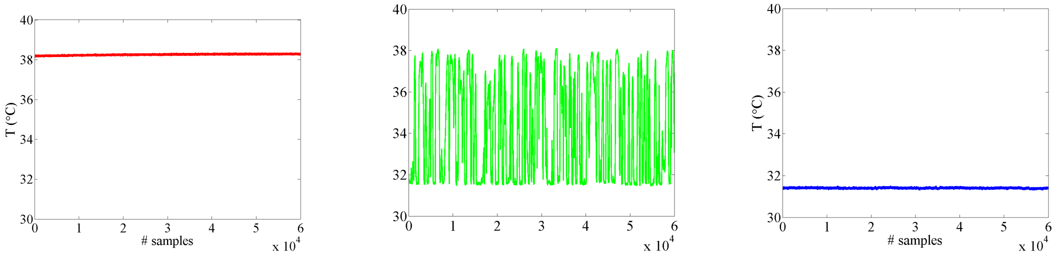

(a) y/H = 0.07 (b) y/H = 0.00 (c) y/H = -0.07

Figure 4.19: Temperature signal vs. y for case 1 at x_1.

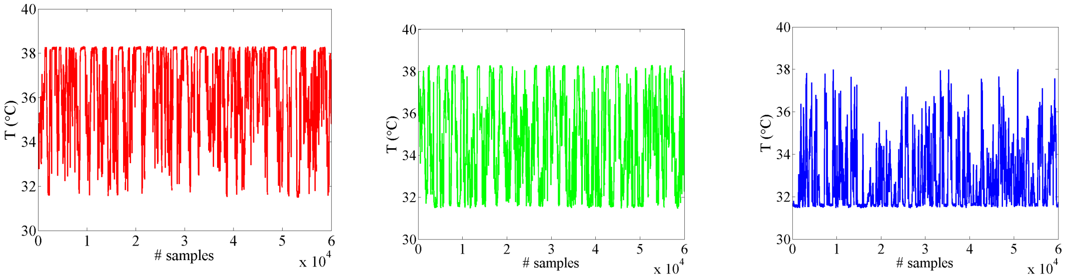

(a) y/H = 0.07 (b) y/H = 0.00 (c) y/H = -0.07

Figure 4.20: Temperature signal vs. y for case 1 at x_2.

parameter, except for case 2. The single-mode case with $\lambda = 2$ cm seems result in lower molecular mixing. The parameter θ is an indicator of the amount of density fluctuations in the system, which includes diffusion as well as turbulent transport. For larger initial wavelengths, greater initial energies and transport is observed in the system. Therefore, larger θ is observed.

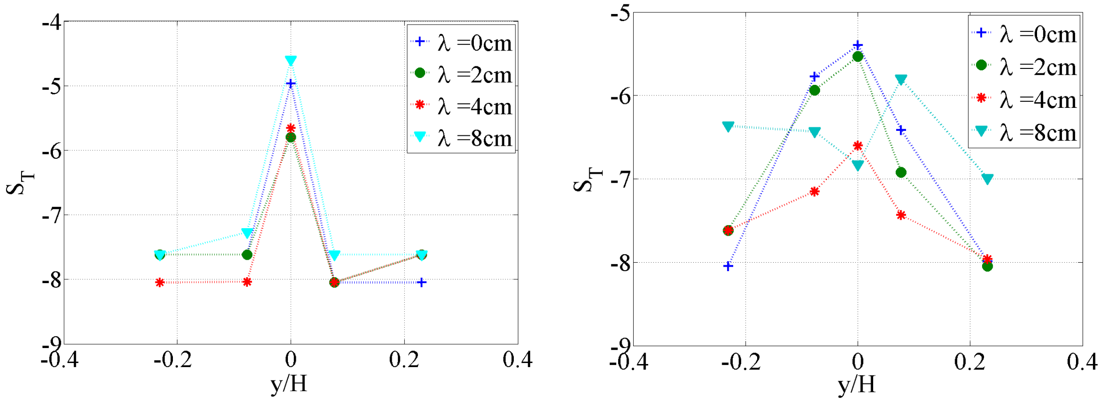

(a) Single-mode cases at x_1

(b) Single-mode cases at x_2

Figure 4.21: Skewness of temperature, S_T vs. crosswise displacement, y/H for single-mode cases.

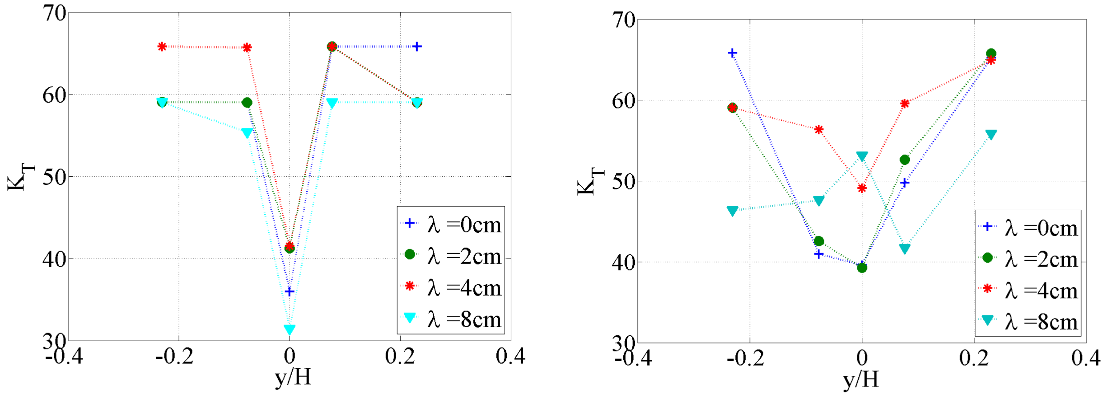

(a) Single-mode cases at x_1

(b) Single-mode cases at x_2

Figure 4.22: Kurtosis of temperature, K_T vs. crosswise displacement, y/H for single-mode cases.

Table 4.9: Mixing variables from thermocouple measurements.

Case	x_1			x_2		
#	B_0	B_2	θ	B_0	B_2	θ
1	0.0730	0.2431	0.6997	0.0638	0.2463	0.7410
2	0.1087	0.2418	0.5504	0.0919	0.2498	0.6323
3	0.1205	0.2435	0.5052	0.0504	0.2494	0.7980
4	0.1718	0.2392	0.2819	0.0473	0.2500	0.8110
5	0.1065	0.2257	0.5284	0.0275	0.2499	0.8898
6	0.1433	0.2478	0.4217	0.0248	0.2420	0.8976
7	0.1752	0.2893	0.2465	0.0483	0.2499	0.8066
8	0.1723	0.2450	0.2967	0.0440	0.2499	0.8598
9	0.1746	0.2450	0.2967	0.0440	0.2499	0.8239
10	0.1612	0.2151	0.2506	0.0562	0.2500	0.775

4.3.1 Transition from 2D to 3D

In 3D miscible RTI in the incompressible limit, where the Boussinesq approximation is valid, a characteristic scale for temperature and velocity in the presence of buoyancy forces, called Bolgiano scale, η_B (given in Eqn. 4.10) is given by Bolgiano Jr (1959) and Obukhov (1959). It was proposed that for $\eta > \eta_B$, the buoyancy force is significant. Therefore, an exponent of 3/5 for velocity, and 1/5 for temperature are proposed. Through high resolution numerical simulations, Boffetta et al. (2012) proposed that η_B is essentially the 'confining' dimension of the system, i.e. the spanwise dimension of a convective Rayleigh-Taylor setup. Above this scale, the mixing width is larger than the confining dimension, thus, transitioning the flow into a Bolgiano scaling, while below the scale, the Kolmogorov-Obukhov scaling is observed. In essence, the Bolgiano scale provides an estimate of the length-scale above which the flow field transitions from 2D to 3D.

$$\eta_B = (\beta_T g)^{-3/2} \epsilon^{5/4} \epsilon_T^{-3/4} \tag{4.10}$$

Here, β_T is the thermal expansion coefficient of the mixed fluid, ϵ is the viscous dissipation rate of kinetic energy and ϵ_T is the dissipation rate of temperature, T. The second order structure function of temperature, $S_2^T(x) = \langle(\delta T(x))^2\rangle$ is calculated along the centerline of the mixing layer at t_1^* and t_2^*, and shown in Fig. 4.23. The solid lines indicate the Kolmogorov scale, while dotted lines indicate the Bolgiano scaling. Using Taylor's hypothesis, we can define the non-dimensional time, $x = U_{mean}t$, which lends the structure function being equal to the autocorrelation function of temperature $T(s) \equiv \frac{\langle T(t)T(t+s)\rangle}{\langle T(t)^2\rangle}$, thereby, Bolgiano length-scale can be calculated.

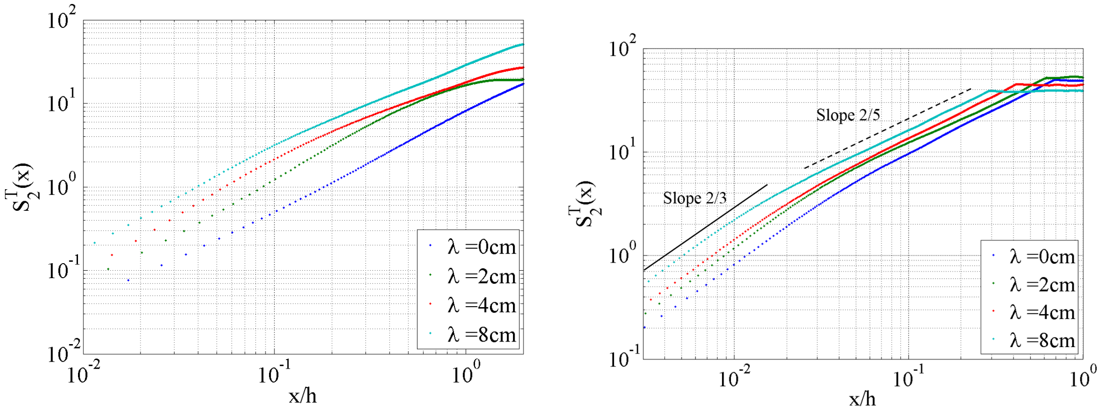

(a) Structure function at t_1^* (b) Structure function at t_2^*

Figure 4.23: Structure functions at times t_1^* and t_2^*.

4.3.2 Statistical analysis of density data

Histograms of density at the centerline of the mixing layer are presented in Figures 4.24, 4.25 and 4.26. All data is taken at two streamwise locations, $x_1 = U_{mean}t_1^*\tau$ and $x_2 = U_{mean}t_2^*\tau$. At initial times, smaller eddies are observed near the center of the mixing layer, which results in the histograms of ρ^* peaking about the average value of 0.5. At late-time, the shifting of the center of gravity of the mixing layer results in the thermocouples detecting more light fluid than heavy fluid. Thus, the peaks shift to the lower densities. Also, greater fluctuations in the mixing layer result in the thermocouple detecting eddies containing pure heavy and light fluid. This general trend is not observed for case 5, where the center of the gravity of the mixing layer has shifted upward. This may be due to the shearing nature of binary-mode cases with comparable wavelengths (i.e. $\lambda_1/\lambda_2 = 1$), which may result in asymmetric growth of the mixing layer. With increasing number of modes (e.g. case 10 vs. case 1), a greater amount of mixing results in higher peak of the density histogram.

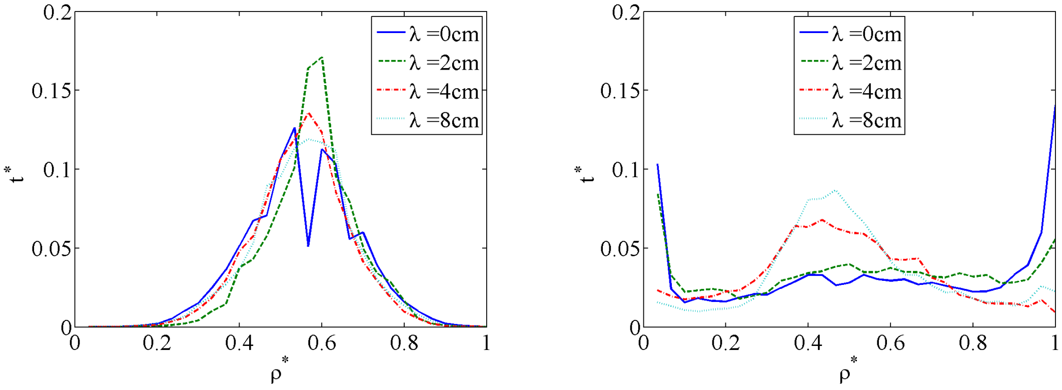

(a) Histogram of ρ^* at x_1

(b) Histogram of ρ^* at x_2

Figure 4.24: Histogram of ρ^* for single-mode cases.

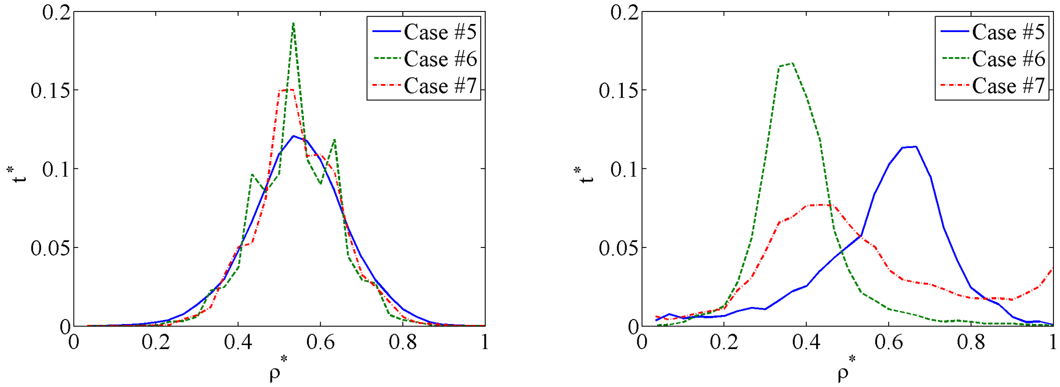

(a) Histogram of ρ^* at x_1

(b) Histogram of ρ^* at x_2

Figure 4.25: Histogram of ρ^* for binary-mode cases.

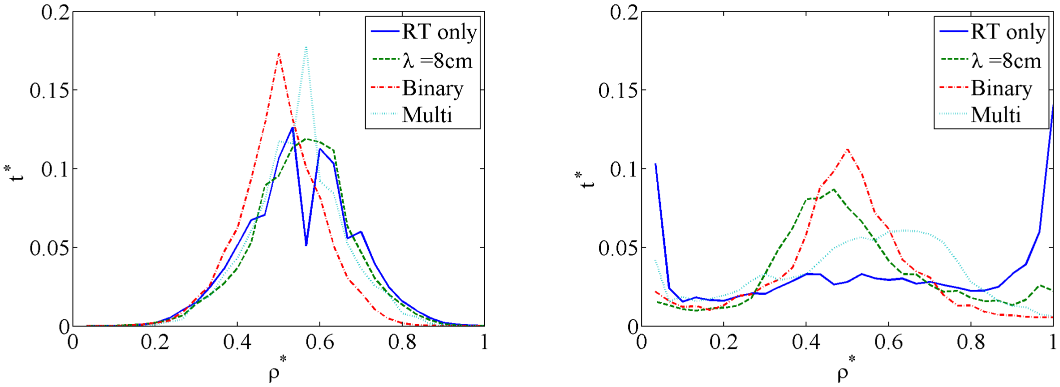

(a) Histogram of ρ^* at x_1 (b) Histogram of ρ^* at x_2

Figure 4.26: Histogram of ρ^* for increasing number of modes.

The density power spectra are presented in Figures 4.27 and 4.28. Compensated power spectra are also given in Figures 4.29 and 4.30. Calculations and details are given in Wilson & Andrews (2002) and Ramaprabhu et al. (2005). Power spectra of measured density is computed for each of the grid points at two streamwise locations (x/H = 0.077 and x/H = 0.77), five crosswise locations (y/H = -0.09, -0.03, 0, 0.03 and 0.09) and three spanwise locations (z/H = -0.231, 0.000 and 0.231) . It should be noted that these spectra are taken at different x_2 locations compared to the molecular mixing measurements. For all cases, temperature data taken at 1kHz at each of these grid points is then converted to density using Eqn. 4.3. The power spectrum of $B_0(\rho)$, $B_0(\omega)$, is calculated by taking the FFT of non-dimensional density, ρ^* and taking the magnitude for the first half of the frequencies. The power of the spectrum, $B_0(\omega)$, as a function of frequency, ω, is plotted for the horizontal centerline i.e. $y = 0, z = 0$ at each streamwise location.

The effect of phase angle is observed by plotting the power spectra for cases 8 and 9, given in Fig. 4.27(b). From the plots, it can be observed that the phase angle does not induce any significant variation in the power spectra. This may be due to the following reasons: *a*) For the given ratio of wavelengths in cases 8 and 9, i.e. 4:1, the effect of the smaller wavelength is to produce a type of 'smearing' as observed in Kuchibhatla & Ranjan (2013a). Thus, only a variation in higher wavenumbers of the spectrum is observed, as supported by Fig. 4.27(b). *b*) Also, the width of the mixing layer $h = h_{f_h=0.95} - h_{f_h=0.05}$ does not vary significantly with β, as found in Kuchibhatla & Ranjan (2013a). The current observations provide support to the theory.

From the histograms of single-mode cases, a lack of symmetry with y at early-time could be observed. This may be due to the offset in the positioning of the thermocouple. However, this asymmetry is further amplified as one approaches greater downstream distance. This is because the mixing layer shifts in the direction of the gravity and there will be an asymmetry of estimated non-dimensional density about the geometric centerline. Lastly, there is insignificant variation of the plots in the Z direction within a bounded region only. Approaching the walls of the Water Channel introduces boundary layer effects that modify these plots at all downstream distances. Based on these plots, it is advisable to take the time-scale based on the largest wavelength of the system as traditionally performed in literature. As the number of modes in the IC is increased, the symmetry of the peaks with the troughs in the autocorrelation is affected. As the large wavelength of $\lambda = 8$ cm still dominates the flow field, the peaks are not affected, however the troughs start to flatten as the small wavelengths start interacting with each other. This is enhanced when the number of modes is increased from 2 to 3 as can be seen in Fig. 4.33.

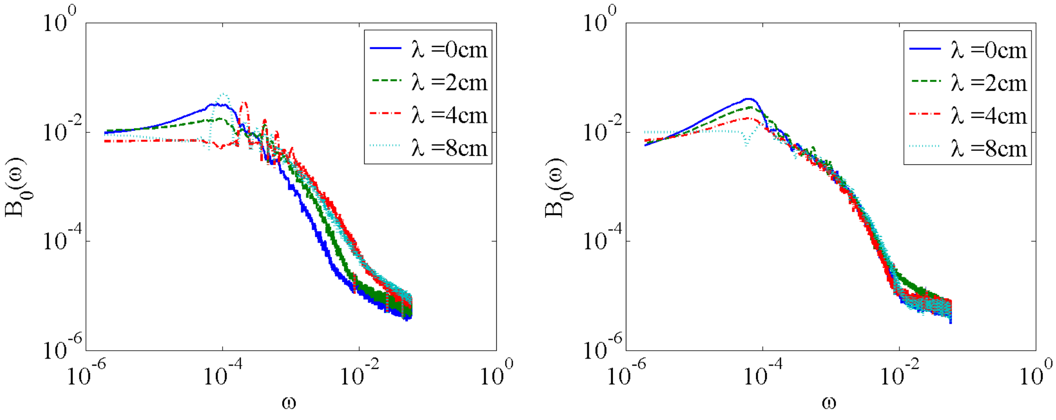

(a) $B_0(\omega)$ for single-mode cases

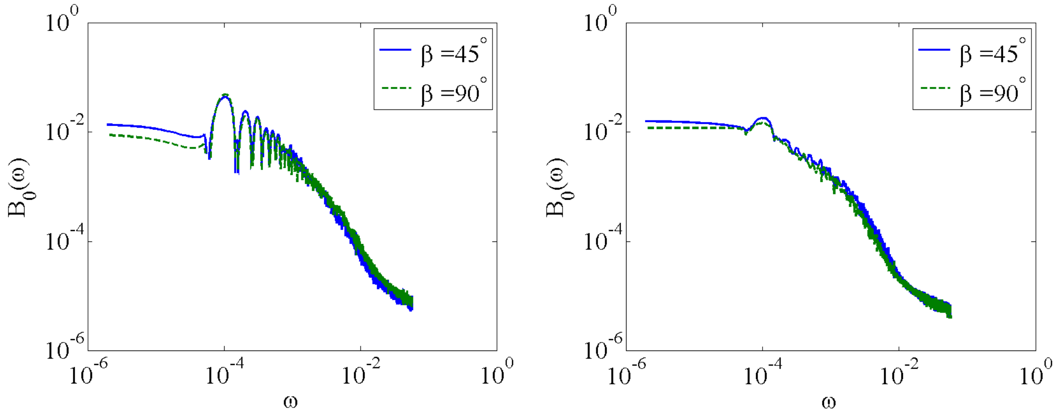

(b) $B_0(\omega)$ for phase angle variation cases

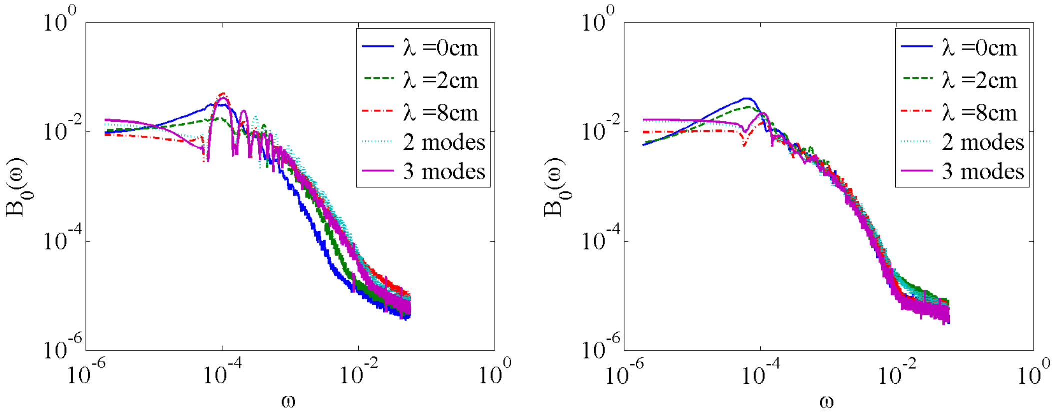

(c) $B_0(\omega)$ for increasing number of modes

Figure 4.27: Density power spectra, $B_0(\omega)$ at different streamwise locations. The left column is at t_1^* and right column is at t_2^*.

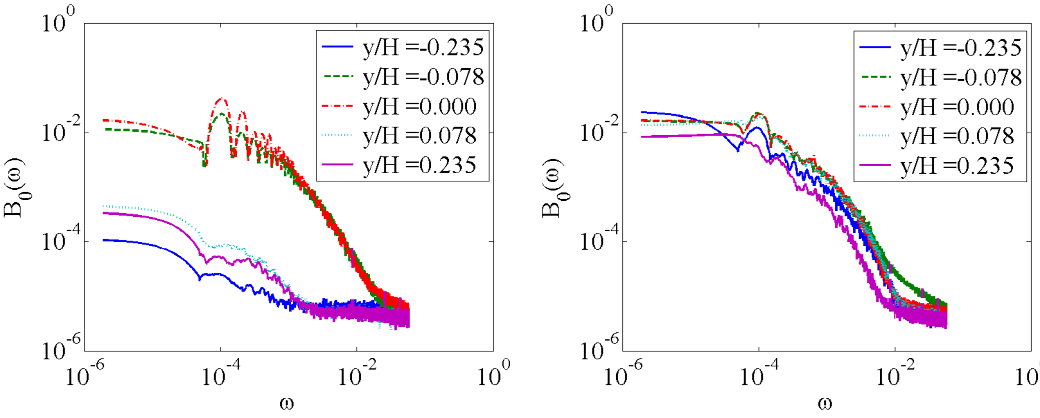

(a) $B_0(\omega)$ for multi-mode case vs. y

Figure 4.28: Density power spectra, $B_0(\omega)$ at different crosswise and spanwise locations for multi-mode case (case 10). The left figure is at t_1^* and right figure is at t_2^*.

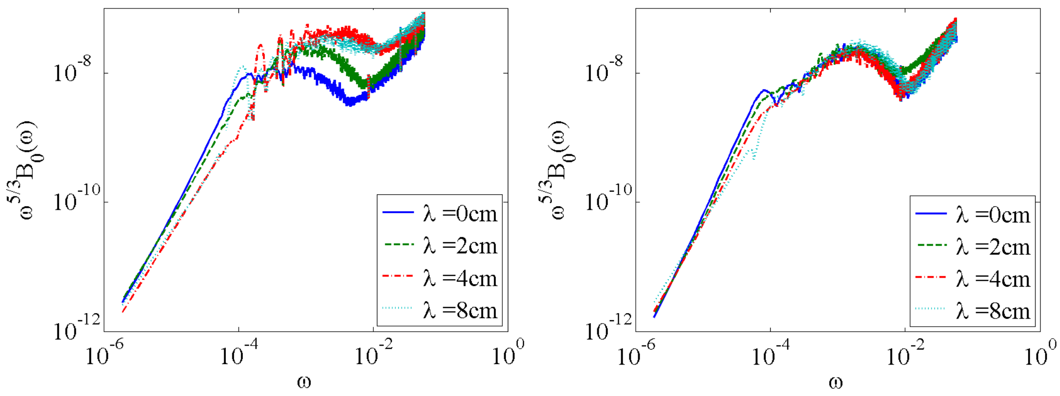

(a) $\omega^{5/3}B_0(\omega)$ for single-mode cases

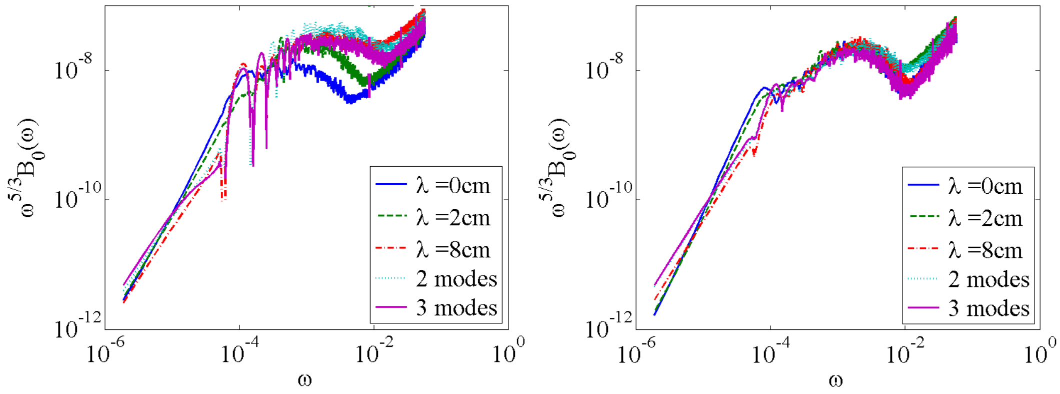

(b) $\omega^{5/3}B_0(\omega)$ for increasing number of modes

Figure 4.29: Compensated density power spectra, $B_0(\omega)$ at different streamwise locations. The left figure is at t_1^* and right figure is at t_2^*.

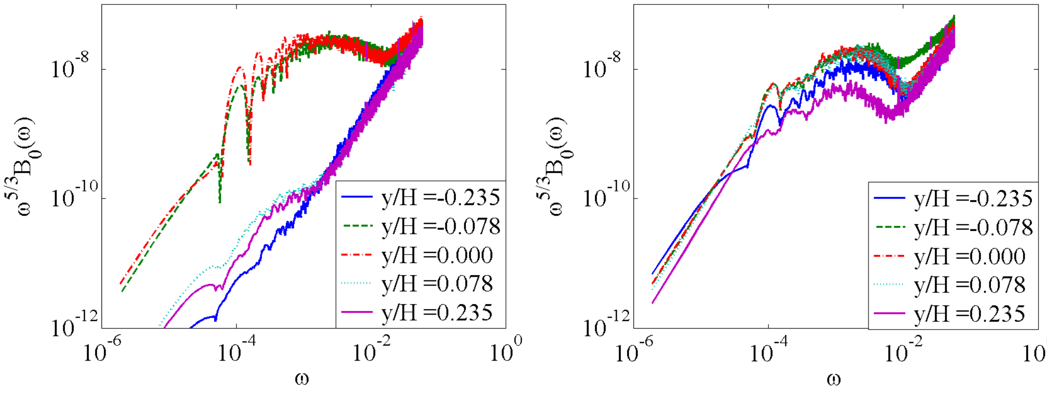

(a) $\omega^{5/3}B_0(\omega)$ for multi-mode case vs. y

Figure 4.30: Compensated density power spectra, $B_0(\omega)$ at different crosswise and spanwise locations for multi-mode case (case 10). The left figure is at t_1^* and right figure is at t_2^*.

4.3.3 Time series analysis

The autocorrelation of ρ^* is calculated by $R_{11}(\rho^*) = \Sigma_{n=0}^{N-m-1} \rho^*_{n+m}\overline{\rho^*_n}$, if $m \geq 0$ and symmetry is used for negative index m. $(m, n) \epsilon [1,\ N]$, where N is the total number of density samples in the interval of observation. This generates a symmetric autocorrelation of density about time lag $l = 0$ s, therefore, only a half of it is plotted. Variation of R_{11} with time lag, l, for different sets of experiments is shown in Fig. 4.31 for single-mode cases, Fig. 4.32 for binary-mode cases, and Fig. 4.33 for multi-mode case respectively . Here, all Figures correspond to the center of the mixing layer, i.e. $y = 0$ cm and $z = 0$ cm. At locations close to the splitter plate, the density strongly correlates to the initial condition, exhibiting periodic peaks with time lag. However, the magnitude of the peaks is reduced with increasing lag, as the correlation with harmonics is reduced. The periodicity at smaller lags is clearly dependent upon the initial wavelength, λ, at location x_1, as given in Fig. 4.31. At the downstream distance x_2, this periodicity is reduced significantly, as only the low frequency waves dominate the flow. The variation in β seems to shift the peak strength or magnitude only. This process continues with downstream distance until the curves completely flatten out, i.e. the flow becomes fully turbulent. This shows that periodicity is a function of wavelength, while the correlation strength depends upon the shape of the IC at the interface.

4.3.4 Observations on thermocouple measurements

Significant points of observation include: *i*) Comparison of the molecular mixing data from the new Water Channel setup is performed with previous data and a decent agreement is observed. *ii*) For single-mode cases, the molecular mixing parameter calculated from temperature measurements at each downstream location increases with increasing wavelength. *iii*) Comparison of centerline θ variation with streamwise

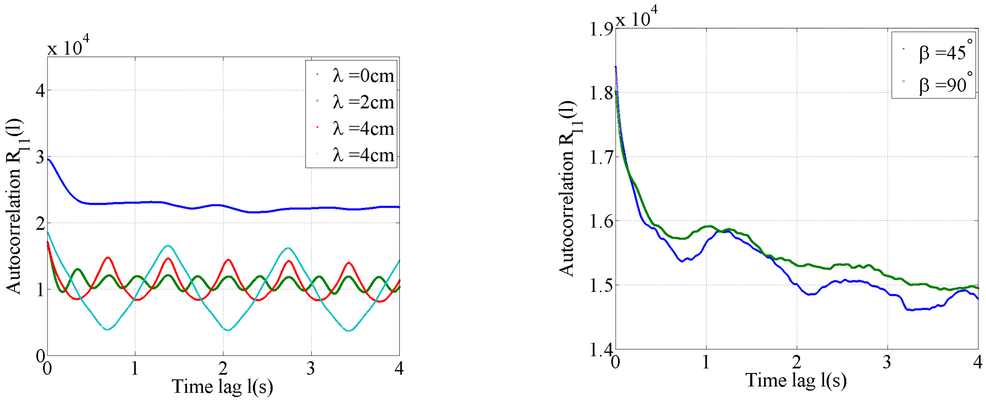

(a) R_{11} at x_1 (b) R_{11} at x_2

Figure 4.31: $R_{11}(\rho^*)$ with time lag, l, at the center of the mixing layer, $y = 0$ and $z = 0$ for single-mode cases.

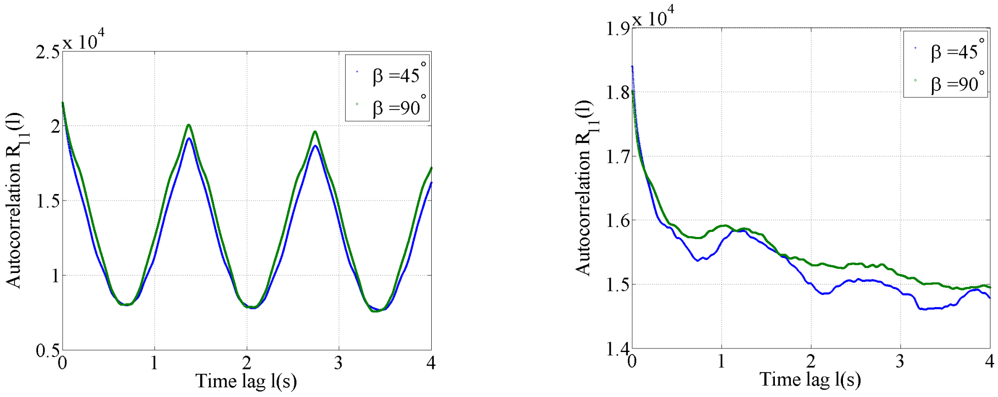

(a) R_{11} at x_1 (b) R_{11} at x_2

Figure 4.32: $R_{11}(\rho^*)$ with time lag, l, at the center of the mixing layer, $y = 0$ and $z = 0$ for phase variation cases.

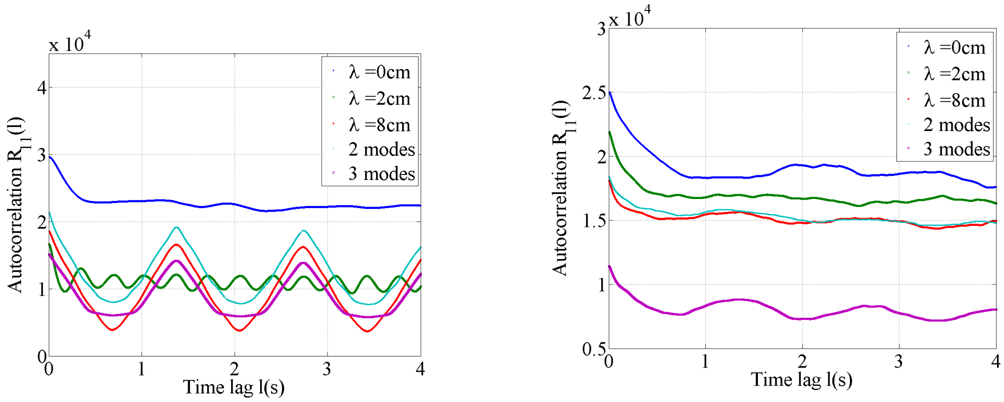

(a) R_{11} at x_1

(b) R_{11} at x_2

Figure 4.33: $R_{11}(\rho^*)$ with time lag, l, at the center of the mixing layer, $y = 0$ and $z = 0$ for multi-mode cases.

location indicates that a greater number of modes increases molecular mixing at the same location. *iv*) The effect of phase angle on molecular mixing is difficult to deduce with only two data points. A more rigorous parametric study is required to understand the effect of phase angle on molecular mixing. *v*) The same trends observed for binary-mode can be extended to multi-mode, i.e. molecular mixing is reduced as number of modes is increased *vi*) A time-scale that takes the initial wavelengths and phase angles into account for the observed delay in saturation is desired.

From the power spectra of the non-dimensional density, additional observations can be made: *vii*) Streamwise variation for case 1 shows that molecular mixing is less at upstream locations along the X-centerline. *viii*) As the mixing width increases, there is little variation in the power spectrum with crosswise distance along the mixing layer. *ix*) Molecular mixing seems independent of spanwise distance, supporting the largely two-dimensional nature of the flow field in the region of interest. *x*) Comparison of the power spectra for single-mode cases shows a strong dependence on initial wavelength at location $x/H = 0.077$, whereas the variation in shape (and slope) is much less pronounced at $x/H = 0.77$. *xi*) Adding a smaller second wavelength of 2 cm to the 8 cm case shows quicker development of the mixing width, therefore, a milder slope for the binary-mode case compared to the single-mode case. *xii*) Increasing the phase angle from 45° to 90° indicates a steeper slope of the power spectrum. This may be due to experimental uncertainty. *xiii*) A similar trend can be observed for multi-mode case 10 when compared to binary-mode case 9.

From the above, it is noted that more data points are required in the vicinity of the centerline ($y = 0$) along the streamwise direction to observe the evolution of the flow. Use of higher resolution diagnostics will help in understanding the effect of ICs on fine-scale mixing. By quantifying the above ICs using such diagnostics, scaling parameters can be constructed and correlations can be drawn between initial wavelengths and turbulent mixing, effectively enabling us to design turbulence.

Table 4.10: List of experiments to study flapper effect.

x/H	Run name	Type	A_t $(\times 10^{-4})$
$x_1^* = 0.1$	W1	Wake only	0
	RT1	RT only	6.82
	F1	Flap only	0
	RTF1	RT with flap IC	7.09
$x_2^* = 1.62$	W2	Wake only	0
	RT2	RT only	6.48
	F2	Flap only	0
	RTF2	RT with flap IC	6.26

4.4 Study of flapper generated effects

In this section, a set of experiments is designed (see Table 4.10) to study the effect of energy distribution with and without the flap, as well as with and without the unstable stratification. In a RT scenario, the baroclinic vorticity $\mathbf{\Omega_B} = (\nabla\rho\times\nabla\mathbf{p})/\rho^{\mathbf{2}}$ drives the growth of bubbles and spikes of larger wavenumbers towards saturation. Thus, the wavelength, λ, of the IC should be sufficiently small to reach saturation within the height of the test section, while sufficiently large to be larger than the size of the wake of the splitter plate ($\lambda \approx 0.32$ cm) and the upstream wire meshes that cause grid turbulence ($\lambda \approx 2.54$ cm). Based on previous experiments, $\lambda = 4$ cm is selected.

4.4.1 Quantification of IC

From linear stability analysis of Chandrasekhar (1961), simulations of Ramaprabhu et al. (2013) and experiments of Wilkinson & Jacobs (2007), nonlinear growth rates are observed when the height of the bubble is comparable to λ, i.e. $A_i/\lambda_i = 1$. Therefore, in the current experiments, the initial amplitude to wavelength ratio, $A/\lambda = 0.1$ is selected. The IC or 'flap' as quantified by Eqn. 4.11 generates a single perturbation, that rises against gravity as a bubble. Flapper motion at the interface is prescribed by $y = Asin(\omega t)$, when the time, $t\epsilon$ $[0, t_p/2]$. Here, y is the crosswise displacement of the tip of the flapper with time, t, and $t_p = 0.85$ s is the time period, chosen such that the wave speed is equal to the free stream convective speed (Eqn. 4.12). On the other hand, the periodic cases correspond to the continual motion of the flapper at all times of observation.

$$y(t) = A\sin(2\pi t/t_p), \quad t\epsilon[0, t_p/2] \tag{4.11}$$

$$\lambda = U_{mean}t_p \tag{4.12}$$

4.4.2 Secondary phenomena

The following phenomena interact with the flapper motion and RTI in the current study: *a) Initial velocity gradient between streams*: Any velocity gradient between the top and bottom streams results in a degree of shearing in the flow, which affects mixing. Towards this, the mean velocity profiles in the top and bottom water streams are measured multiple times and compared with each other. They show a velocity difference of about ±7% between them, which will affect the mixing layer minimally for low flow velocities. *b) Wake flow*: The splitter plate is very thin, however, its wake is caused due to upstream components in the developing section. *c) Boundary conditions*: While the bottom end of the Channel is bounded by Plexiglas, the top is open to the atmosphere, in order to minimize reflection of the laser plane during imaging. The thickness of the boundary layer formed at bottom of the wall of the Channel is estimated to be very small (of the order of a centimeter) and therefore, its effect on the mixing layer is neglected. These secondary phenomena are carefully recorded, quantified and verified to be insignificant in previous works by Kuchibhatla & Ranjan (2013a,b). From the previous measurements, it is found that three-dimensionality takes over when $x/H \approx 1.0$, where the density profiles get skewed with y. It could be due to the presence of spanwise modes due to the constraining walls of the Water Channel, however, the region corresponding to $z/H \approx 0$ in all cases exhibits a symmetrically growing mixing layer about the initial interface location.

The convective RT experimental systems such as used in the current scenario and Akula et al. (2013) are affected by the presence of wake emanating from the splitter plate. Ideally, minimal interaction between the wake flow and the RT instability is desired. However, using a very thin splitter plate poses design challenges, while a thicker plate results in a wider wake. In a symmetric RT scenario, a symmetric wake about the plate is also desired. Therefore, velocity profiles at different streamwise locations are plotted and a highly symmetric wake is observed. As the wake flow develops into a turbulent flow, it exhibits a cascading fluctuating kinetic energy spectrum. From the PIV measurements, the amplitude of the power spectrum of the components of fluctuating kinetic energy ($k =< u'^2 + v'^2 > /2 = 1.5I_t^2$) in x and y directions is calculated. Plots of k show that the dominant energy containing wavelengths correspond to the splitter plate thickness and mesh spacing. Therefore, it is surmised that the ICs employed in this study are very large compared to the size of the splitter plate, and hence, for all further purposes, it is assumed that the effect of the wake is insignificant in the evolution of the instability.

4.4.3 Flow visualization

PIV measurement of these regions is taken using two Nd-YAG lasers that pulse alternatively at 15 Hz each and a time delay of 0.01 s. This time delay is small enough to capture the particle motion in the turbulent regime. Using silver coated hollow glass spheres of 10 μm size, images of the flow fields are ensemble averaged to get the average velocity field in the center XY plane. For PIV, a bandpass filter of 532 nm±7 nm is used to capture the scattered light only. For PLIF measurement, very small concentrations (0.1 mgl^{-1}) of Rhodamine 6G are used with a high camera aperture to take flow images at 15 Hz. Such low concentrations are required for using normalized fluorescence images as equivalent to the normalized density fields. This is due to the nonlinearity in light attenuation at higher concentrations. It also reduces interference between the PIV and PLIF images. A notch filter that rejects incident laser illumination of 533 nm±2 nm is used during PLIF imaging so that only the fluoresced illumination is captured in images. For all cases, background images, dye and spatial calibration images are taken and used for subtracting noise from images and for ensuring both PLIF and PIV cameras record the same region in space.

For the 520 PLIF images, white noise caused ±0.4% uncertainty. Background images are acquired for all cases and subtracted for removing artifices of the imaging system e.g. non-uniformities in the laser plane due to optical alignment issues. As the Schmidt number of Rhodamine dye in water, Sc of the dye is large, a thorough mixing of the dye with water is achieved in order to avoid lumps of dye that would trail the water surrounding them. Due to limited system capabilities, about 520 PLIF images and 1040 PIV images (hence, 520 PIV vectors) could only be recorded, limiting the total time of observation to ≈ 34 s. The shortest streamwise locations recorded during imaging, x_1 and x_2 correspond to 2 cm and 63.5 cm, respectively. The list of cases for this study is given in Table 4.10.

Shown in Fig. 4.34 are images of the bubble and spike structures at non-dimensional early-time, t_1^* and late-time, t_2^* for all cases. All of these images are obtained at the same time after the start of the experiment, $t = 0.66$ s and represent typical flow fields; however, cases F1, F2, RTF1 and RTF2 are transient in nature compared to the rest of the cases. The wake flow (Fig. 4.34(a)) shows a periodic,

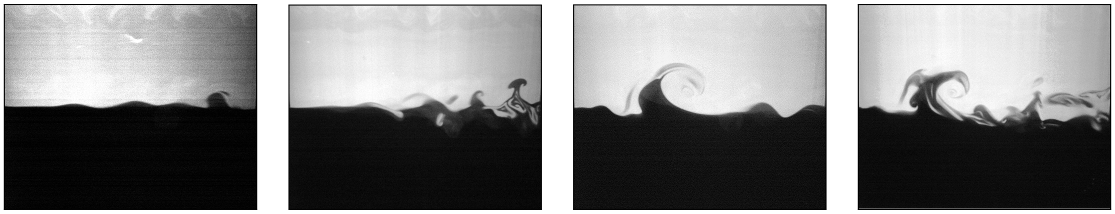

(a) Case W1 (b) Case RT1 (c) Case F1 (d) Case RTF1

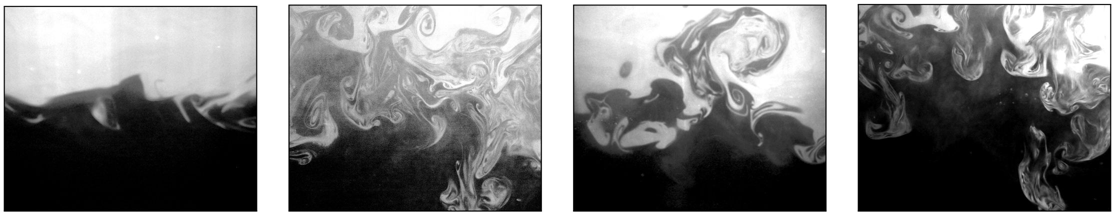

(e) Case W2 (f) Case RT2 (g) Case F2 (h) Case RTF2

Figure 4.34: Flow visualization for all cases at location x_1 (top row) and x_2 (bottom row).

wavy interface that is characteristic of von Karman vortices, with a small amount of mixing of the top and bottom streams. On the other hand, the RT flow (Fig. 4.34(b)) shows greater mixing due to the development of the initial perturbations inherently present in the streams into larger structures. A single bubble, which is a pocket of hot water escaping into the cold water above, is observed. When the flap is introduced into the flow (Fig. 4.34(c)), a large vortex is generated. The size of this vortex is significantly larger than the wake of the splitter plate. However, in the presence of RTI (Fig. 4.34(d)), several smaller secondary structures are observed on the vortex, which result in greater amount of mixing and a quicker evolution to turbulence. The presence of a wider range of scales is visualized in the enhanced turbulence intensity of the flow field at late-time. Here, Fig. 4.34(e) shows a slightly larger wake at late-time, while the RT case (Fig. 4.34(f)) shows a turbulent mixing layer. As compared to F2, case RTF2 shows enhanced mixing and the development of a large range of scales.

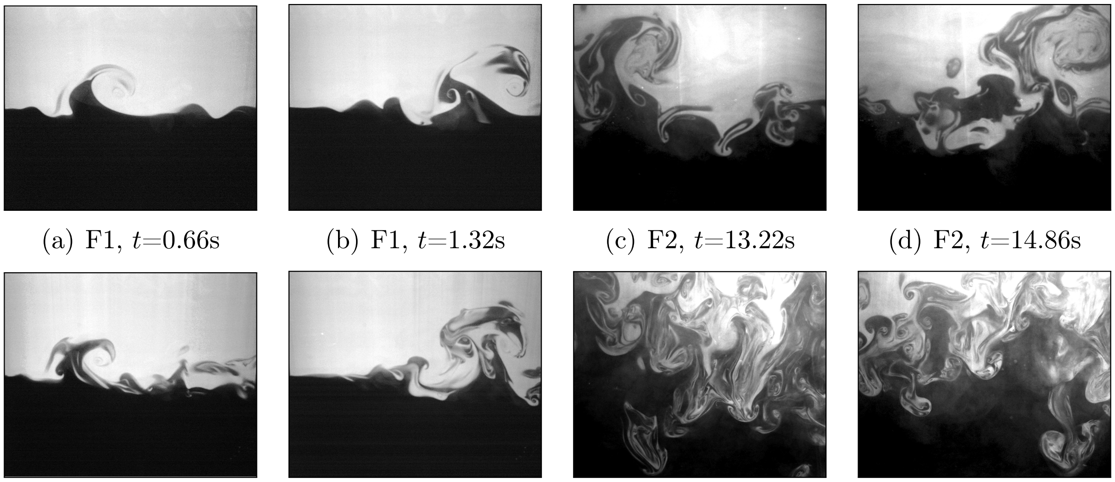

(a) F1, t=0.66s (b) F1, t=1.32s (c) F2, t=13.22s (d) F2, t=14.86s

(e) RTF1, t=0.66s (f) RTF1, t=1.32s (g) RTF2, t=13.22s (h) RTF2, t=14.92s

Figure 4.35: Images of flow with and without flapper motion and buoyancy. Casewise evolution of flap cases, F1 & F2 without density gradient (top row) and RTF1 & RTF2 with density gradient (bottom row).

A montage of the flow images with time for the flap cases F1, F2, RTF1 and RTF2 is given in Fig. 4.35. At time t = 1.32 s, case F1 shows a flap interacting with the wake flow. Case RTF1, on the other hand, shows a bubble aligned with the direction of acceleration due to gravity. The bubble is larger in the presence of RT, with a greater number of secondary structures emanating from it. For RTF2 at late-time, the bubble maybe larger than the imaging region.

4.4.4 Effect of buoyancy on vortex evolution

A vortex pair is induced by the flapper motion. As the pair progresses downstream, the velocity components along the centerline x can be used to identify the motion of the bubble tip with time. The peak of bubble velocity components, u and v, are denoted by u_{peak} and v_{peak} respectively. u_{peak} reaches a maximum and decreases with downstream distance (see Fig. 4.36). On the other hand, v_{peak} decays with downstream distance, but slower than u_{peak}. Similarly, in the presence of RTI,

v_{peak} reaches a maximum value after a longer duration. This peak magnitude corresponds to the saturation bubble velocity under the presence of buoyancy, variation of velocity components of which is given in Fig. 4.37.

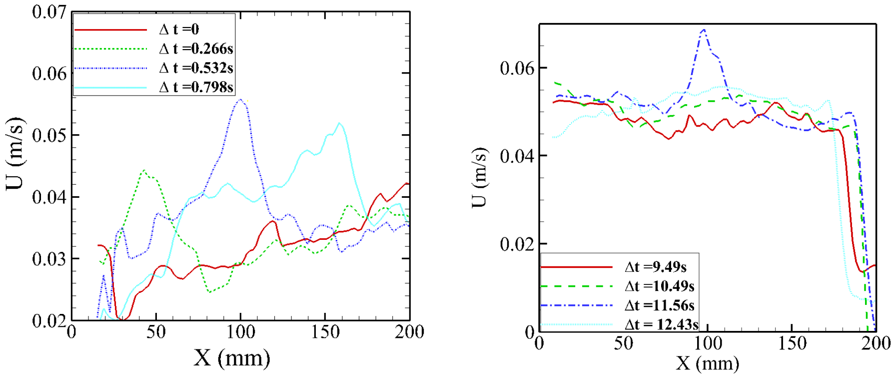

(a) u at x_1 (b) u at x_2

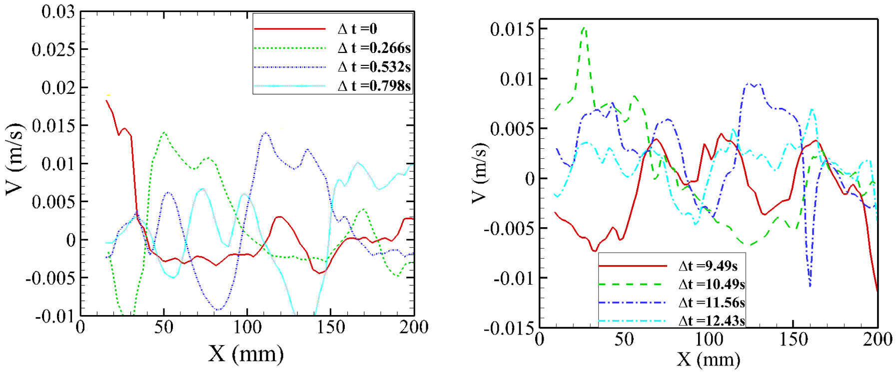

(c) v at x_1 (d) v at x_2

Figure 4.36: Evolution of velocity components along centerline x for flap case without RTI. Top row indicates the profile of u, while bottom row is for v.

A better idea of the interaction of the vortex pair and baroclinic vorticity can be obtained from contour plots of vorticity in the Z-direction, $\Omega_z(x, y, t) = \frac{\delta v}{\delta x} - \frac{\delta u}{\delta y}$. The plots correspond to locations x_1 and x_2 respectively (Fig. 4.38). For the flap cases, instantaneous contours of vorticity are plotted (these correspond to the images in Fig. 4.34), while for the other cases, Reynolds averaged (or equivalently, time averaged) vorticity is plotted. The case W1 (Fig. 4.38(a)) shows layers of

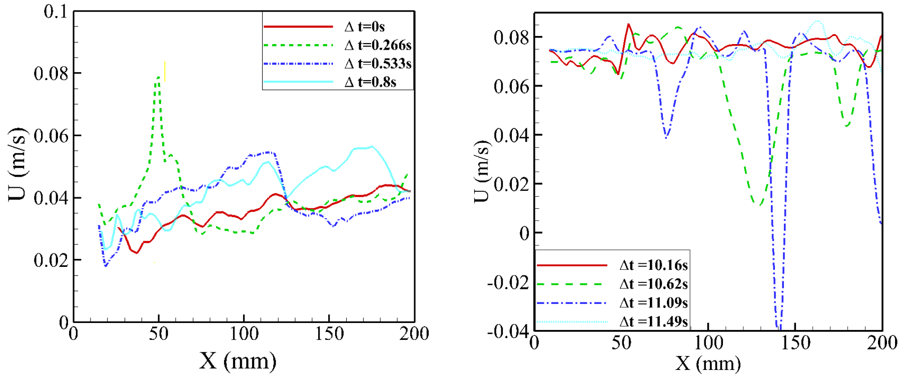

(a) u at x_1 (b) u at x_2

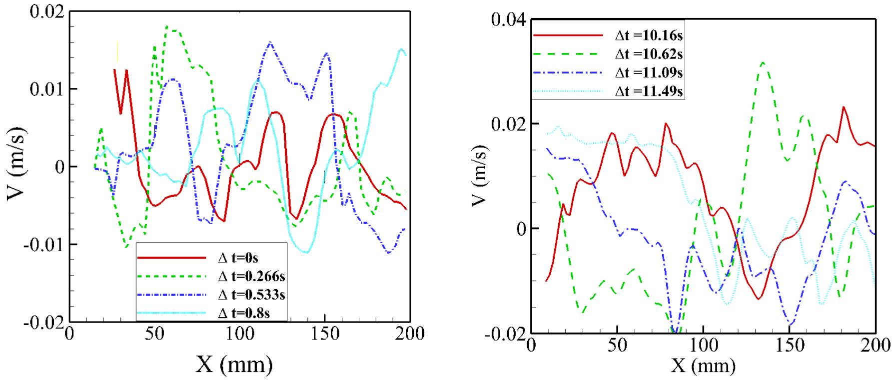

(c) v at x_1 (d) v at x_2

Figure 4.37: Evolution of velocity components along centerline x for flap under RTI. Top row indicates the profile of u, while bottom row is for v.

negative vorticity above a layer of positive vorticity caused to the velocity deficit in the wake of the splitter plate. A similar scenario is seen in the RTF1 case (Fig. 4.38(c). In Fig. 4.38(e) it can be observed that a vortex pair is generated due to the flap. The strength of the vortex pair is greater when present in a RT setting (Fig. 4.38(g)). It can be also inferred that the baroclinic vorticity at the interface is greater than the vorticity induced by the flap. An initial condition that generates a large amount of vorticity in comparison with baroclinic vorticity is not preferred for Rayleigh-Taylor experiments, as it would dwarf the development due to RTI. In the previous experimental studies by Kuchibhatla & Ranjan (2013a), periodic multi-modal oscillations of the flapper are used for studying the effect of initial conditions on Rayleigh-Taylor growth. The current exercise proves that the initial vorticity due to flapper motion is not so strong as to render RT growth insignificant. However, an accurate comparison of flap vorticity vs. baroclinic vorticity can only be performed when the initial conditions used in Kuchibhatla & Ranjan (2013a) are replicated, which is not the case. The largest wavelength used in Kuchibhatla & Ranjan (2013a) is 8 cm, and the temperature gradient (or Atwood number) is greater than the current case.

The above discussion pertains to the qualitative comparison of velocity profiles and vorticity fields, because of the transient nature of the flap cases. For the wake flow and RT flow, however, turbulent statistics can be obtained by Reynolds averaging (indicated by <>) as described below. The wake case W1 shows the greatest turbulence intensity (or equivalently, RMS turbulence velocity $U_{rms} = \sqrt{(u'^2 + v'^2)/2}$) at the interface right off the splitter plate. Case RT1 exhibits the greatest RMS turbulence velocity magnitude along the mixing layer, which grows with streamwise distance. Thus, it may be that buoyancy accentuates density and velocity gradients in the flow field that produce a greater amount of turbulence intensity. Also, the

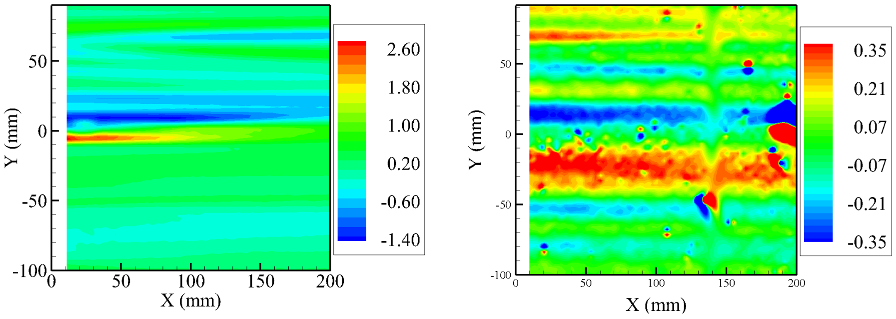

(a) Wake at x_1

(b) Wake at x_2

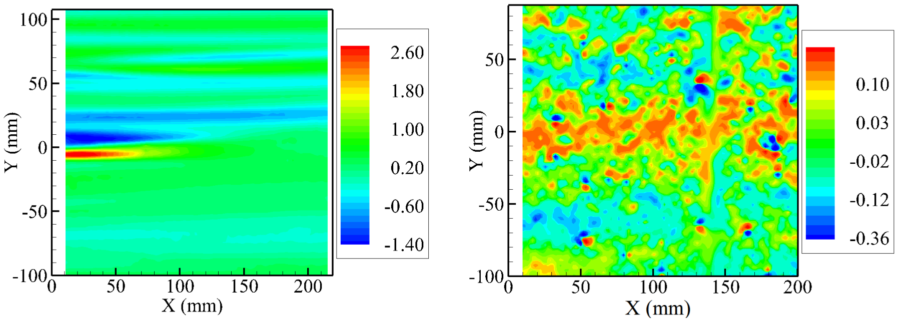

(c) RT at x_1

(d) RT at x_2

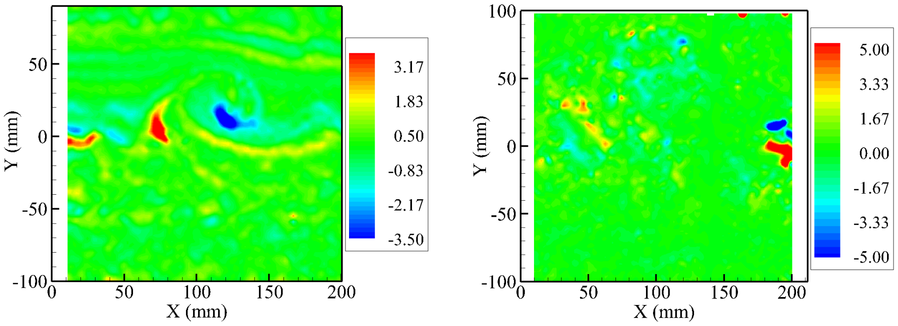

(e) Flap only at x_1

(f) Flap only at x_2

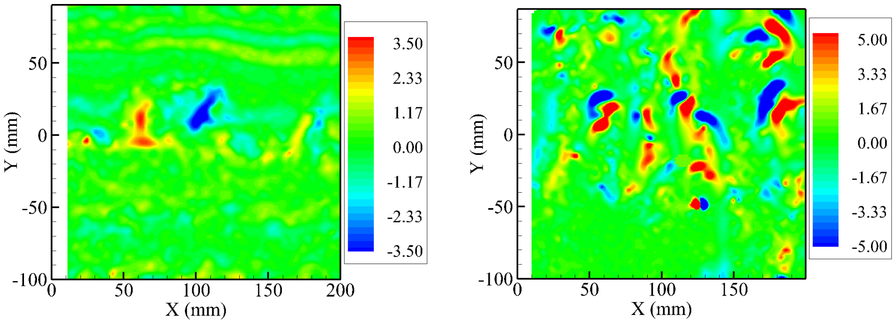

(g) Flap under RT at x_1

(h) Flap under RT at x_2

Figure 4.38: Contours of vorticity Ω_z (s^{-1}) for flow in Figures 4.34 and 4.35. The left column corresponds to location x_1, while right column corresponds to x_2.

effect of the flap cannot be completely understood using the current time averaging technique and a detailed study of the mixing due to flap needs to be performed.

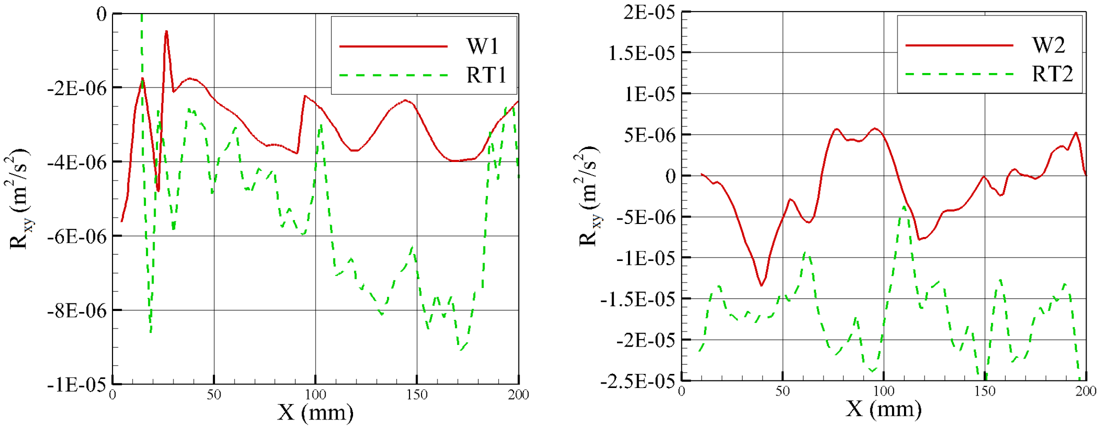

(a) R_{xy} variation along horizontal centerline at x_1 (b) R_{xy} variation along horizontal centerline at x_2

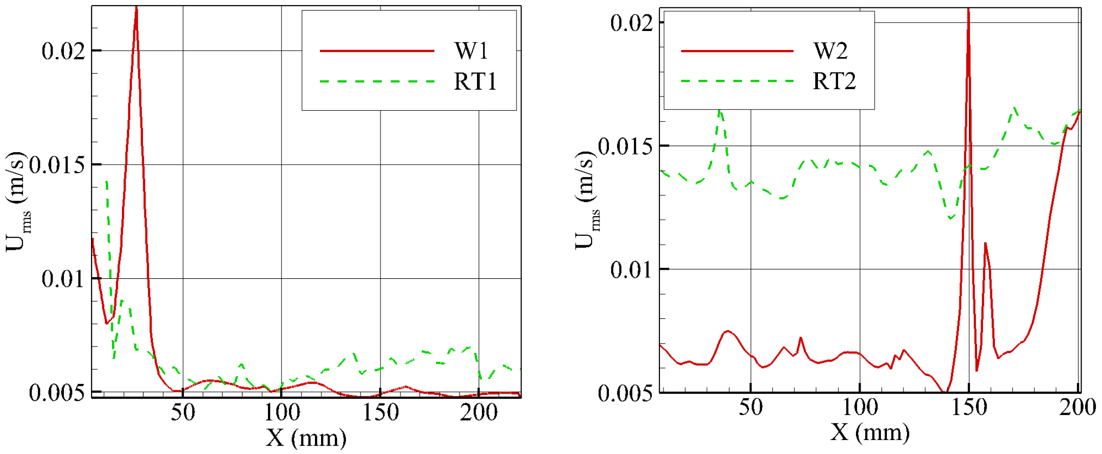

(c) U_{rms} variation along horizontal centerline at x_1 (d) U_{rms} variation along horizontal centerline at x_2

Figure 4.39: Comparison of turbulence statistics at different streamwise locations using Reynolds averaging. The top row is a comparison of Reynold stress component R_{xy}, while the bottom row is for RMS turbulence velocity, U_{rms}.

In order to understand the nature of interaction of RT flow with the initial condition, plots of Reynolds stress component in the XY plane, $R_{xy} = R_{yx} =< u'v' >$ along the X-axis, i,e. $y = 0$, are given in Fig. 4.39. The quicker mixing in RT case is witnessed in the stronger magnitude of R_{xy} at either locations. Plots of the Reynolds stress along the streamwise direction at the horizontal centerline show that the Reynolds stress component, R_{xy} is stronger in the presence of buoyancy than without it. The above behavior can also be corroborated by RMS turbulence velocity profiles given in Fig. 4.39.

Previously, Kellogg & Corrsin (1980) studied the grid turbulence phenomenon of flow past a 'zither', and observed periodicity in the autocorrelation parameter and the power spectra at large wavenumbers corresponding to the dimensions of the zither. In their experiments, the zither is a set of parallel cylinders that generate periodic structures downstream. The periodicity of such a flow can be studied by observing the autocorrelation of density or velocity at a certain downstream location using diagnostics with high temporal resolution. The frequency of the diagnostic technique must be greater than twice the frequency of the structures shed from the zither. The decay of kinetic energy due to this periodic boundary condition is recorded and compared with analytical models of Comte & Corrsin (1971). This type of analysis will provide a better idea of the interaction for periodic RT flows.

4.4.5 Observations on effect of flapper motion

Significant points of observation include: *a*) A set of experiments with and without flap and RTI are performed to study the evolution of a flap in an unstably stratified mixing layer. *b*) Instantaneous flow images are obtained using PLIF, while two-dimensional velocity vectors are simultaneously obtained using PIV simultaneously. *c*) Flow images show that RTI is responsible for a greater amount of mixing and turbulence levels than the wake flow. *d*) When a flap is induced into a RT flow field, it introduces a pair of counter rotating vortices, which result in a quicker growth of the mixing region than without buoyancy force. Also, because of the nonlinear interaction of flap with the structural modes inherent to the Water Channel, a larger range of scales is witnessed in case of RT flow with flap. The flap vorticity is comparable to the magnitude of baroclinic vorticity for the temperature gradient used in the current study. *e*) The RT mixing layer produces strong turbulence levels in it along the center of the mixing layer. *f*) The current analysis provided a quantitative basis to the interaction of energy distribution in terms of mean profiles and time variation of velocity components, however, qualitative support to this discussion is required by plotting energy spectra and cumulative distributions. *g*) A comparison of the energetics with and without flap would provide insight into the distribution of kinetic energy between scales and its dissipation. *h*) Future endeavors using periodic initial conditions need to be performed to understand the presence of artifacts of initial configuration upon turbulent flows.

4.5 PLIF imaging results

In this section, PLIF images of the entire test section are presented for different types of ICs(see Table 4.11). Experimental cases are organized by increasing number of modes. The last broadband case uses 11 modes, the distribution of which is similar to the broadband IC used in Olson & Jacobs (2009). Here, the first 11 modes of the IC are taken, such that they replicate the waveform within reasonable error, while capturing the largest amplitudes, as shown in Fig. 4.40(a). However, the wavelengths used in Olson & Jacobs (2009) are much smaller than the current experiment. Therefore, a scaling factor is used such that the largest wavelength is $\lambda_{max} = 4$ cm, so that the remaining modes lie in the lower neighborhood, i.e. 2.04 cm $\leq \lambda \leq$ 4 cm. This neighborhood also contains the most unstable wavelength of the Water Channel, thus, the interaction will include all the major factors of the experiment. Plot of the variation of phase angle with wavelength for the component modes of case 18 is given in Fig. 4.41.

Table 4.11: List of parameters for PLIF visualization experiments.

IC type	Remarks	Case #	λ_1 (cm)	λ_2 (cm)	λ_3 (cm)	β_1 (°)	β_2 (°)	A_t ($\times 10^{-3}$) at x_1	A_t ($\times 10^{-3}$) at x_2
Single-mode	Increasing λ	1	0	-	-	-	-	1.88	1.90
		2	2	-	-	-	-	1.72	1.85
		3	4	-	-	-	-	1.42	1.65
		4	6	-	-	-	-	1.42	1.65
		5	8	-	-	-	-	1.61	1.73
Binary-mode	Increasing β	6	8	2	-	0	-	1.92	2.15
		7	8	2	-	30	-	1.88	2.15
		8	8	2	-	45	-	1.88	2.15
		9	8	2	-	60	-	1.88	2.15
		10	8	2	-	90	-	1.88	2.15
		11	8	2	-	120	-	1.88	2.15
	Increasing λ_2	12	8	4	-	45	-	1.88	2.15
		13	8	6	-	45	-	1.88	2.15
Multi-mode	Inc. # of modes	14	8	4	2	45	90	2.85	2.14
		14	8	4	2	45	90	2.00	1.97
		15	8	6	4	45	-	2.00	1.97
		16	8	6	5	45	-	2.00	1.97
		17	8	7	6	45	-	2.00	1.97
		18	Broadband IC					2.00	1.97

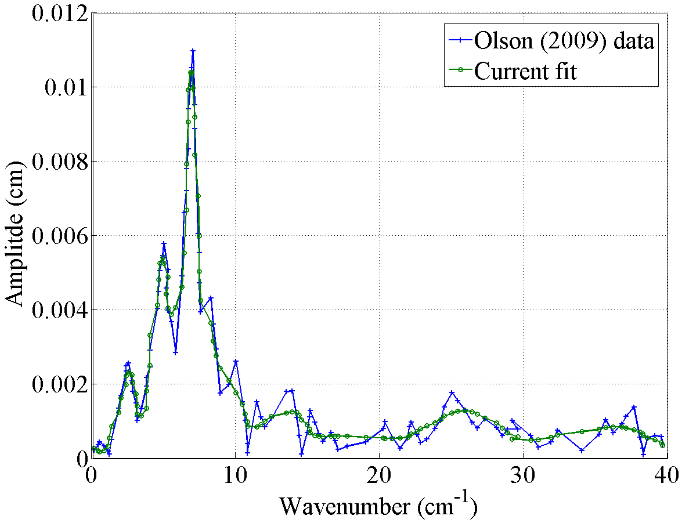

(a) Interface amplitude, A, vs. wavenumber, k

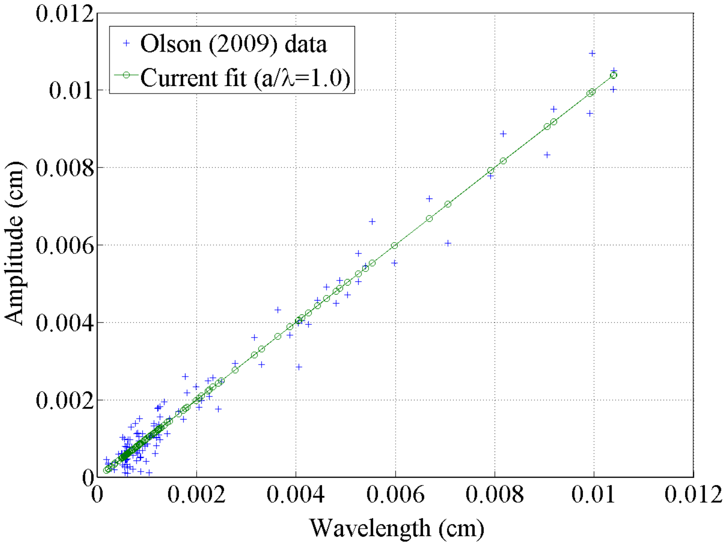

(b) Ratio of $A/\lambda \sim 1$ for Olson & Jacobs (2009)

Figure 4.40: Broadband IC case 18: Current waveform vs. Olson & Jacobs (2009).

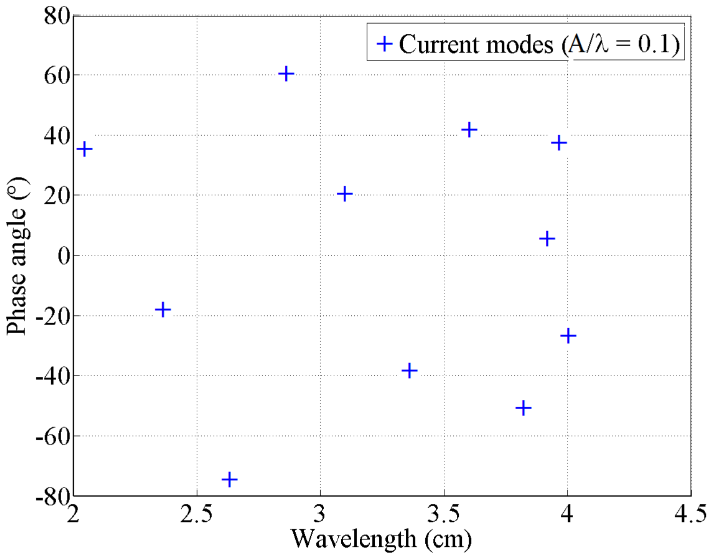

Figure 4.41: Composition of broadband IC case 18: β vs. λ.

4.5.1 Visualization of entire test section

Shown in Figures 4.42, 4.43, 4.44 and 4.45 are plots of the bubble and spike structures right off the splitter plate, for a different types of IC.

Mixing width its obtained from the ensemble averaging of about 2200 of these images, and statistical convergence is obtained. Figure 4.46 shows the contour plots at different stages of this processing technique, while Fig. 4.47 shows the RMS uncertainty from the location of pure fluid at all times in the images. The uncertainty reaches a constant value of about $\sim 0.4\%$ for all cases. By subtracting the average background image from the average intensity image in the illumination plane, contours of mixing fraction are obtained. A discussion of the dye calibration setting and optimum aperture setting are listed in appendix E.

Use of PLIF technique for density measurement is widely reported in literature (see Dahm & Dimotakis (1987), Reid et al. (2013) and Webster et al. (2001)). Rhodamine 6G is used in water as tracer. It has a Schmidt number, $Sc = \nu/D \approx 1500$, Prandtl number, $Pr = \nu/\alpha \approx 7$, and Lewis number, $Le = Sc/Pr = \alpha/D \approx 214$. This means that thermal diffusion is much faster than mass diffusion, and the particles lag the mixing layer. Therefore, the molecular mixing parameter, which is sensitive to RMS of intensity fluctuations in the image, is overpredicted. Also, the low temporal frequency of this imaging technique cannot capture the rapid fluctuations witnessed in turbulent flows. As such, molecular mixing of large-scale strucutures is only captured using this technique. To ensure this, the shape of the intensity histogram from PLIF is compared with thermocouple data in Fig. 4.48 for case 3. In these plots, it should be noted that while the thermocouples sample at 1 kHz for 60 seconds, the PLIF method samples at 15 Hz for 150 s. Also, while the Atwood number of both cases might be slightly different, they retain the general shape of the

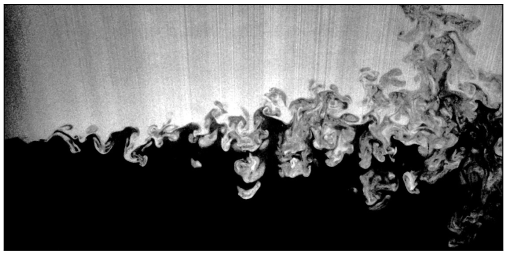

(a) $\lambda = 0$ cm

(b) $\lambda = 2$ cm

(c) $\lambda = 4$ cm

(d) $\lambda = 6$ cm

(e) $\lambda = 8$ cm

Figure 4.42: Flow visualization of single-mode cases.

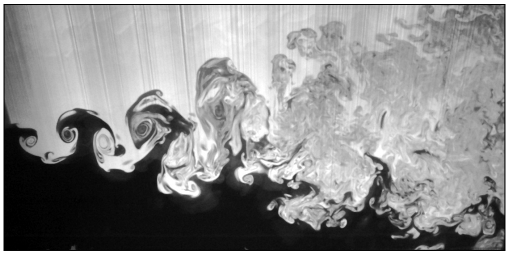

(a) $(\lambda_1, \lambda_2, \beta)$ = (8 cm, 2 cm, 0°)

(b) $(\lambda_1, \lambda_2, \beta)$ = (8 cm, 2 cm, 30°)

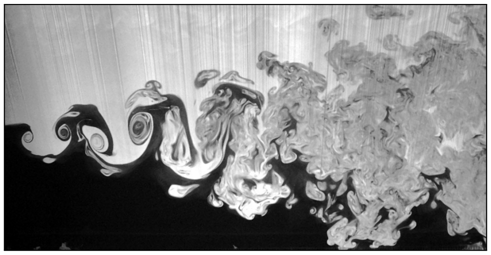

(c) $(\lambda_1, \lambda_2, \beta)$ = (8 cm, 2 cm, 45°)

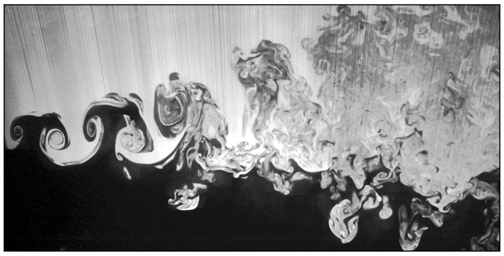

(d) $(\lambda_1, \lambda_2, \beta)$ = (8 cm, 2 cm, 60°)

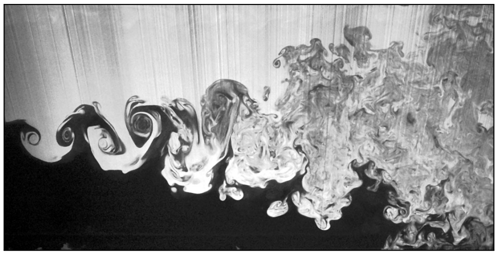

(e) $(\lambda_1, \lambda_2, \beta)$ = (8 cm, 2 cm, 90°)

Figure 4.43: Flow visualization of cases with increasing phase angle.

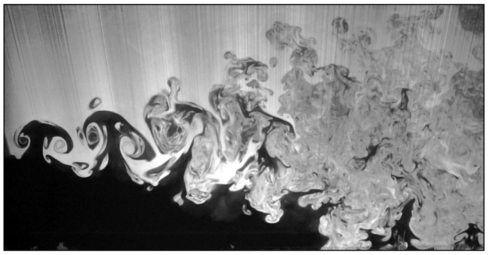

(a) 3 modes

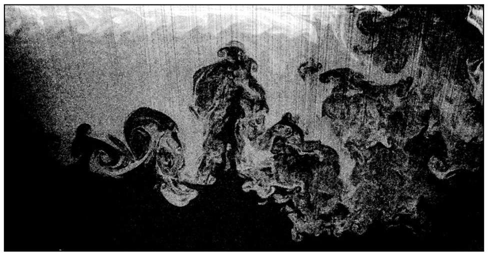

(b) 4 modes

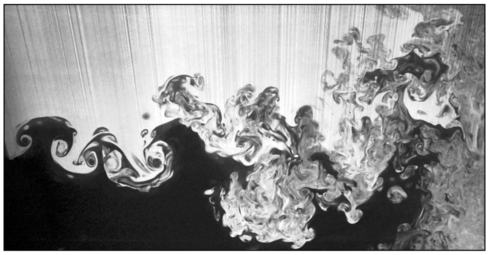

(c) 5 modes

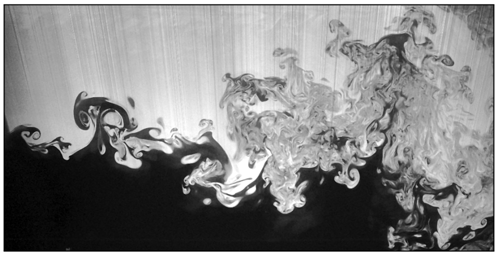

(d) 7 modes

(e) Broadband IC

Figure 4.44: Flow visualization of cases with increasing number of modes.

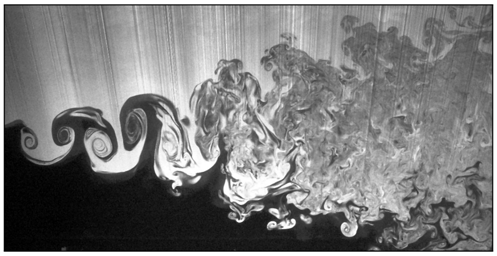

(a) $(\lambda_1, \lambda_2, \beta)$ = (8 cm, 2 cm, 120°)

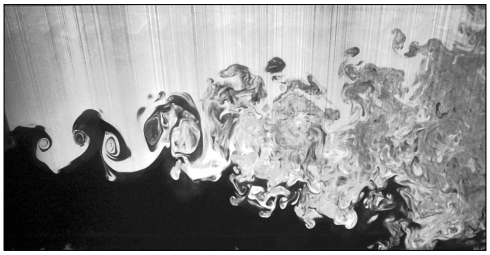

(b) $(\lambda_1, \lambda_2, \beta)$ = (8 cm, 4 cm, 45°)

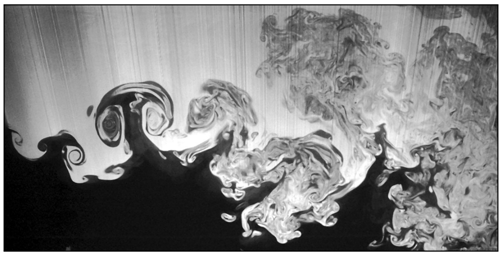

(c) $(\lambda_1, \lambda_2, \beta)$ = (8 cm, 6 cm, 45°)

Figure 4.45: Flow visualization of remaining cases.

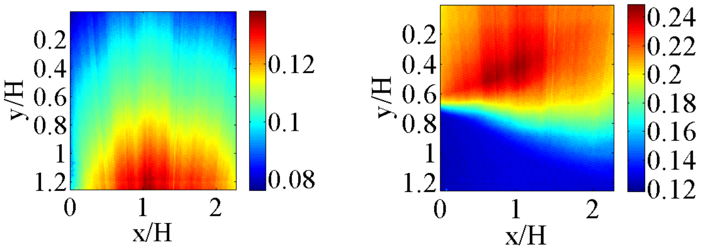

(a) Average background image (b) Average mixing image

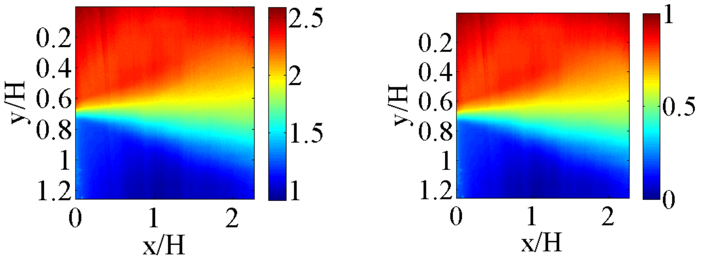

(c) Divided image (d) Scaled image

Figure 4.46: Contour plots of average image at different stages of ensemble averaging.

Figure 4.47: Variation of RMS white noise with number of images.

distribution. The PLIF images have a resolution of about 50 pixels per cm at x_1 and 66 pixels per cm at x_2, respectively.

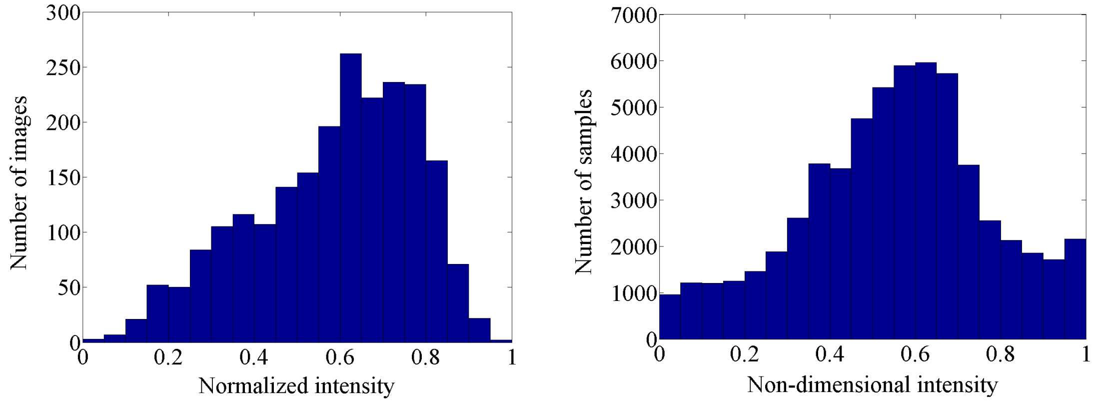

(a) Intensity using PLIF

(b) Intensity using thermocouples

Figure 4.48: Histograms of normalized intensity using PLIF and thermocouples at $(x, y, z) = (x_1, 0, 0)$ cm for case 3.

4.5.2 Visualization of turbulent zones

PLIF images of the center-plane of the Channel for all cases at a streamwise location of $x_{im,1} = 1$ in and $x_{im,2} = 40$ in are given in Figures 4.49, 4.50, 4.51 and 4.52 respectively.

For the single-mode cases 1, 2 and 8 (shown in Figures 4.49(a)-4.50(g)), the wavelength of the wave is increased and therefore, larger sized mushroom structures are observed as the flow develops with time. Characteristic bubble and spike structures can be visualized in these images. The initially horizontal interface grows into larger bubbles and spikes, which show a multi-modal behavior in the downstream region. An area of about 11 cm×11 cm is photographed and shown in all images of 4.49(a)-4.50(g), and show the instantaneous RTI structures within the linear and nonlinear regimes. As the instability develops, smaller secondary structures arise from the

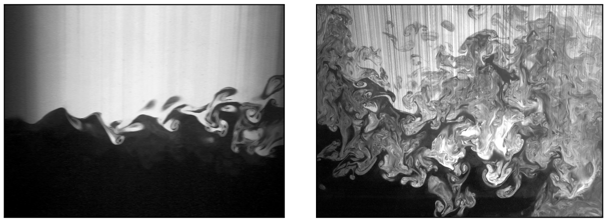

(a) $\lambda = 0$ cm at x_1 (b) $\lambda = 0$ cm at x_2

(c) $\lambda = 2$ cm at x_1 (d) $\lambda = 2$ cm at x_2

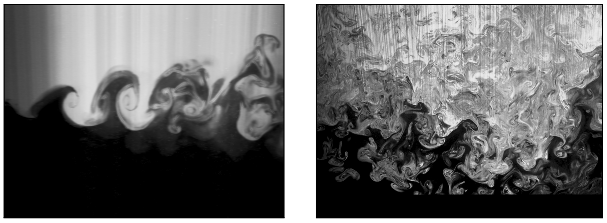

(e) $\lambda = 4$ cm at x_1 (f) $\lambda = 4$ cm at x_2

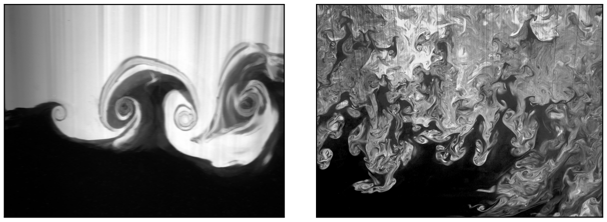

(g) $\lambda = 6$ cm at x_1 (h) $\lambda = 6$ cm at x_2

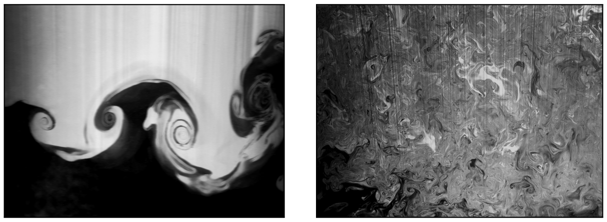

(i) $\lambda = 8$ cm at x_1 (j) $\lambda = 8$ cm at x_2

Figure 4.49: Flow visualization of single-mode cases at early and late-times.

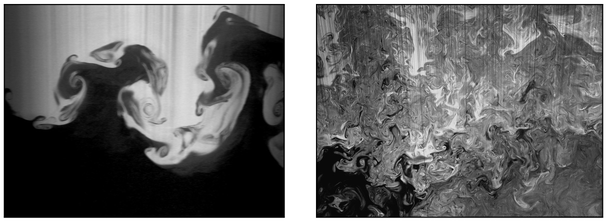

(a) $(\lambda_1, \lambda_2, \beta)$ = (8 cm, 2 cm, 0°) at x_1 (b) $(\lambda_1, \lambda_2, \beta)$ = (8 cm, 2 cm, 0°) at x_2

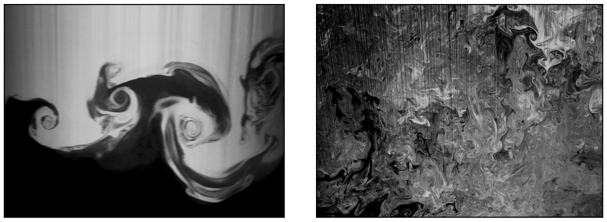

(c) $(\lambda_1, \lambda_2, \beta)$ = (8 cm, 2 cm, 30°) at x_1 (d) $(\lambda_1, \lambda_2, \beta)$ = (8 cm, 2 cm, 30°) at x_2

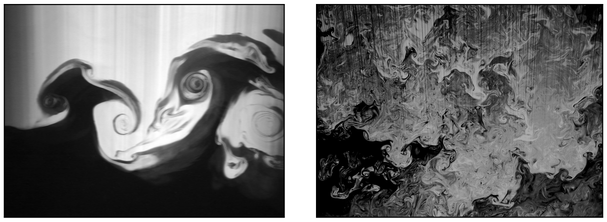

(e) $(\lambda_1, \lambda_2, \beta)$ = (8 cm, 2 cm, 45°) at x_1 (f) $(\lambda_1, \lambda_2, \beta)$ = (8 cm, 2 cm, 45°) at x_2

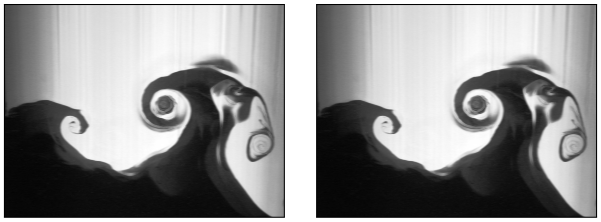

(g) $(\lambda_1, \lambda_2, \beta)$ = (8 cm, 2 cm, 60°) at x_1 (h) $(\lambda_1, \lambda_2, \beta)$ = (8 cm, 2 cm, 60°) at x_2

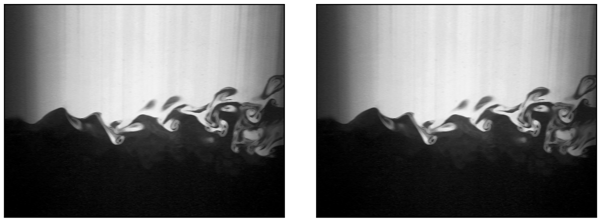

(i) $(\lambda_1, \lambda_2, \beta)$ = (8 cm, 2 cm, 90°) at x_1 (j) $(\lambda_1, \lambda_2, \beta)$ = (8 cm, 2 cm, 90°) at x_2

Figure 4.50: Flow visualization of cases with increasing phase angle at early and late-times.

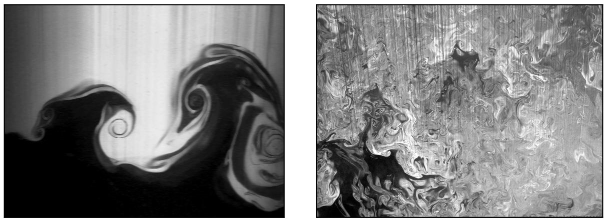

(a) 3 modes at x_1 (b) 3 modes at x_2

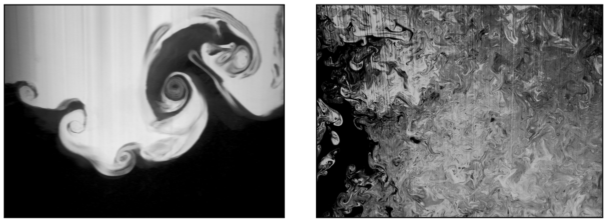

(c) 4 modes at x_1 (d) 4 modes at x_2

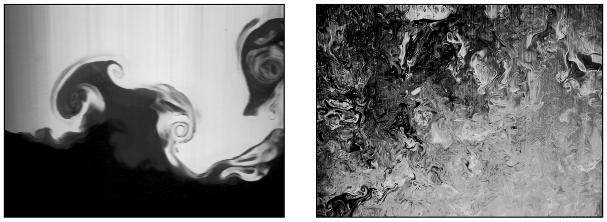

(e) 5 modes at x_1 (f) 5 modes at x_2

(g) 7 modes at x_1 (h) 7 modes at x_2

Figure 4.51: Flow visualization of cases with increasing number of modes at early and late-times.

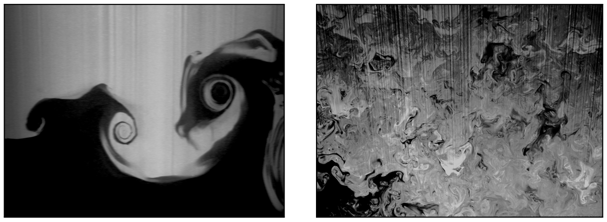

(a) $(\lambda_1, \lambda_2, \beta)$ = (8 cm, 2 cm, 120°) at x_1

(b) $(\lambda_1, \lambda_2, \beta)$ = (8 cm, 2 cm, 120°) at x_2

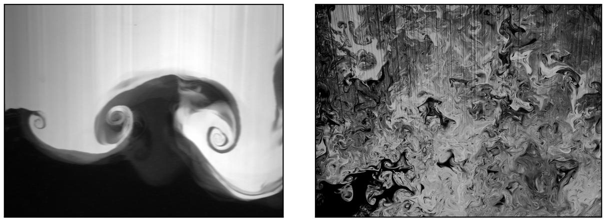

(c) $(\lambda_1, \lambda_2, \beta)$ = (8 cm, 4 cm, 45°) at x_1

(d) $(\lambda_1, \lambda_2, \beta)$ = (8 cm, 4 cm, 45°) at x_2

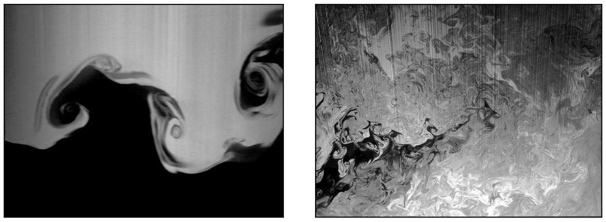

(e) $(\lambda_1, \lambda_2, \beta)$ = (8 cm, 6 cm, 45°) at x_1

(f) $(\lambda_1, \lambda_2, \beta)$ = (8 cm, 6 cm, 45°) at x_2

Figure 4.52: Flow visualization of cases 11-13 at early and late-times.

primary bubbles and spikes, because of the development of Kelvin-Helmholtz shear mechanism after initial stages, affecting RTI growth. Image of multi-modal flow structures with three initial modes is provided in Fig. 4.50(g) (case 9). It can be observed that the smaller spikes and bubbles are 'leaning' away from the vertical axis when there exists a phase difference between the modes. From these sets of images, parameters B_0, B_2 and θ can be extracted for analysis. PLIF data can be used to extract scalar dissipation rate, which is used for quantifying fine-scale mixing. Thus, the effect of ICs in inducing fine-scale mixing can be observed. Flow visualization for increasing number of modes is given in Fig. 4.51, while rest of the cases are visualized in Fig. 4.52.

4.6 Analysis of full Channel PLIF data

An analysis of a few select cases among the above is presented in this subsection. The effect of increasing number of modes is studied using the list of cases in Table 4.12.

Table 4.12: List of PLIF experiments with increasing number of modes.

# modes	λ_1 (cm)	λ_2 (cm)	λ_3 (cm)	λ_4 (cm)	$\beta_i - \beta_{i-1}$ (°)	A_t ($\times 10^{-3}$)
0	0	-	-	-	-	1.00
1	8	-	-	-	-	1.07
3	8	4	2	-	45	1.07
7	(8,7,6,5,4,3,2)				45	1.11
11	Broadband IC					1.13

Because a high divergence laser plane is utilized for imaging, a small region, i.e. x_0 ($\sim$ 0-8.89 cm) is cropped from all images to remove image edge artifacts. This offset in time, t_0, is accounted in all cases. For each case, a total of 800 images are taken to reduce statistical uncertainties to $\sim$ 0.4%. Background images are taken for all cases and subtracted for removing artifices of the imaging system such as non-uniformities in the laser plane due to optical alignment issues. Also, a calibration procedure that ensures a linear variation of pixel intensity with dye concentration is followed. From this procedure, the limiting amount of dye that is sufficient to produce maximum contrast in the images, while attenuating the laser linearly within the Channel is found to be 29 μgl^{-1}. This is in consistency with the experiments of Ferrier et al. (1993), who found the limiting dye concentration to be 50 μgl^{-1}. However, it should be noted that attenuation of the signal depends upon the incoming laser fluence, which is greater for the current experiments. Using a procedure similar to Weber

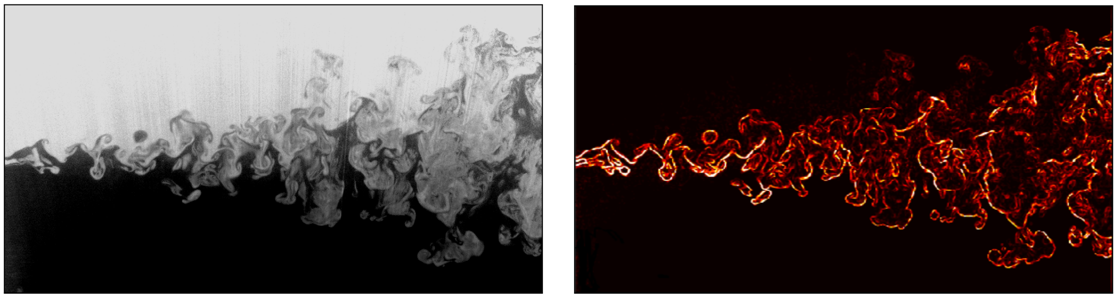

(a) $\lambda = 0$ cm (b) Contours of χ for $\lambda = 0$ cm

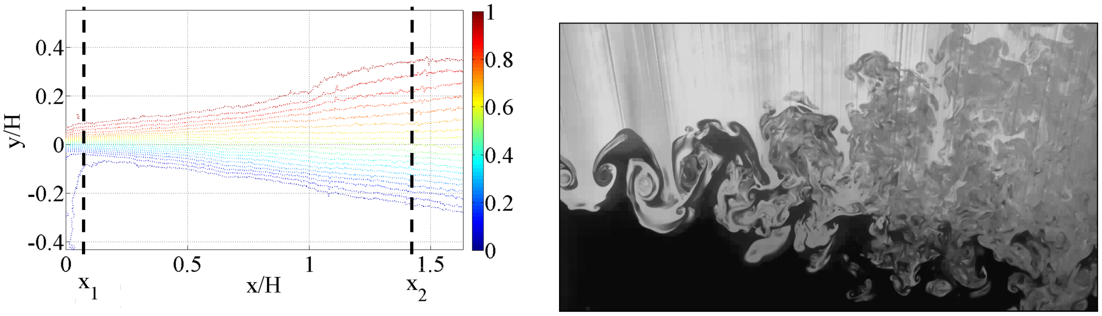

(c) Contours of f_c for $\lambda = 0$ cm (d) $\lambda = 8$ cm

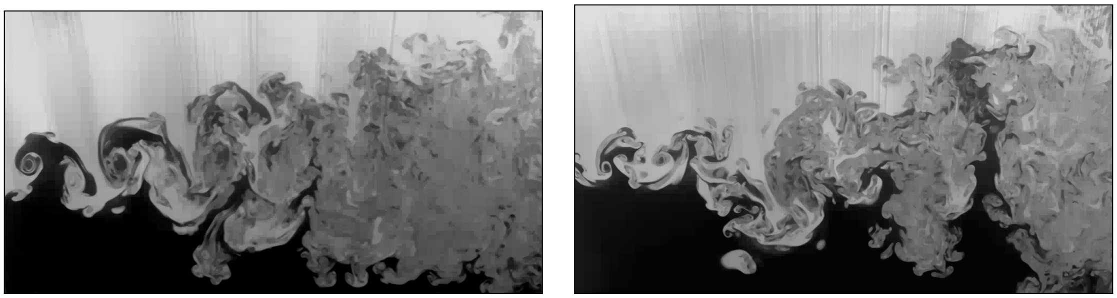

(e) $\lambda =$ (8, 4, 2) cm, $\delta\beta = 45°$ (f) $\lambda =$ (8, 7, 6, 5, 4, 3, 2) cm, $\delta\beta = 45°$

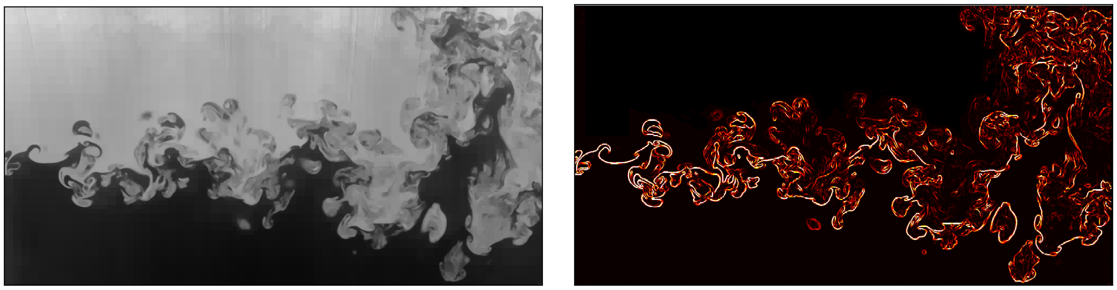

(g) Broadband IC (h) Contours of χ for broadband case

Figure 4.53: PLIF imaging of flow evolution for cases listed in Table 4.11. A region of $x \times y \approx 58.67$ cm$\times$38.48 cm is presented.

(2012), nonlinear illumination due to divergence of the laser plane is corrected. Using the 'Haar' 2D wavelet filter, vertical striations in the images caused due to the changing refractive index of the working fluid are removed. The initially horizontal fluid interface develops into larger flow structures that show merge to eventually become turbulent. Therefore, it is inferred that case 1 (Fig. 4.53(a)) comprises of few inherent modes due to the flow laminators and wire meshes present in the experimental setup. The qualitative contours of scalar dissipation rate are given in Fig. 4.53(b), with the brightest points corresponding to the greatest magnitude of gradient of the density. Figure 4.53(d) shows the single-mode bubbles and spikes for case 2. For multi-mode cases 3-5 (Figures 4.53(f)-4.53(g)), increasing the number of modes induces more secondary structures into the flow field, which soon results in secondary interactions due to mode coupling.

Table 4.13: Comparison of bubble vertical velocity with literature.

# modes	t_0/τ	λ_{eq} (cm)		Bubble velocity, U_b (cms^{-1})	
		Expt.	Max(λ_i)	$dh/2dt$	Goncharov (2002)
0	0.90	4.42	3.78	1.16	0.68
1	0.70	7.88	8.00	1.07	0.94
3	0.75	6.81	8.00	0.79	0.87
11	0.75	7.20	4.00	1.26	0.92

Total mixing width ($h = h_{f_h=0.95} - h_{f_h=0.05}$) for all cases are given in Fig. 4.54. The figure show that case 1 approaches the saturation growth rate (where h varies as $\alpha A_t g t^2$), while the remaining cases are yet to saturate. This is due to the large wavelength ICs that take longer times for saturation. However, case 1 which shows a parabolic mixing width at late-times exhibits bubble velocity significantly different from potential flow model by Goncharov (2002). Symmetric bubble and spike growth

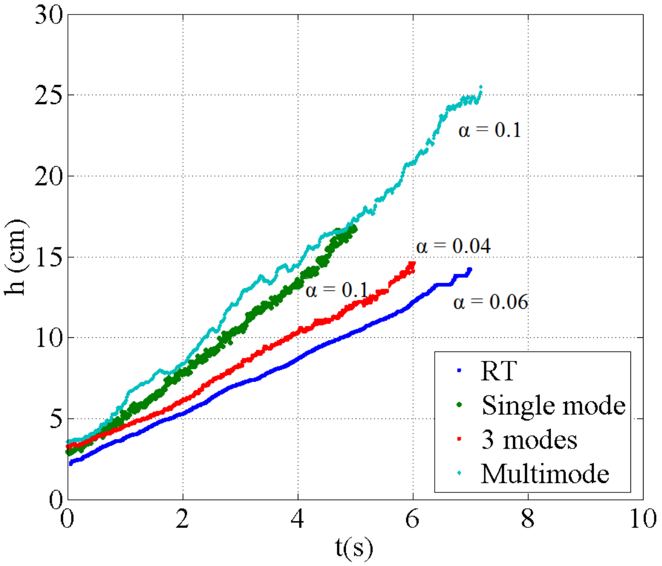

Figure 4.54: Mixing width variation.

is observed, which is characteristic of low density contrast RT flows. Therefore, bubble velocity is calculated by $U_b = \frac{dh}{2dt}$ and compared with Goncharov's estimate $U_b = \frac{\lambda_{eq}}{\sqrt{3\pi(1+A_t)\tau}}$. Here, τ is the equivalent wavelength of each case, given by $\tau = \sqrt{\frac{\lambda_{max}}{A_t g}}$ in Table 4.13.

In the nonlinear and saturation regimes, the center of the mixing layer is quickly and completely mixed ($f_h = 0$) and the molecular mixing parameter reaches asymptotic values. A plot of variation of θ for all cases is given in Fig. 4.55. Here, case 1 asymptotes to 0.75, while the rest of the cases show larger values. Recently, from their numerical simulation, Ramaprabhu et al. (2013) attributed higher θ in multi-modal RT mixing to greater amount of molecular mixing due to secondary instabilities. With delayed transition, a corresponding delay in saturation is witnessed, therefore, θ at the same t^* is smaller. Therefore, using λ_{eq} for the time-scale τ is more accurate estimate for periodic ICs, similar to Dimonte (2004); Mueschke (2008), who used the

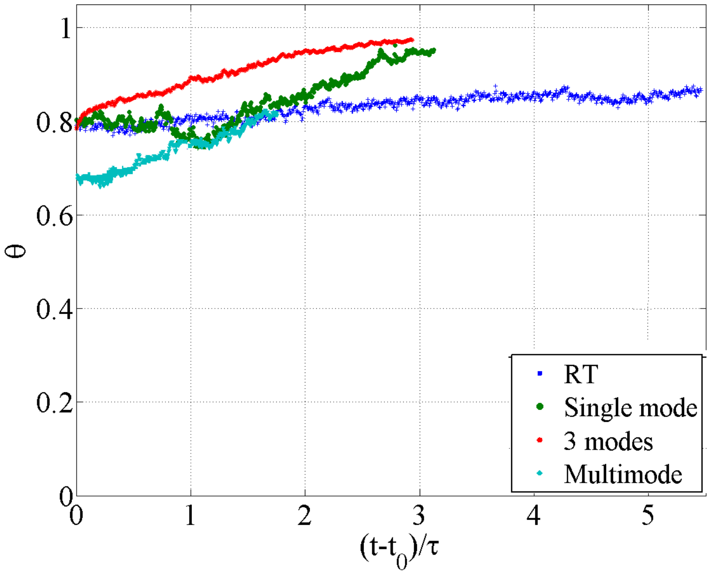

Figure 4.55: Molecular mixing variation.

largest component wavelength of the system.

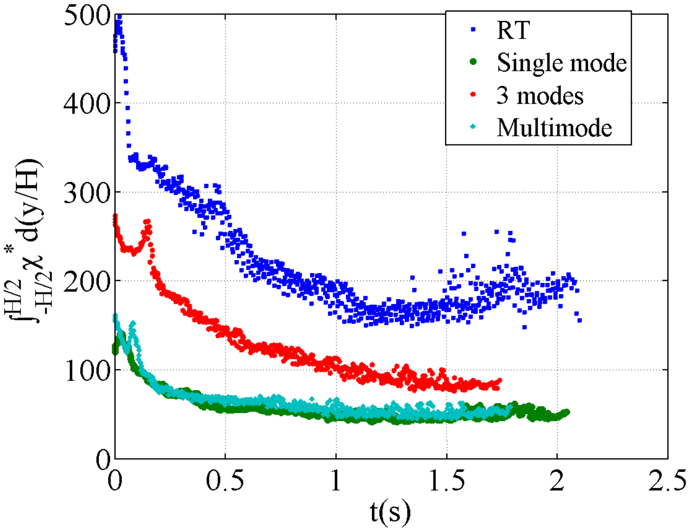

Figure 4.56: Scalar mixing variation.

An estimate of the amount of scalar mixing is given by the time mean of scalar dissipation parameter, $\chi^*(x,y) = |\nabla\rho^*(x,y)|^2/Sc$. Variation of the quantity $\int_{-\frac{H}{2}}^{\frac{H}{2}} \chi^*(x,y)\frac{dy}{H}$

along the geometrical centerline of the mixing layer, $y = 0$ is presented in Fig. 4.56. The spatial resolution of PLIF images is insufficient to observe fine-scale dissipation. Therefore, effect of ICs on scalar dissipation rate are inconclusive. However, the integral of dissipation rate along the mixing height gives a measure of the spread and sum of gradients. Thus, a larger initial dominant wavelength creates a mixing layer, which could show a greater value of the integral. However, such a trend is not observed in the figure. This indicates that large-scale gradients may be present in the mixing layer.

4.7 PIV measurement results

In this section, simultaneous measurement of density and velocity fields is performed using PLIF and PIV techniques simultaneously. Two locations are chosen for these measurements: A region immediately downstream of the splitter plate, i.e. $x/H \epsilon [0.16, 0.5]$ and a region far downstream of it in the turbulent zone, *i.e.* x/H ϵ [3.33, 3.75]. The imaging region is of size $\sim$ 10 cm × 10 cm at early-time, while it is larger, of size $\sim$ 12.7 cm × 12.7 cm at late-time. As the mixing layer grows with time, a larger region of the flow is captured to observe the large-scale structures present in the flow. To capture the small scale structures at late-time, greater spatial resolution is also required at late-time.

A thin planar sheet of the test section is illuminated using laser sheet from a pulsed laser. Rhodamine 6G, the fluorescein, is added only to the cold water tank, while Silver Coated Hollow Glass Spheres (SGHS) are added to both tanks. The amount of Rhodamine is sufficiently small to result in linear attenuation of incident laser light, while the amount of SGHS is sufficiently small to ignore particle agglomeration during experiment. While the PLIF camera has a resolution of 2 MPx, the PIV camera has a resolution of 1 MPx. Using a pulse generator, periodic pulses are sent to both cameras at 15 Hz. The PLIF camera obtains a single image after every pulse, while the PIV camera captures two images in double exposure mode. Using a exposure delay of 0.33 s, the set of images is captured at uniform intervals between pulses. Thus, the effective frequency ofPIV imaging is 30 Hz. While PLIF technique captures the fluoresced light from the illumination plane, the PIV technique captures the Mie-scattered light. As the wavelength of fluoresced light is greater than the incident light, a bandpass filter is used on the PLIF camera to capture it. On the other hand, a notch filter is used on PIV lens to capture the Mie-scattered light only and block fluoresced light. Images of a calibration target placed inside the Channel initially are used for spatial calibration of the region of interest (ROI). The list of cases studied using this setting is provided in Table 4.14.

Table 4.14: PIV experimental parameters.

IC type	Case #	λ_1 (cm)	λ_2 (cm)	λ_3 (cm)	β_1 (°)	β_2 (°)	A_t ($\times 10^{-4}$)	
							at x_1	at x_2
No flap RT	1	0	-	-	-	-	6.82	6.48
Single-mode	2	5	-	-	-	-	7.30	6.73
3 modes	3	5	3	2	45	90	5.96	7.00
11 modes	4	Broadband					7.30	6.48

Sets of Mie-scattered images are analyzed using Insight 4G® to obtain the velocity fields at known time from the start of image capture. 1000 images are obtained for each case, resulting in 500 velocity fields. The recursive PIV algorithm is used to obtain the best possible resolution from the images, without loss of accuracy. Statistical parameters of the flow are extracted from the velocity data.

Vector plots of sample instantaneous velocity fields for no flapper motion, single-mode, 3 modes and multi-mode cases are shown in Figures 4.57, 4.58, 4.59 and 4.60

respectively. The contours of velocity magnitude are also shown in the plots. From these instantaneous plots, a qualitative idea of the size of the large-scale structures at late-time is obtained. The motion of a pair of vortices is observed at early-time, while the turbulent flow at late-time is observed from these vector plots.

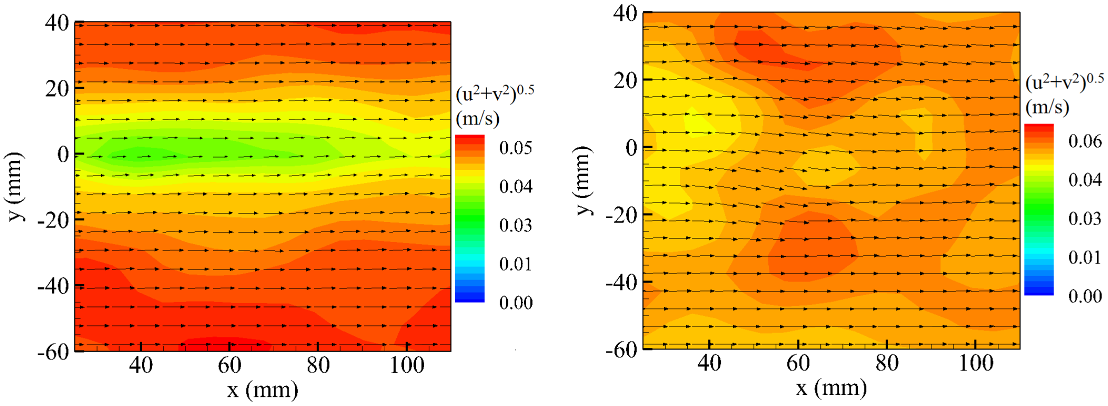

(a) $x/H = 0.16$ (b) $x/H = 3.33$

Figure 4.57: Instantaneous vector fields of no flapper motion case.

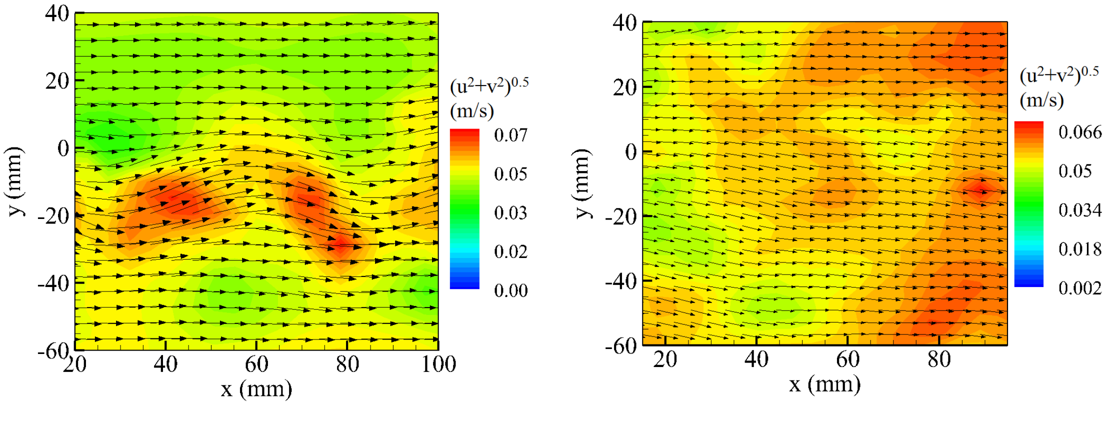

(a) $x/H = 0.16$ (b) $x/H = 3.33$

Figure 4.58: Instantaneous vector fields of single-mode case.

The mean (time averaged) velocity components are obtained for all cases. Profiles

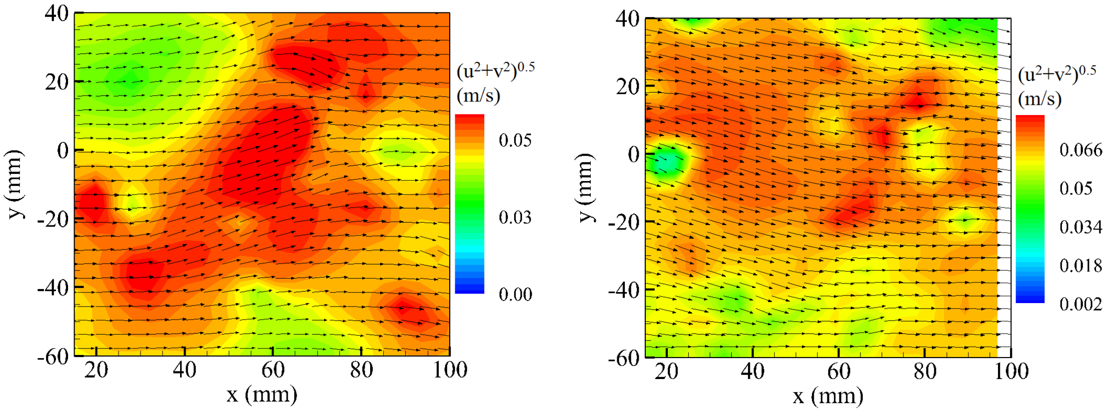

(a) $x/H = 0.16$ (b) $x/H = 3.33$

Figure 4.59: Instantaneous vector fields of 3 modes case.

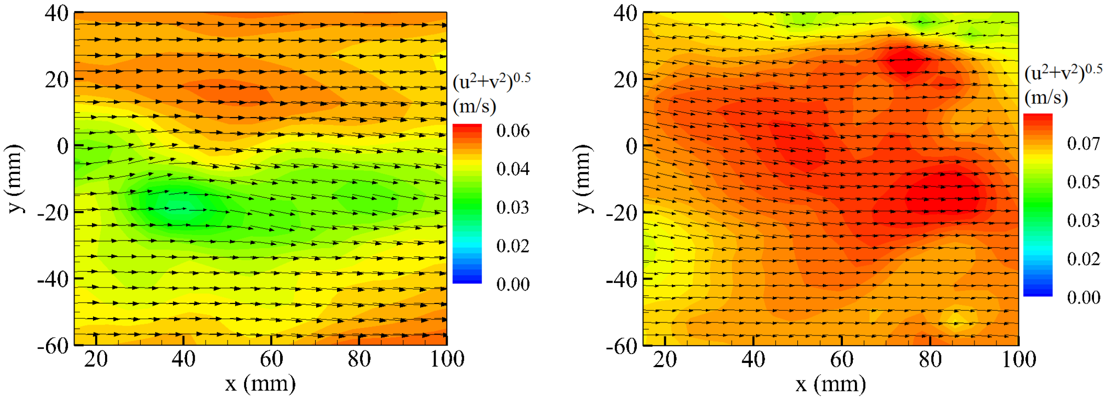

(a) $x/H = 0.16$ (b) $x/H = 3.33$

Figure 4.60: Instantaneous vector fields of broadband multi-mode case.

of $U =< u >$ along the centerline of the mixing layer with streamwise distance, x, is provided in Fig. 4.61. Profiles of $V =< v >$ along the centerline x are given in Fig. 4.62. The velocity deficit in the wake of the splitter plate is compensated to an extent by the motion of the flapper. This is corroborated by the plots of profiles of mean streamwise velocity component, $< u >$. The single-mode case pushes the flow much stronger than the other cases. Thus, by increasing the number of modes of the IC, effect of the flapper motion on $< u >$ is reduced. However, at late-time, magnitudes of $< u >$ for cases of flapper motion is close to each other, but different from the no-flap case. This indicates that effect of flapper motion is almost uniform for all IC types with a moving flapper. Profiles of the mean crosswise velocity component,

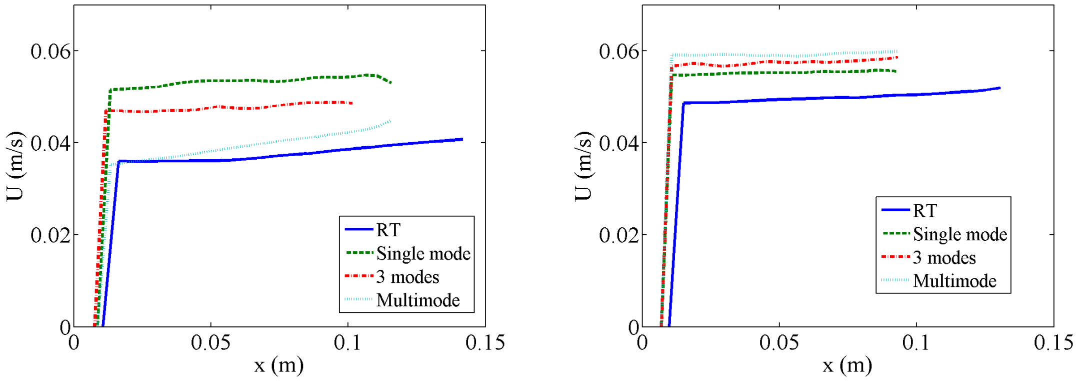

(a) $x/H = 0.16$ (b) $x/H = 3.33$

Figure 4.61: Profiles of U with streamwise distance, x, at early and late-times for all cases.

$V =< v >$, indicate that centroid of the mixing layer shifts down with time (see Fig. 4.62(b)). As the single-mode IC moves the fluid by the greatest amount in periodic waves, the spike velocity magnitude, $V =< v_s >$ is also much larger than the other IC cases at both early and late-times. Also, increasing the number of initial modes produces smaller eddies in the system at early-time, which saturate quicker than the larger eddies. This results in a greater amount of mixing of the streams, and reduced spike velocities at late-times. Even though the late-time flow for multi-mode IC may have larger eddies resulting from mode-coupling, the mean velocity components may not indicate the presence of this instantaneous phenomenon. Similarly, profiles of

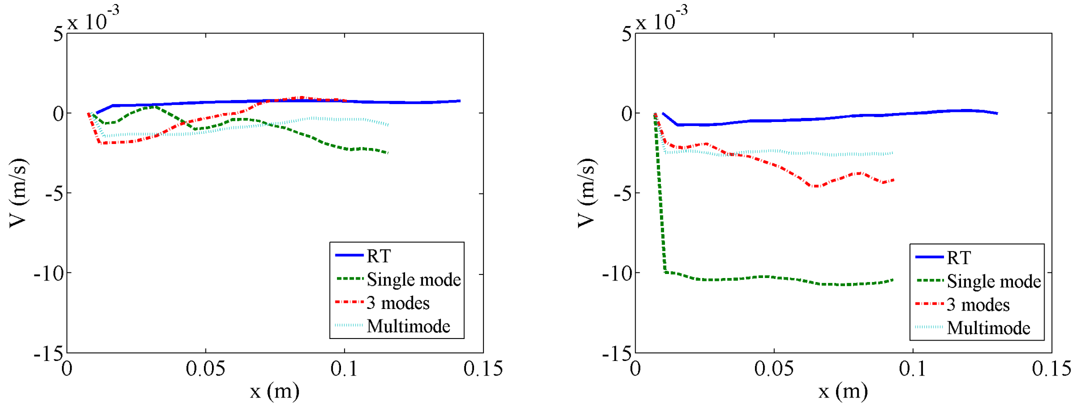

(a) $x/H = 0.16$ (b) $x/H = 3.33$

Figure 4.62: Profiles of V with streamwise distance, x, at early and late-times for all cases.

$U = < u >$ and $V = < v >$ with crosswise distance, y are plotted in Figures 4.63 and 4.64 respectively. Profiles of U in Fig. 4.63 indicate the velocity deficit at early-time and the compensating effect of flapper motion at late-time. This is in agreement with the above discussion. Plots of V with crosswise displacement, y, at early and late-time provide the bubble and spike velocities across the mixing layer at streamwise locations of $x/H = 0.16$ and $x/H = 3.33$, respectively. The profiles indicate that the single-mode case shows the largest bubble and spike velocity at late-time. At early-time, however, a definite trend is not discerned. This could be due to uncertainty in the measurements or due to insufficient duration of measurement.

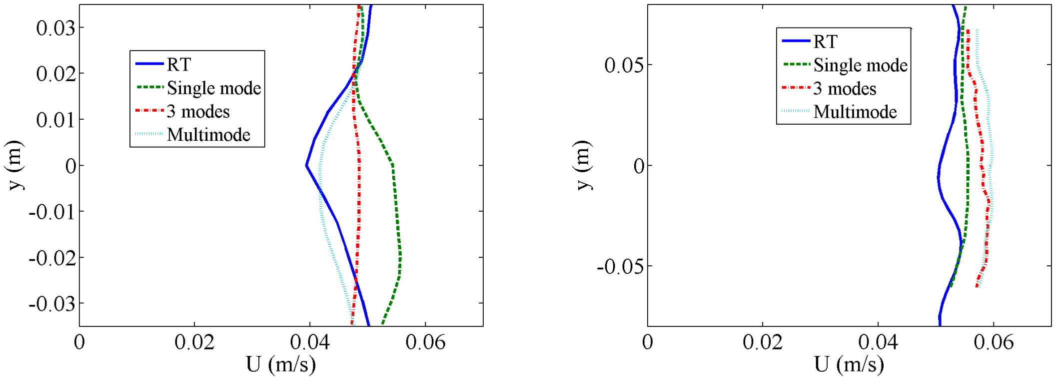

(a) $x/H = 0.16$ (b) $x/H = 3.33$

Figure 4.63: Profiles of U with crosswise distance, y, at early and late-times for all cases.

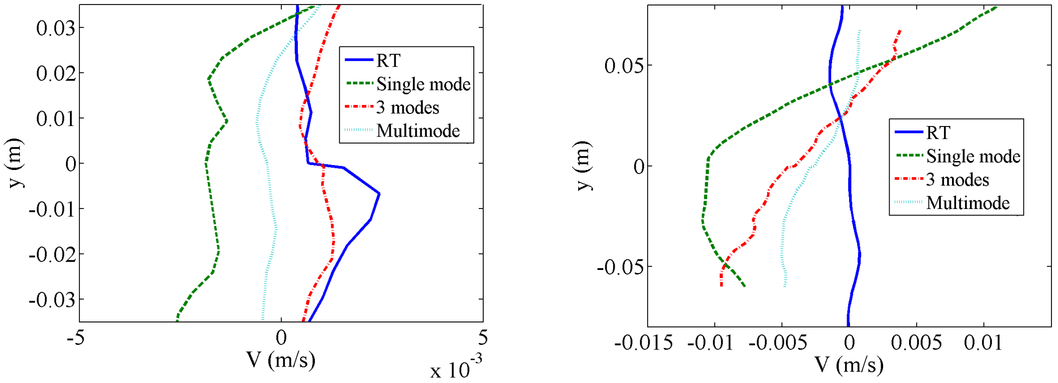

(a) $x/H = 0.16$ (b) $x/H = 3.33$

Figure 4.64: Profiles of V with crosswise distance, y, at early and late-times for all cases.

Profiles of turbulence intensity, given by $I_t = < u'^2 + v'^2 >$ are given in Figures 4.65 and 4.66 respectively. The profiles indicate that the multi-mode case has high turbulence intensities at late-time, comparable to the 3 modes case. On the other hand, the single-mode case shows a peculiarly high turbulence intensity at early-time. This may be due to fluctuations in flapper motion profile. The flapper motion has a maximum uncertainty of $\approx 10\%$ under operating conditions. The motion of the axis of the servo motor is incremental between time steps, which may result in overshoot. This may results in continual adjustment of flapper profile. Thus, there may be additional small scale fluctuations due to flapper motion at early-time. However, these fluctuations are expected to be similar for all cases involving a moving flapper.

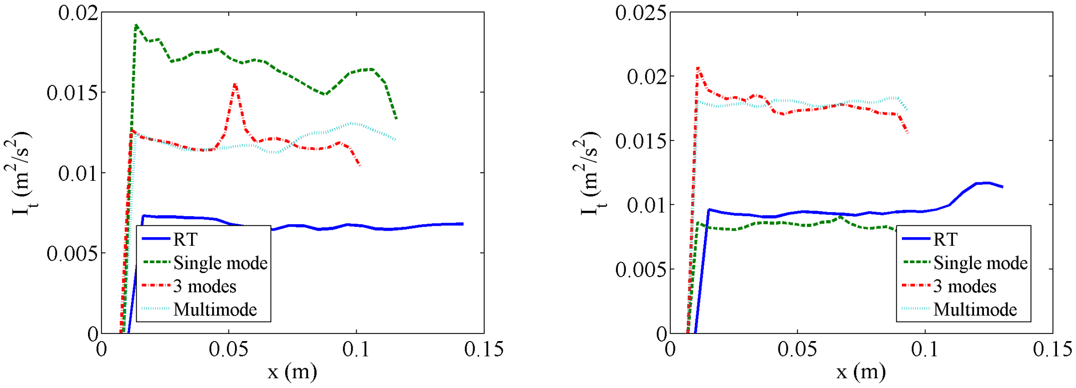

(a) $x/H = 0.16$ (b) $x/H = 3.33$

Figure 4.65: Profiles of turbulence intensity with streamwise distance, x, at early and late-times for all cases.

Histograms of fluctuating velocity components, u' and v' at the center of the mixing layer at early and late-times are provided in Figures 4.67 and 4.68 respectively. Widening of the histograms at late-time is witnessed due to evolution of the Rayleigh-Taylor mixing layer. The histograms of the 3 modes case and the multi-mode case are wider than the remaining cases, as a greater amount of mixing and range of length and time scales is observed with increasing the number of modes of the IC.

Finally, spectra of u' and v' at early and late-times are reported in Figures 4.69 and 4.70 respectively. The spectra of $< v' >$ show a cascading profile characteristic of turbulent flows. However, due to limited temporal resolution of the PIV technique,

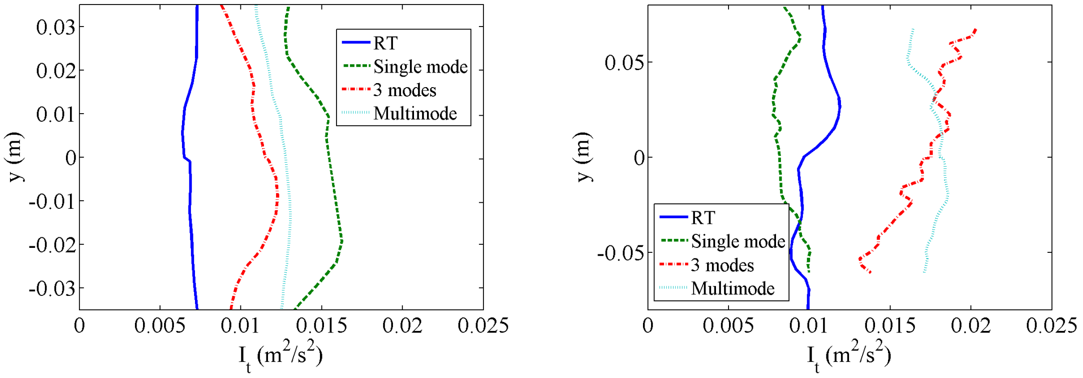

(a) $x/H = 0.16$

(b) $x/H = 3.33$

Figure 4.66: Profiles of turbulence intensity with crosswise distance, y, at early and late-times for all cases.

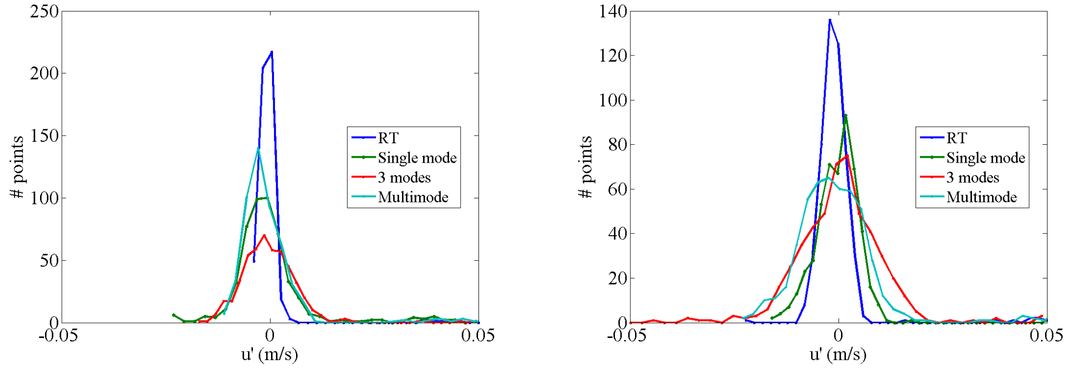

(a) $x/H = 0.16$

(b) $x/H = 3.33$

Figure 4.67: Histograms of fluctuating velocity component, u', at early and late-times for all cases.

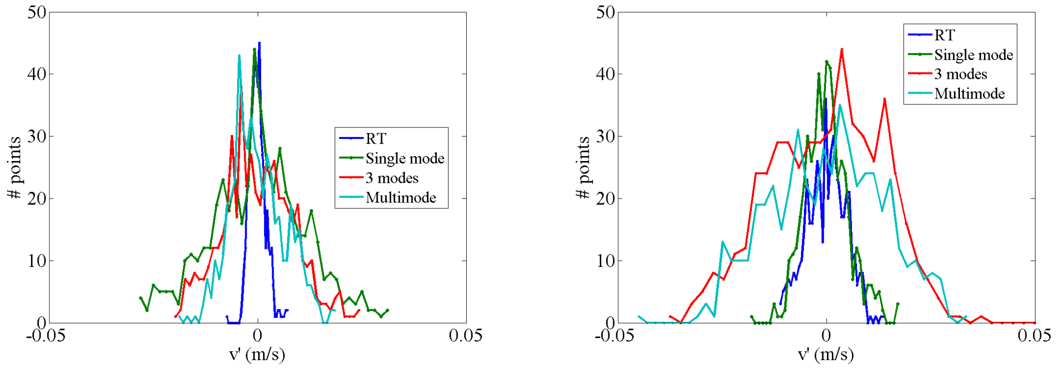

(a) $x/H = 0.16$ (b) $x/H = 3.33$

Figure 4.68: Histograms of fluctuating velocity component, v', at early and late-times for all cases.

only a few decades of the inertial range are measured in these experiments.

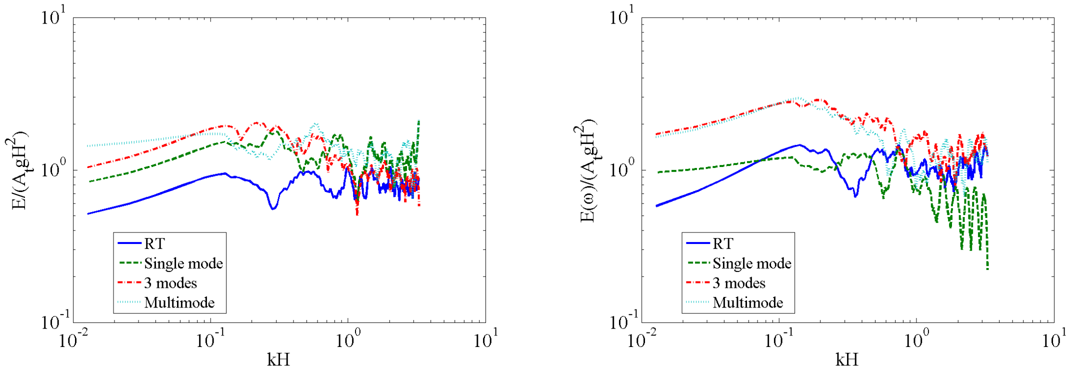

(a) $x/H = 0.16$ (b) $x/H = 3.33$

Figure 4.69: Power spectra of fluctuating velocity component, u', at early and late-times for all cases.

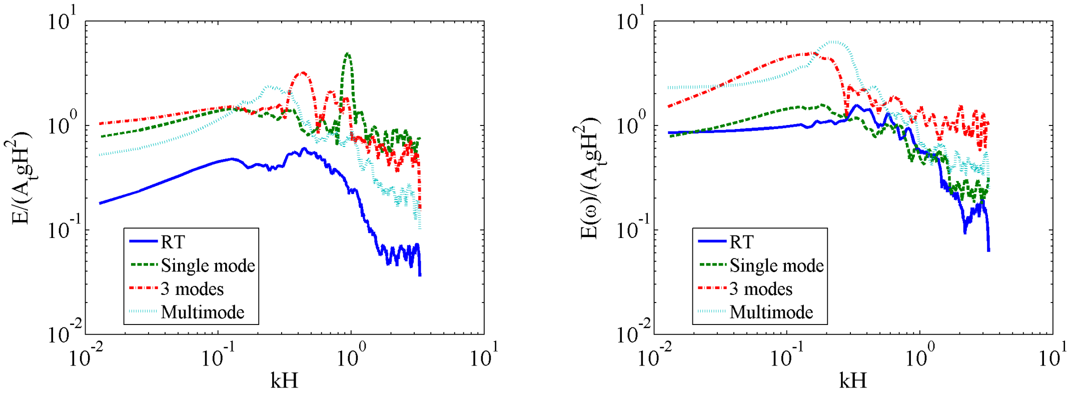

(a) $x/H = 0.16$

(b) $x/H = 3.33$

Figure 4.70: Power spectra of fluctuating velocity component, v', at early and late-times for all cases.

5. CONCLUSION AND FUTURE WORK

5.1 Conclusion

From the above discussion on total mixing, molecular mixing and fine-scale mixing rate (scalar dissipation rate), the following observations are generally observed, regarding the effect of initial conditions on RTI:

1. Using the flapper mechanism, the ability to generate a controlled IC is proven by the current experiments. The scaling of increased mixing width with wavelength of a single-mode IC needs to be performed, for all stages of RTI evolution.

2. Typical of RTI structures, the larger wavelengths induce enhanced molecular mixing (witnessed in parameter, θ), into the flow field, which is also observed from the magnitude of density gradients. Measurement of θ and χ from PLIF imaging is limited by spatial resolution, as the dissipation range is not observed.

3. Changing the phase angle for a binary-mode ICdoes not seem to significantly affect the total mixing from ensemble averaging, while there is a clear indication of the presence of localized shear in the flow field. This might mean that the ensemble averaging technique may not be able to capture the localized fluctuations in density, corresponding to smaller time-scales. Also, the amount of molecular mixing is significantly affected by the phase angle. It can be therefore, concluded that more measurements (using perhaps different diagnostics) of the mixing layer evolution are required for understanding the effect of shear on Rayleigh-Taylor mixing.

4. Multi-modal interaction is clearly affecting the mixing layer evolution, hence, it

can possibly affect ‘late-time’ behavior of the instability. In order to verify this, turbulent statistics are required at different stages of evolution, for different ICs.

5. The ICs used in our experiments caused a significant amount of initial vorticity comparable to the baroclinic vorticity at the low Atwood numbers characteristic of our system. However, the initial vorticity dissipates quickly in the absence of buoyancy, while the presence of buoyancy greatly enhances mixing.

6. The greater challenge presented by this study lies in founding a scaling law for these multi-modal cases, especially due to the reduced complexity in the current set of experiments, i.e., the symmetry of the spikes and bubbles at these low Atwood numbers, and the limited range of variation of wavelengths of the ICs.

5.2 Future work

Thus, based on the above observations, the following future work is proposed to improve our understanding of RTI physics, as well as to gather a better answer to the questions raised in §2.3:

1. The velocity and density statistics are limited by spatial and temporal resolution of the diagnostics employed. For observing the dissipation scales, higher spatial resolution PLIF imaging is desired, while for observing the dissipation scales in velocity power spectra, a greater temporal resolution of the PIV technique is desired.

2. Treating the IC problem from a dynamic systems approach, the path to chaos may be observed for different number of modes of the IC. Also, the effect of phase angle can be understood better.

3. Apart from the above, the experimental data can be used for validating models of Rayleigh-Taylor turbulence, to make them more robust (for all types of ICs), and to extrapolate this behavior for high Atwood number flows.

REFERENCES

S. I. Abarzhi (2010). ‘Review of theoretical modelling approaches of Rayleigh-Taylor instabilities and turbulent mixing’. *Phil. Trans. Royal Soc. A: Math., Phys. and Engg. Sci.* **368**(1916):1809–1828.

S. I. Abarzhi, et al. (2005). ‘Rayleigh-Taylor turbulent mixing of immiscible, miscible and stratified fluids’. *Phys. Fluids* **17**(8):081705.

S. I. Abarzhi, et al. (2003). ‘Rayleigh-Taylor and Richtmyer-Meshkov instabilities for fluids with a finite density ratio’. *Phys. Lett. A* **317**(5-6):470–476.

B. Akula, et al. (2013). ‘Effect of shear on Rayleigh-Taylor mixing at small Atwood number’. *Phys. Rev. E* **87**(3):033013.

U. Alon, et al. (1995). ‘Power laws and similarity of Rayleigh-Taylor and Richtmyer-Meshkov mixing fronts at all density ratios’. *Phys. Rev. Lett.* **74**(4):534–537.

M. J. Andrews & S. B. Dalziel (2010). ‘Small Atwood number Rayleigh-Taylor experiments’. *Phil. Trans. Royal Soc. A: Math., Phys. and Engg. Sci.* **368**(1916):1663–1679.

M. J. Andrews, et al. (2012). ‘Test problem: tilted Rayleigh-Taylor for 2-D mixing studies’. Tech. rep., Los Alamos National Laboratory.

A. Banerjee & M. J. Andrews (2006). ‘Statistically steady measurements of Rayleigh-Taylor mixing in a gas channel’. *Phys. Fluids* **18**(3):035107.

A. Banerjee & M. J. Andrews (2009). ‘3D simulations to investigate initial condition effects on the growth of Rayleigh-Taylor mixing'. *Intl. J. Heat and Mass Transfer* **52**(17):3906–3917.

A. Banerjee, et al. (2010). 'Development and validation of a turbulent-mix model for variable-density and compressible flows'. *Phys. Rev. E* **82**:046309.

C. Baumgarten (2006). *Mixture formation in internal combustion engines.* Springer Berlin Heidelberg.

J. B. Bell & D. L. Marcus (1992). 'A second-order projection method for variable-density flows'. *J. Comp. Phys.* **101**(2):334–348.

D. C. Besnard, et al. (1996). 'Spectral transport model for turbulence'. *Theoretical and Comp. Fluid Dyn.* **8**:1–35.

G. Boffetta, et al. (2012). 'Bolgiano scale in confined Rayleigh-Taylor turbulence'. *J. Fluid Mech.* **690**:426–440.

G. Boffetta, et al. (2009). 'Kolmogorov scaling and intermittency in Rayleigh-Taylor turbulence'. *Phys. Rev. E* **79**:065301.

R. Bolgiano Jr (1959). 'Turbulent spectra in a stably stratified atmosphere'. *J. Geophys. Research* **64**(12):2226–2229.

K. A. Buch & W. J. A. Dahm (1996). 'Experimental study of the fine-scale structure of conserved scalar mixing in turbulent shear flows. Part 1. Sc$\gg$1'. *J. Fluid Mech.* **317**:21–71.

W. Cabot & Y. Zhou (2013). 'Statistical measurements of scaling and anisotropy of turbulent flows induced by Rayleigh-Taylor instability'. *Phys. Fluids* **25**:015107.

W. H. Cabot & A. W. Cook (2006). 'Reynolds number effects on Rayleigh-Taylor instability with possible implications for type Ia supernovae'. *Nature Phys.* **2**(8):562–568.

P. Carles, et al. (2006). 'Rayleigh-Taylor Instability for immiscible fluids of arbitrary viscosities: A magnetic levitation investigation and theoretical Model'. *Phys. Rev. Lett.* **96**:104501.

S. Chandrasekhar (1961). *Hydrodynamic and hydromagnetic instability.* Clarendon Press, Oxford.

B. Cheng, et al. (2000). 'Density dependence of Rayleigh-Taylor and Richtmyer-Meshkov mixing fronts'. *Phys. Lett. A* **268**(4-6):366–374.

B. Cheng & A. J. Scannapieco (2005). 'Buoyancy-drag mix model obtained by multifluid interpenetration equations'. *Phys. Rev. E* **72**:046310.

D. Chung & D. I. Pullin (2010). 'Direct numerical simulation and large-eddy simulation of stationary buoyancy-driven turbulence'. *J. Fluid Mech.* **643**:279–308.

R. Clift, et al. (2005). *Bubbles, drops, and particles.* Courier Dover Publications.

B. G. Comte & S. Corrsin (1971). 'Simple Eulerian time correlation of full and narrow-band velocity signals in grid-generated, isotropic turbulence'. *J. Fluid Mech.* **48**(2):273–337.

A. W. Cook & P. E. Dimotakis (2001). 'Transition stages of Rayleigh-Taylor instability between miscible fluids'. *J. Fluid Mech.* **443**:69–99.

A. W. Cook & Y. Zhou (2002). 'Energy transfer in Rayleigh-Taylor instability'. *Phys. Rev. E* **66**:026312.

W. Dahm & P. Dimotakis (1987). ‘Measurements of entrainment and mixing in turbulent jets’. *AIAA J.* **25**(9):1216–1223.

B. J. Daly (1969). ‘Numerical study of the effect of surface tension on interface instability’. *Phys. Fluids* **12**(7):1340–1354.

S. B. Dalziel, et al. (1999). ‘Self-similarity and internal structure of turbulence induced by Rayleigh-Taylor instability’. *J. Fluid Mech.* **399**:1–48.

P. Danckwerts (1952). ‘The definition and measurement of some characteristics of mixtures’. *Applied Scientific Research* **3**:279–296.

G. Dimonte (2000). ‘Spanwise homogeneous buoyancy-drag model for Rayleigh-Taylor mixing and experimental evaluation’. *Phys. Plasmas* **7**(6).

G. Dimonte (2004). ‘Dependence of turbulent Rayleigh-Taylor instability on initial perturbations’. *Phys. Rev. E* **69**:056305.

G. Dimonte & M. Schneider (1996). ‘Turbulent Rayleigh-Taylor instability experiments with variable acceleration’. *Phys. Rev. E* **54**:3740–3743.

Y. Doron & A. Duggleby (2011). ‘Optical density measurements and analysis for single-mode initial-condition buoyancy-driven mixing’. *J. Fluids Engg.* **133**(10):101204.

E. Fermi, et al. (1955). *Taylor instability of incompressible liquids.* United States Atomic Energy Commission, Technical Information Service.

A. Ferrier, et al. (1993). ‘Application of optical techniques to the study of plumes in stratified fluids’. *Dyn. Atmospheres and Oceans* **20**(1):155–183.

N. Freed, et al. (1991). 'Two-phase flow analysis of self-similar turbulent mixing by Rayleigh-Taylor instability'. *Phys. Fluids A: Fluid Dyn.* **3**(5):912–918.

J. Glimm, et al. (2011). 'New directions for Rayleigh-Taylor mixing'. *Phil. Trans. Royal Soc. A: Turbulent mixing and beyond* **371**(2003):20120183.

V. N. Goncharov (2002). 'Analytical model of nonlinear, single-mode, classical Rayleigh-Taylor instability at arbitrary Atwood numbers'. *Phys. Rev. Lett.* **88**:134502.

J. H. Hammer, et al. (1999). 'High yield inertial confinement fusion target design for a z-pinch-driven hohlraum'. *Phys. Plasmas* **6**(5):2129.

Z. Huang, et al. (2007). 'Rayleigh-Taylor instability experiments with precise and arbitrary control of the initial interface shape'. *Phys. Rev. Lett.* **99**:204502.

T. Ikegawa & K. Nishihara (2003). 'Saturation and postsaturation phenomena of Rayleigh-Taylor instability with adjacent modes'. *Phys. Rev. E* **67**:026404.

J. W. Jacobs (1992). 'Shock-induced mixing of a light-gas cylinder'. *J. Fluid Mech.* **234**:629–649.

P. S. Karasso & M. G. Mungal (1997). 'PLIF measurements in aqueous flows using the Nd:YAG laser'. *Exp. Fluids* **23**:382–387.

M. Kelley, et al. (1976). 'Evidence for a Rayleigh-Taylor type instability and upwelling of depleted density regions during equatorial spread F'. *Geophys. Research Lett.* **3**(8):448–450.

R. Kellogg & S. Corrsin (1980). 'Evolution of a spectrally local disturbance in grid-generated, nearly isotropic turbulence'. *J. Fluid Mech.* **96**:641–669.

J. Kestin, et al. (1978). 'Viscosity of liquid water in the range 8°C to 150°C'. *J. Phys. Chem.* **7**(3):941–948.

K. Kifonidis, et al. (2006). 'Non-spherical core collapse supernovae. II. The late-time evolution of globally anisotropic neutrino-driven explosions and their implications for SN 1987 A'. *Astronomy and Astrophys.* **453**:661–678.

W. Kraft (2008). *Simultaneous and instantaneous measurement of velocity and density in Rayleigh-Taylor mixing layers.* Ph.d. thesis, Texas A&M University, College Station, TX, USA.

Y. A. Kucherenko, et al. (1991). 'Experimental study of the gravitational turbulent mixing self-similar mode'. In *3rd Intl Workshop on the Physics of Compressible Turbulent Mixing, Cambridge University (ed. R. Dautray)*, pp. 427–454.

S. Kuchibhatla (2010). 'Experimental investigation of the effect of initial conditions on Rayleigh-Taylor instability'. Masters thesis, Texas A&M University, College Station, TX, USA.

S. Kuchibhatla & D. Ranjan (2013a). 'Effect of initial conditions on Rayleigh-Taylor mixing: modal interaction'. *Physica Scripta* **2013**(T155):014057.

S. Kuchibhatla & D. Ranjan (2013b). 'Rayeligh-Taylor experiments'. In *Proc. ASME FEDSM'12*, Houston, TX, USA.

D. J. Kulkula (1981). 'Thermodynamic and transport properties of pure and saline water'. Masters thesis, State university of New York, Buffalo, NY, USA.

A. G. Lawrie & S. B. Dalziel (2011). 'Rayleigh-Taylor mixing in an otherwise stable stratification'. *J. Fluid Mech.* **688**:507.

D. Layzer (1955). ‘On the instability of superposed fluids in a gravitational field’. *The Astrophys. J.* **122**:1–12.

K. A. Leicht (1997). *Effect of initial conditions on Rayleigh-Taylor mixing development.* Ph.d. thesis, Texas A&M University, College Station, TX, USA.

D. J. Lewis (1950). ‘The instability of liquid surfaces when accelerated in a direction perpendicular to their planes. II’. *Proc. Royal Soc. of London. Series A, Math. and Phys. Sci.* **202**:81–96.

H. Lim, et al. (2010). ‘Nonideal Rayleigh-Taylor mixing’. *Proc. National Academy Sci.* **107**(29):12786–12792.

P. F. Linden & J. M. Redondo (1991). ‘Molecular mixing in Rayleigh-Taylor instability. Part I: Global mixing.’. *Phys. Fluids A* **3**(5):1269.

P. F. Linden, et al. (1994). ‘Molecular mixing in Rayleigh-Taylor instability’. *J. Fluid Mech.* **265**:97–124.

J. D. Lindl & W. C. Mead (1975). ‘Two-dimensional simulation of fluid instability in laser-fusion pellets’. *Phys. Rev. Lett.* **34**:1273–1276.

D. Livescu, et al. (2009). ‘High-Reynolds number Rayleigh-Taylor turbulence’. *J. Turbulence* **10**(13):1–32.

D. Livescu, et al. (2010). ‘New phenomena in variable-density Rayleigh-Taylor turbulence’. *Physica Scripta* **2010**(T142):014015.

D. Livescu & T. Wei (2012). ‘Direct numerical simulations of Rayleigh-Taylor instability with gravity reversal’. In *Proc. ICCFD7*, p. 2304, Hawaii.

D. Livescu, et al. (2011). 'Direct numerical simulations of Rayleigh-Taylor instability'. *J. Phys.: Conference Series* **318**(8):082007.

F. E. Marble (1985). 'Growth of a diffusion flame in the field of a vortex'. In *Recent advances in the aero. sci.*, pp. 395–413. Plenum Press, NY, USA.

O. Marchal & J. Mutterer (2005). 'Haar Wavelet Filter and Adaptive Median Filter'.

M. M. Marinak, et al. (1998). 'Nonlinear Rayleigh-Taylor evolution of a three-dimensional multimode perturbation'. *Phys. Rev. Lett.* **80**:4426–4429.

K. O. Mikaelian (2003). 'Explicit expressions for the evolution of single-mode Rayleigh-Taylor and Richtmyer-Meshkov instabilities at arbitrary Atwood numbers'. *Phys. Rev. E* **67**:026319.

J. Milovich, et al. (2006). 'Highly-resolved 2D HYDRA simulations of double-shell ignition designs'. Tech. rep., UCRL-PROC-222562, Lawrence Livermore National Laboratory (LLNL), Livermore, CA.

J. L. Milovich, et al. (2004). 'Multimode short-wavelength perturbation growth studies for the National Ignition Facility double-shell ignition target designs'. *Phys. Plasmas* **11**(4):1552 – 1568.

N. J. Mueschke (2004). 'An investigation of the influence of initial conditions on Rayleigh-Taylor mixing'. Masters thesis, Texas A&M University, College Station, TX, USA.

N. J. Mueschke (2008). *Experimental and numerical study of molecular mixing dynamics in Rayleigh-Taylor unstable flows.* Ph.d. thesis, Texas A&M University, College Station, TX, USA.

N. J. Mueschke, et al. (2006). 'Experimental characterization of initial conditions and spatio-temporal evolution of a small-Atwood-number Rayleigh-Taylor mixing layer'. *J. Fluid Mech.* **567**:27–63.

A. Obukhov (1959). 'Effect of Archimedean forces on the structure of the temperature field in a turbulent flow'. In *Dokl. Akad. Nauk SSSR*, vol. 125, p. 1246.

D. H. Olson & J. W. Jacobs (2009). 'Experimental study of Rayleigh-Taylor instability with a complex initial perturbation'. *Phys. Fluids* **21**(3):034103.

D. Oron, et al. (2001). 'Dimensionality dependence of the Rayleigh-Taylor and Richtmyer-Meshkov instability late-time scaling laws'. *Phys. Plasmas* **8**(6):2883.

F. M. Peart (2008). 'Effect of initial conditions on the development of Rayleigh-Taylor instabilities'. Masters thesis, Texas A&M University, College Station, TX, USA.

J. D. Pelletier (2008). *Quantitative modeling of earth surface processes*, vol. 304. Cambridge University Press Cambridge.

P. Ramaprabhu (2003). *On the dynamics of Rayleigh-Taylor mixing.* Ph.d. thesis, Texas A&M University, College Station, TX, USA.

P. Ramaprabhu & M. J. Andrews (2003). 'Simultaneous measurements of velocity and density in buoyancy-driven mixing'. *Exp. Fluids* **34**:98–106.

P. Ramaprabhu & M. J. Andrews (2004). 'Experimental investigation of Rayleigh-Taylor mixing at small Atwood numbers'. *J. Fluid Mech.* **502**:233–271.

P. Ramaprabhu & G. Dimonte (2005). 'Single-mode dynamics of the Rayleigh-Taylor instability at any density ratio'. *Phys. Rev. E* **71**:036314.

P. Ramaprabhu, et al. (2005). ‘A numerical study of the influence of initial perturbations on the turbulent Rayleigh-Taylor instability’. *J. Fluid Mech.* **536**:285–319.

P. Ramaprabhu, et al. (2012). ‘The late-time dynamics of the single-mode Rayleigh-Taylor instability’. *Phys. Fluids* **24**(7):074107.

P. Ramaprabhu, et al. (2013). ‘The Rayleigh-Taylor Instability driven by an accel-decel-accel profile’. *Phys. Fluids* **25**(11):115104.

L. Rayeligh (1883). ‘Investigations of the character of the equilibrium of an incompressible heavy fluid of variable density’. *Proc. London Math. Soc.* **14**:170–177.

K. I. Read (1984). ‘Experimental investigation of turbulent mixing by Rayleigh-Taylor instability’. *Phys. D: Nonlinear Phenomena* **12**(1-3):45–58.

J. Z. Reid, et al. (2013). ‘Density measurements of a turbulent wake using acetone planar laser-Induced fluorescence’. *AIAA J.* **51**(4):829–839.

J. R. Ristorcelli & T. T. Clark (2004). ‘Rayleigh-Taylor turbulence: self-similar analysis and direct numerical simulations’. *J. Fluid Mech.* **507**:213–253.

B. Rollin & M. J. Andrews (2010). ‘On the “early-time” evolution of variables relevant to turbulence models for the Rayleigh-Taylor instability’. In *Proc. FEDSM-ICNMM2010*, pp. 1–7, Montreal, Quebec, Canada.

A. J. Scannapieco & S. L. Ossakow (1976). ‘Nonlinear equatorial spread F’. *Geophys. Research Lett.* **3**(8):451–454.

A. J. Schmitt, et al. (2001). ‘Growth of pellet imperfections and laser imprint in direct drive inertial confinement fusion targets’. *Phys. Plasmas* **8**(5):2287.

D. M. Snider & M. J. Andrews (1994). 'Rayleigh-Taylor and shear driven mixing with an unstable thermal stratification'. *Phys. Fluids* **6**(10):3324.

D. M. Snider & M. J. Andrews (1995). 'An inexpensive method for quantitative data collection from photographic prints'. *Meas. Sci. and Tech.* **6**(5):502.

S. Sohn (2003). 'Simple potential-flow model of Rayleigh-Taylor and Richtmyer-Meshkov instabilities for all density ratios'. *Phys. Rev. E* **67**:026301.

S. Sohn (2009). 'Effects of surface tension and viscosity on the growth rates of Rayleigh-Taylor and Richtmyer-Meshkov instabilities'. *Phys. Rev. E* **80**:055302.

M. J. Steinkamp, et al. (1999). 'Two-point description of two-fluid turbulent mixing - I. Model formulation'. *Intl. J. Multiphase Flow* **25**(4):599–637.

L. K. Su & N. T. Clemens (2003). 'The structure of fine-scale scalar mixing in gas-phase planar turbulent jets'. *J. Fluid Mech.* **488**:1–29.

G. Taylor (1950). 'The instability of liquid surfaces when accelerated in a direction perpendicular to their planes. I'. *Proc. Royal Soc. of London. Series A. Math. and Phys. Sci.* **201**(1065):192–196.

C. Tomkins, et al. (2008). 'An experimental investigation of mixing mechanisms in shock-accelerated flow'. *J. Fluid Mech.* **611**:131–150.

V. Tsiklashvili, et al. (2012). 'An experimental study of small Atwood number Rayleigh-Taylor instability using the magentic levitation of paramagnetic fluids'. *Phys. Fluids* **24**(15):052106.

J. T. Waddell, et al. (2001). 'Experimental study of Rayleigh-Taylor instability: Low Atwood number liquid systems with single-mode initial perturbations'. *Phys. Fluids* **13**(5):1263.

D. Walker (1987). 'A fluorescence technique for measurement of concentration in mixing liquids'. *J. Phys. E: Scientific Instruments* **20**(2):217.

C. Weber (2012). *Turbulent mixing maesurements in the Richtmyer-Meshkov Instability*. Ph.d. thesis, University of Wisconsin, Madison, WI, USA.

D. Webster, et al. (2001). 'Simultaneous DPTV/PLIF measurements of a turbulent jet'. *Exp. Fluids* **30**(1):65–72.

T. Wei & D. Livescu (2012). 'Late-time quadratic growth in single-mode Rayleigh-Taylor instability'. *Phys. Rev. E* **86**:046405.

J. White, et al. (2010). 'Experimental measurements of the nonlinear Rayleigh-Taylor instability using a magnetorheological fluid'. *Phys. Rev. E* **81**:026303.

J. P. Wilkinson & J. W. Jacobs (2007). 'Experimental study of the single-mode three-dimensional Rayleigh-Taylor instability'. *Phys. Fluids* **19**(12):124102.

P. Wilson & M. Andrews (1999). 'Spectral nonequilibrium in a turbulent mixing layer'. *Phys. Fluids* **11**(8):2425.

P. N. Wilson & M. J. Andrews (2002). 'Spectral measurements of Rayleigh-Taylor mixing at small Atwood number'. *Phys. Fluids* **14**(3):938.

D. L. Youngs (1984). 'Numerical simulation of turbulent mixing by Rayleigh-Taylor instability'. *Phys. D: Nonlinear Phenomena* **12**(1-3):32–44.

D. L. Youngs (1989). 'Modelling turbulent mixing by Rayleigh-Taylor instability'. *Physica D: Nonlinear Phenomena* **37**(1-3):270–287.

D. L. Youngs (1994). 'Numerical simulation of mixing by Rayleigh-Taylor and Richtmyer-Meshkov instabilities'. *Laser and Particle Beams* **12**(04):725–750.

APPENDIX A

VALIDATION OF FLAPPER GENERATED PROFILES[*]

Most of the discussion and all Figures in this section are reproduced from Kuchibhatla & Ranjan (2013b) with permission from ASME. The flapper system is validated using a chart plotter that moves a graph sheet at a uniform speed of ≈ 5 cms^{-1}. Time dependent profiles of the flapper tip during operation are plotted on the graph sheet for single and binary-mode initial conditions. The amplitude and time period, t_p, of the motion profiles of the flapper tip are measured and compared with servo input to determine their accuracy (The uncertainty is determined to be $\approx 10\%$ for multi-mode). Figure A.1 shows the profile of the flapper for a binary-mode IC with (λ_1, λ_2, β) = (3 cm, 2 cm, 0°) and time periods of ($t_{p,1}$, $t_{p,2}$) = (5 s, 2 s).

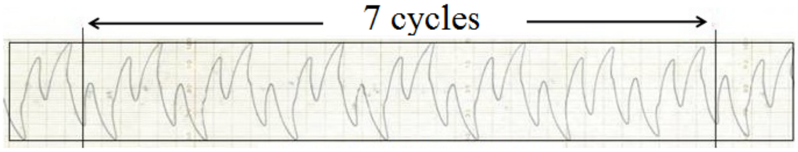

Figure A.1: Flapper motion profile. Figure taken from Kuchibhatla & Ranjan (2013b).

A plot of probability of intensity vs. pixel intensity along the horizontal centerline for the backlight is given in Fig. A.2. It depicts a Gaussian distribution for each color mode that is centered about the peak intensity. For a given dye, the background color mode with the most uniformity can be selected by constructing similar plots to Fig. A.2. The ensemble averaging process using backlit imaging is described in detail in Banerjee & Andrews (2006) and Kuchibhatla (2010). Using

---

[*] Reprinted with permission from “Rayleigh-Taylor experiments” by Kuchibhatla, S. & Ranjan, D., 2013. Proceedings of ASME FEDSM 2012, Copyright 2013 by ASME.

a calibration wedge, variation of pixel intensity with dye concentration is observed. Beer-Lambert's principle relates the intensity of light passing through a solute vs. the concentration of solute. It is verified that water density varies linearly with pixel intensity. Figure A.3 shows the linear variation of calibration image intensity (in different backlight color modes), while the probability of intensity is plotted in Fig. A.4.

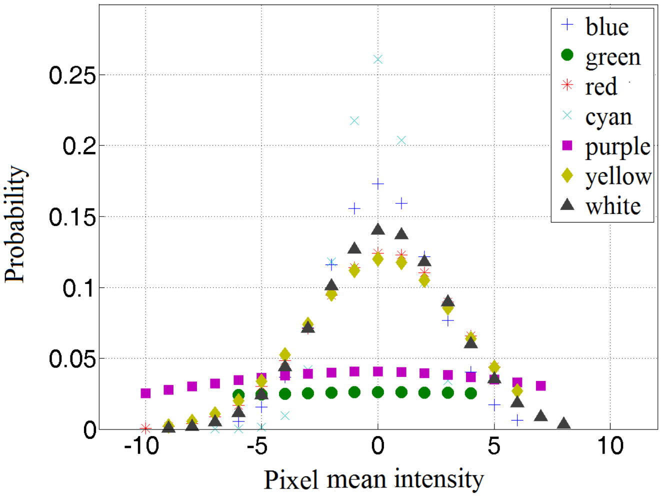

Figure A.2: Probability plot of intensity for different backlight color modes. Figure taken from Kuchibhatla & Ranjan (2013b).

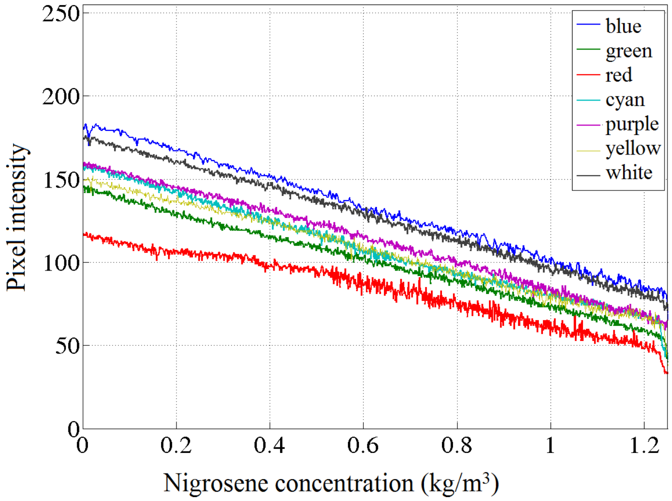

Figure A.3: Pixel intensity vs. dye concentration. Figure taken from Kuchibhatla & Ranjan (2013b).

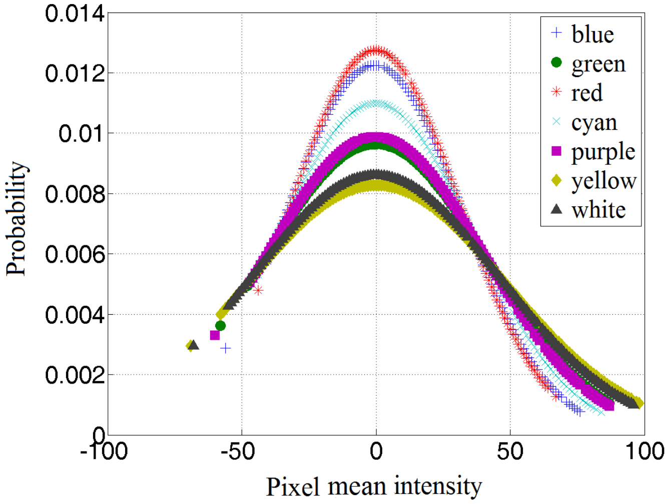

Figure A.4: Probability of pixel intensity for dye calibration study. Figure taken from Kuchibhatla & Ranjan (2013b).

APPENDIX B

VALIDATION OF MOLECULAR MIXING DATA*

Most of the discussion and all Figures in this section are reproduced from Kuchibhatla & Ranjan (2013b) with permission from ASME. The molecular mixing parameters for case 1 in Table 4.7 is presented in Figures B.1, B.2, B.3 and B.4. The number of data points in these plots is insufficient at $x/H = 0.077$. This is due to limitation of the traverse of the thermocouple rake mechanism. Although the variation in B_0, B_2 and θ exhibit a trend very similar to the previous works, it can be observed that the volume fraction profile close to the splitter plate indicates a wider mixing layer. As the thickness of the splitter plate is reduced in comparison with previous Water Channel setup, the increased mixing width at early-time could be attributed to larger Atwood number in the current experiments or greater inherent wavelengths of the setup due to the modified setup.

Figures B.1(a) and B.1(b) show the variation of volume fraction of heavy fluid, f_h with crosswise displacement, y. As the current experiments are characterized by a greater Atwood number, molecular mixing is greater due to a stronger density gradient that drives the mixing. It can be observed from the plots that f_h satisfies its boundary conditions far from the interface at $y \approx 0$, i.e. $f_h = 0$ as $y/H \to -\frac{1}{2}$ and $f_h = 1$ as $y/H \to \frac{1}{2}$ for all cases. It should be noted that along the centerline, the value of f_h is very close to $\frac{1}{2}$. The small discrepancies present could be attributed to the offset in positioning the thermocouple profiler. Non-dimensional density does not attain an exact value of $\frac{1}{2}$ at the streamwise centerline obtained by visual inspection.

---

*Reprinted with permission from "Rayleigh-Taylor experiments" by Kuchibhatla, S. & Ranjan, D., 2013. Proceedings of ASME FEDSM 2012, Copyright 2013 by ASME.

Therefore, a recursive process such as used by Ramaprabhu (2003) is used to set the location of the geometric centerline along Y-direction and ensure f_h is very close to $\frac{1}{2}$ at the mixing centerline. Using this technique, the vertical location of thermocouple corresponding to $f_h = 0.5$ is calculated, and crosswise locations are adjusted with the offset factor. As noted earlier, these Water Channel experiments are considered statistically steady. By selecting hot and cold water temperatures, repeated experiments provide the similar mixing behavior within reasonable experimental uncertainty.

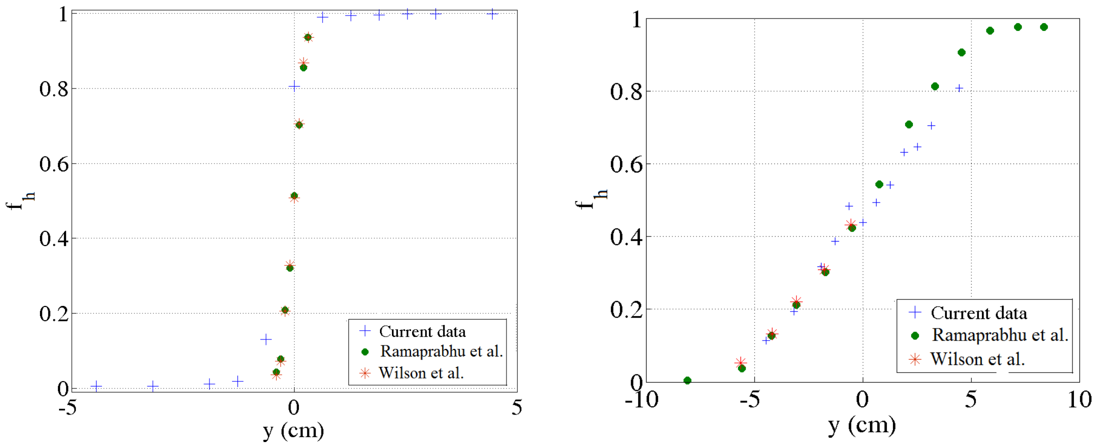

(a) f_h vs. y at $x/H = 0.077$

(b) f_h vs. y at $x/H = 0.908$

Figure B.1: Comparison of volume fraction of heavy fluid, f_h, for case 1. Figure taken from Kuchibhatla & Ranjan (2013b).

The parameter B_0 is a measure of normalized density fluctuations. Plot of B_0 vs. y in Fig. B.2 show that B_0 peaks to a centerline value within the range of 0.06-0.09 at both locations. B_0 decreases with crosswise distance y about the centerline, with a slight skewness about $y \approx 0$. This could be due to the slanting of the thermocouple profiler with the vertical direction (in spite of corrections performed for angle of leaning of profiler with the vertical). Also, B_0 decreases with streamwise distance as

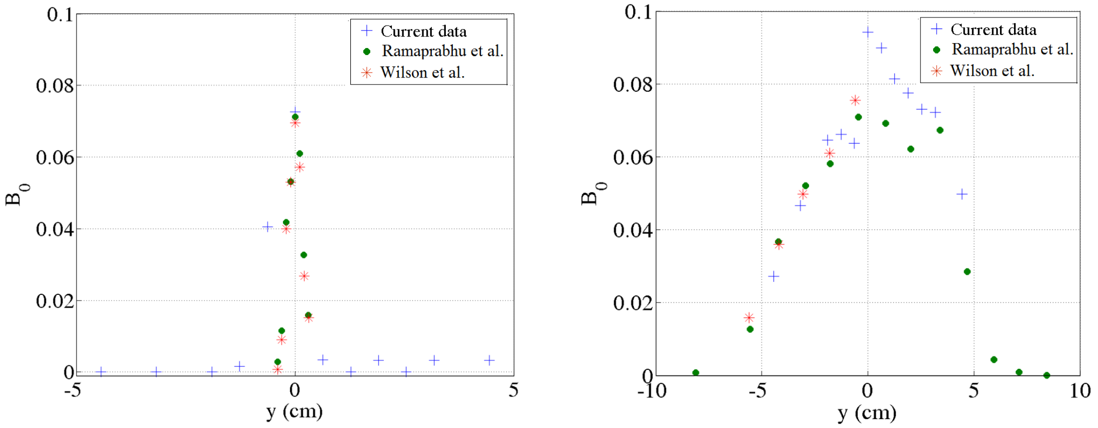

(a) B_0 vs. y at $x/H = 0.077$ (b) B_0 vs. y at $x/H = 0.908$

Figure B.2: Comparison of molecular mixing parameter, B_0, for case 1. Figure taken from Kuchibhatla & Ranjan (2013b).

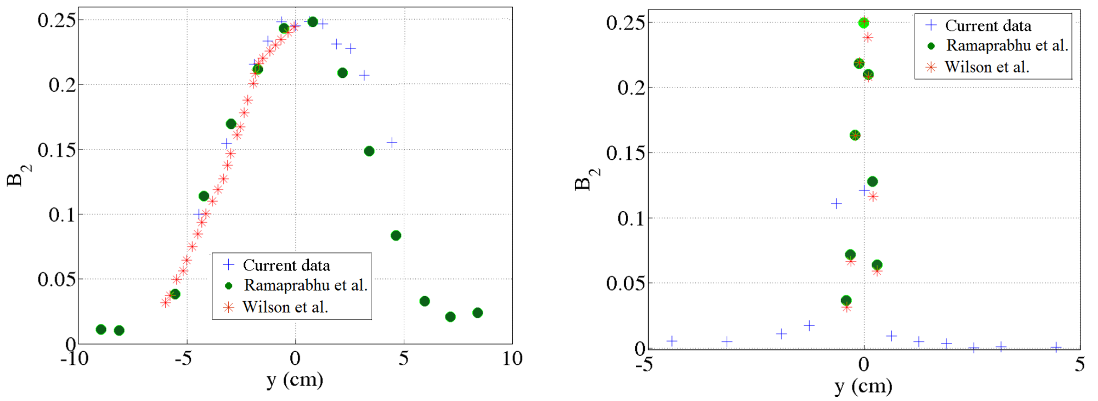

(a) B_2 vs. y at $x/H = 0.077$ (b) B_2 vs. y at $x/H = 0.908$

Figure B.3: Comparison of molecular mixing parameter, B_2, for case 1. Figure taken from Kuchibhatla & Ranjan (2013b).

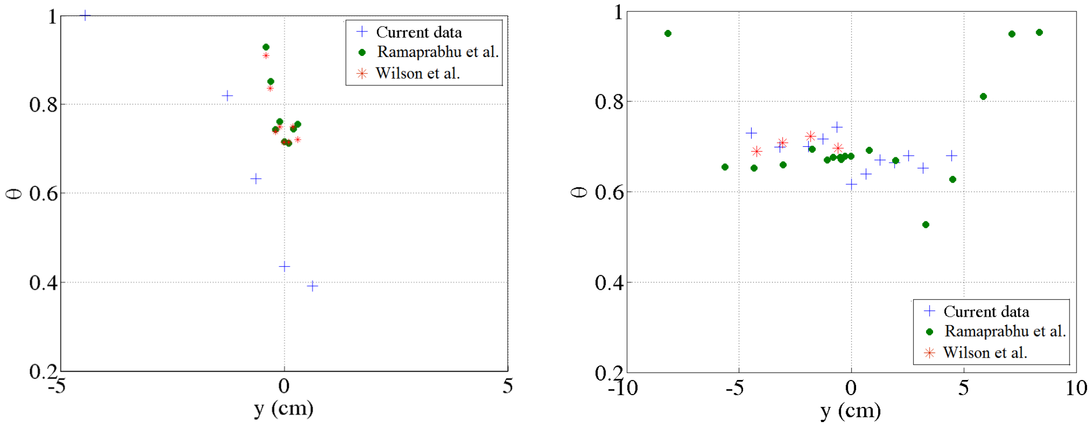

(a) θ vs. y at $x/H = 0.077$

(b) θ vs. y at $x/H = 0.908$

Figure B.4: Comparison of molecular mixing parameter, θ, for case 1. Figure taken from Kuchibhatla & Ranjan (2013b).

the fluctuations are smaller due to reduced density gradients.

Calculated B_2 at the centerline indicates a constant value of $\frac{1}{4}$ for all the cases, as can be seen in Figures B.3(a) and B.3(b). From these plots, a good agreement between the current and previous data can be seen. Variation of θ (given in Figures B.4(a) and B.4(b)) is largely dependent upon B_0, as B_2 remains relatively constant. θ reaches 0 asymptotically as $y/H \to -\frac{1}{2}$ and $\frac{1}{2}$ in pure fluid regions. In the streamwise direction, θ increases due to greater molecular mixing in the core of the mixing layer. This is observed from the spread of the plots of θ with y, for each case. The centerline θ values increase from 0.38 at $x/H = 0.077$ to 0.625 at $x/H = 0.908$.

The beta probability distributions of the first kind for ρ^* at both locations are given in Fig. B.5 for case 10 in Table 4.7. At $x/H = 0.077$, very little molecular mixing has occurred near the centerline and therefore, small peaks are observed around $\rho^* = 0.5$ for the probability curve, whereas at $x/H = 0.908$, the greater mixing width resulted in a broader peak with the greatest probability of density corresponding to a $y = 0$. As y/H approaches $-\frac{1}{2}$ and $\frac{1}{2}$, the unmixed region of the flow dictates greater probability of non-dimensional density at these locations.

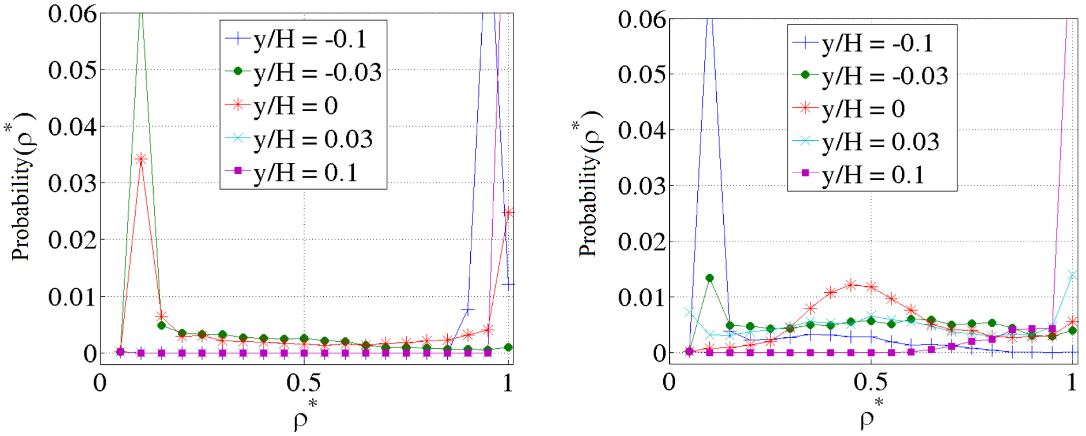

(a) Probability(ρ^*) for different y/H for case 10 at $x/H = 0.077$

(b) Probability(ρ^*) for different y/H for case 10 at $x/H = 0.908$

Figure B.5: Beta probability distributions of ρ^* for case 10.

APPENDIX C

EFFECT OF ATWOOD NUMBER VARIATION

The Water Channel experiments are characterized by low A_t RTI mixing due to a temperature contrast of about 5-8 °C. In order to check the limitations on maximum Atwood number, the temperature contrast is varied between 3-16.5 °C, and ensemble averaged mixing properties are studied. Table C.1 gives the list of parameters for the set of 8 experimental 'cases'. The temperature contrast of each experiment is increased to attain greater Atwood numbers. The cold water temperature depends upon the supply water temperature on the day of the experiment. Figure C.2 gives the hot and cold water temperatures for each case, while Fig. C.3 gives the hot and cold water densities obtained from Eqn. 3.1. Ensemble averaged mixing contours are plotted in Figures C.4 and C.5, showing contour lines of non-dimensional density. These plots indicate that the mixing layer develops faster with A_t, such that it equals the height of the channel at $x = 0.4H$ for case 7. Therefore, the parabolic growth rate regime is not observed for higher A_t, and hence, this can be treated as the upper limit for Water Channel experiments. For cases 7 and 8, the contours also indicate a faint presence of recirculation zones above and below the flapper, which is due to the transient nature of the convective streams of hot and cold water mixing in a channel. This is observed when the hot water stream cannot completely convect the water present in the channel at the beginning of the experiment. Lastly, mixing width obtained from these curves is presented in Figures C.6 and C.7.

The plots clearly indicate that the mixing width increases with A_t, as observed previously. From the plots, a temperature difference, $\Delta T = 11$ °C is the maximum temperature difference, i.e. the limiting Atwood number is $A_t = 1.76 \times 10^{-3}$.

Table C.1: Experimental parameters: Effect of Atwood number variation.

Case #	T_h (°C)	T_l (°C)	ΔT (°C)	ρ_c (gcm^{-3})	ρ_h (gcm^{-3}) ($\times 10^{-3}$)	A_t ($\times 10^{-3}$)	Observation
1	16.25	19.25	3.00	1.0002	999.475	0.386	-
2	17.20	21.80	4.60	1.0000	998.720	0.648	-
3	16.60	22.70	6.10	1.0000	998.432	0.866	Poor image quality
4	20.80	28.50	7.70	0.9990	996.297	1.368	-
5	18.90	27.00	8.10	0.9996	996.895	1.341	-
6	16.60	27.00	11.05	1.0002	996.640	1.765	Recirculation appears
7	16.65	30.05	13.40	1.0002	995.644	2.258	Mixing affected
8	16.65	33.15	16.50	1.0002	994.234	2.967	$y/H = 1$ at $x/H = 0.3$

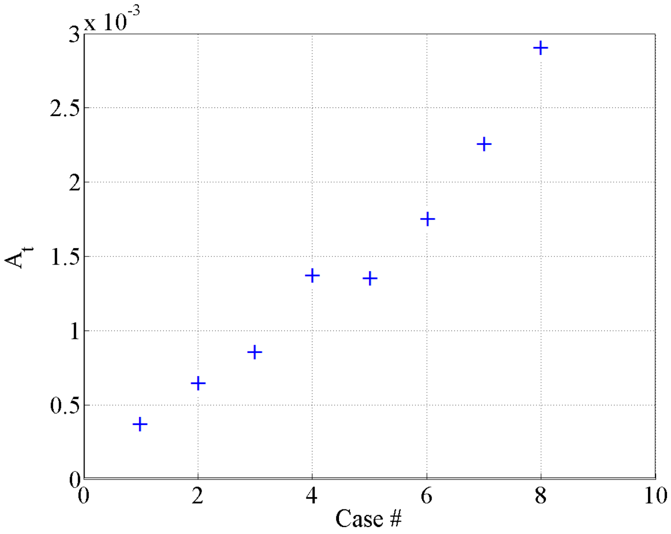

Figure C.1: Casewise Atwood number.

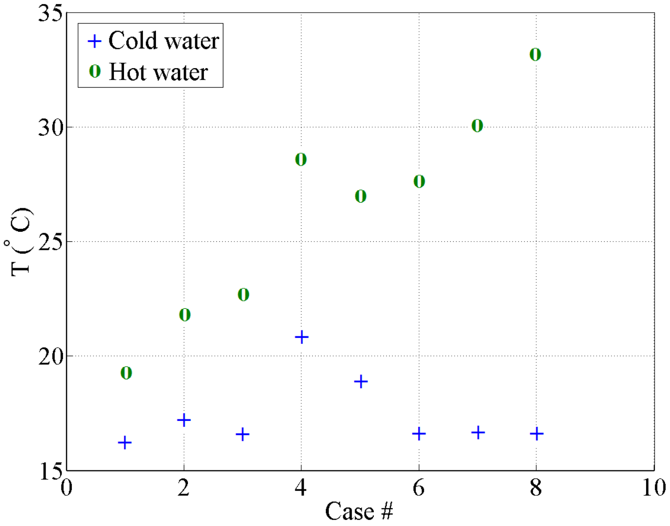

Figure C.2: Casewise hot and cold water temperature.

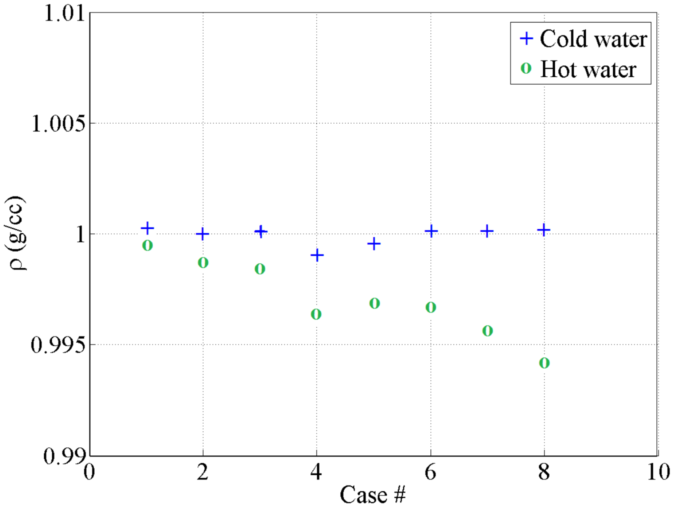

Figure C.3: Casewise hot and cold water density.

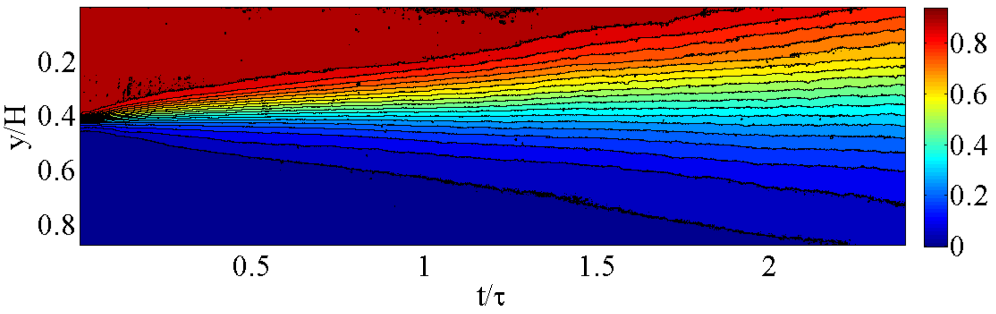

(a) Case 1

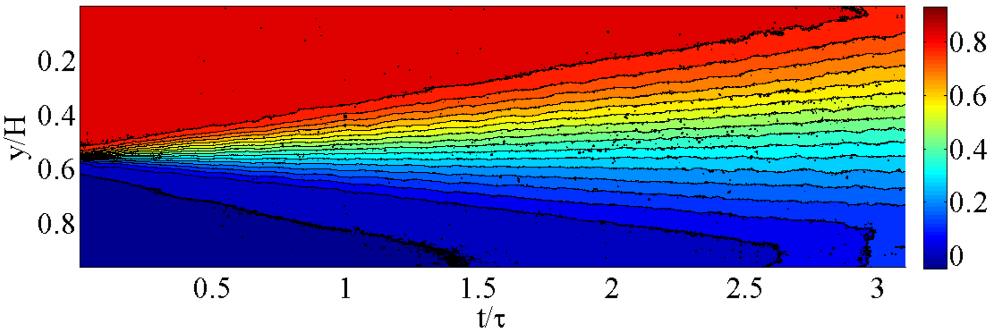

(b) Case 2

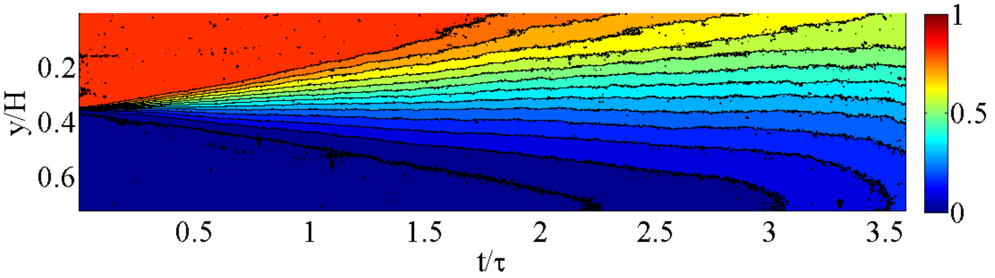

(c) Case 3

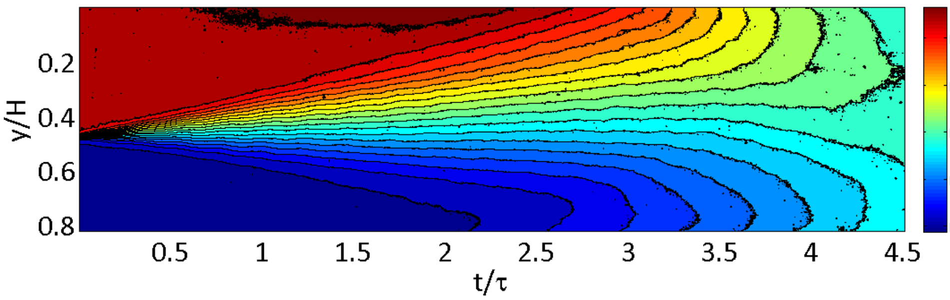

(d) Case 4

Figure C.4: Contour plots of ρ^* from ensemble averaging for cases 1-4.

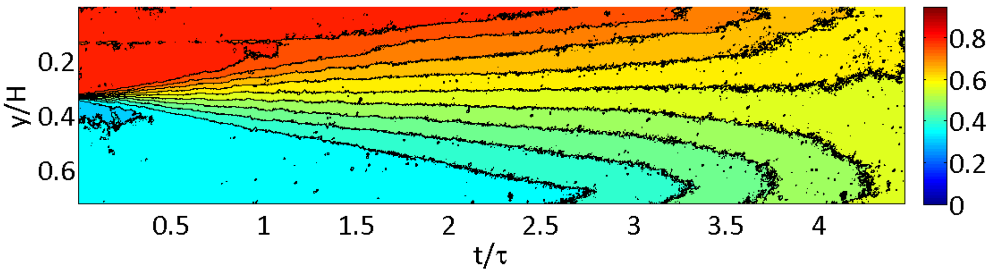

(a) Case 5

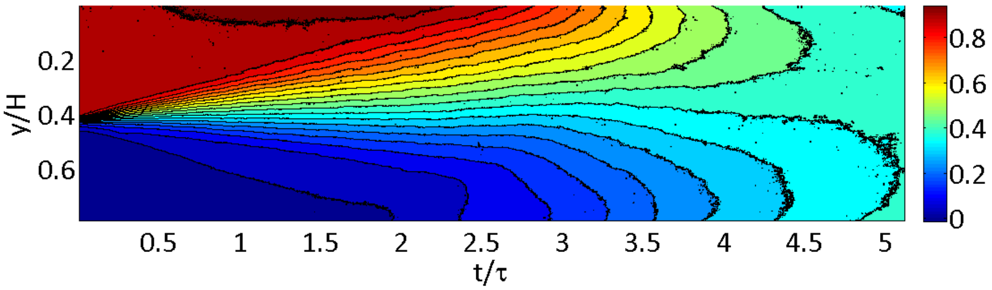

(b) Case 6

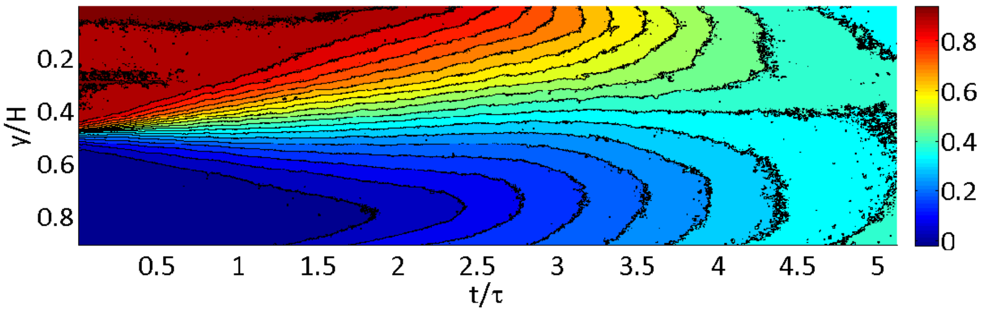

(c) Case 7

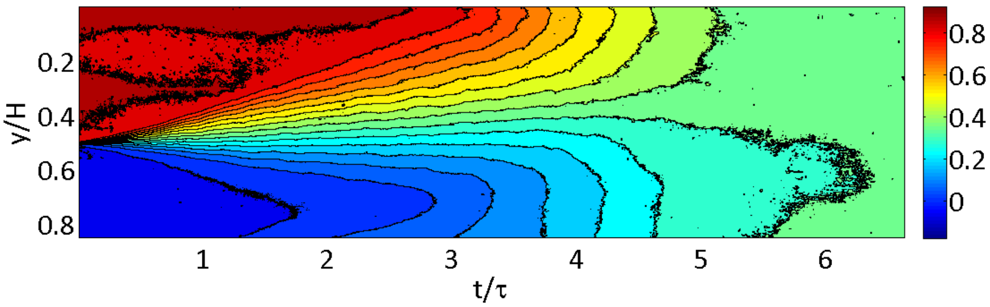

(d) Case8

Figure C.5: Contour plots of ρ^* from ensemble averaging - cases 5-8.

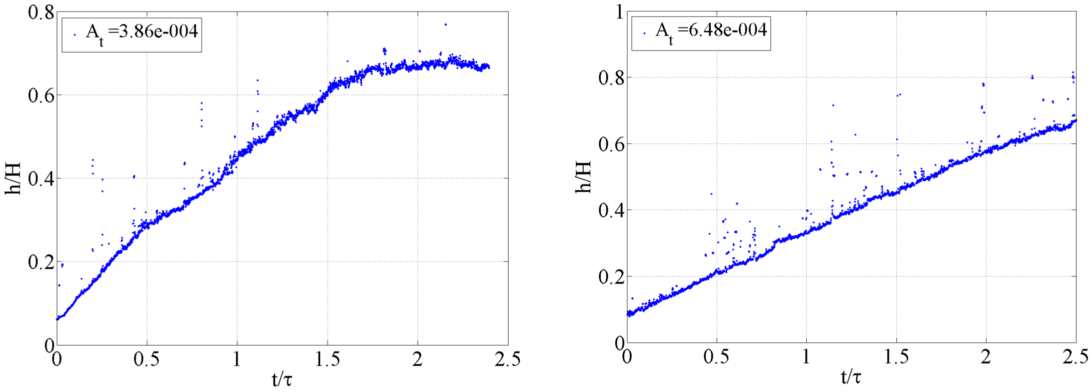

(a) Case 1 (b) Case 2

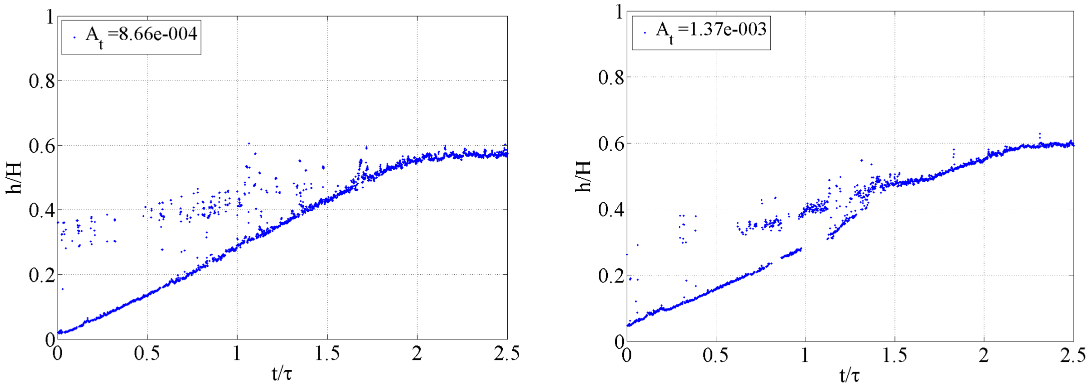

(c) Case 3 (d) Case 4

Figure C.6: Mixing width from ensemble averaging for cases 1-4.

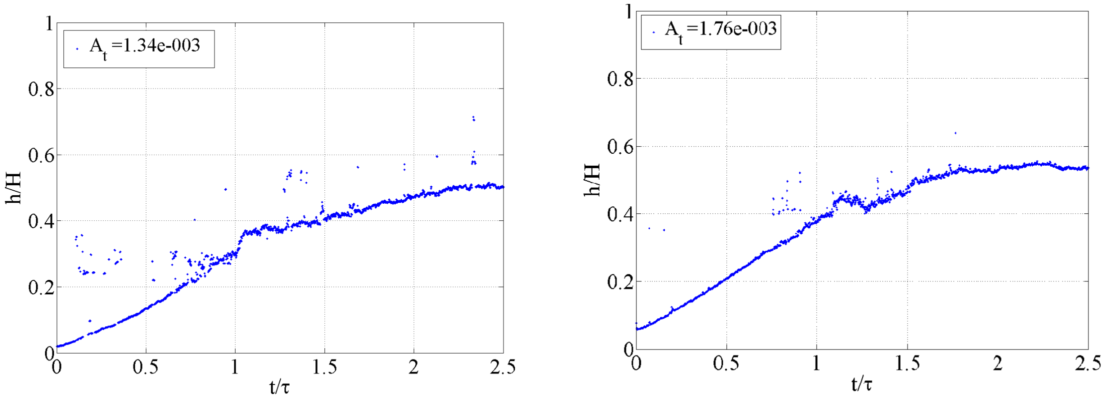

(a) Case 5 (b) Case 6

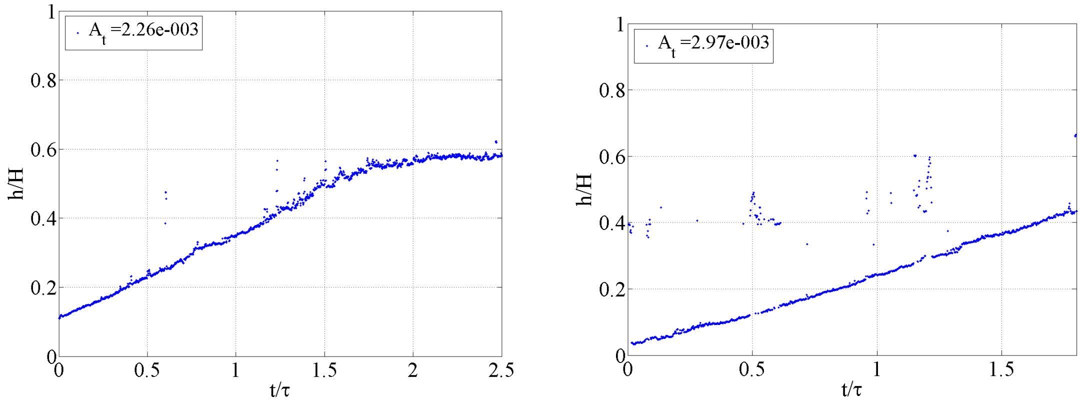

(c) Case 7 (d) Case8

Figure C.7: Mixing width from ensemble averaging for cases 5-8.

To check the presence of linear growth rate regime for cases in this study, an analysis of the ensemble averaged mixing width is performed. Basically, the mixing width is curve fit to an exponential distribution, within the 'linear-time', i.e., corresponding to t^* between 0.05-0.10. This t^* is chosen to be very small compared to the maximum time attained. However, at $t^* = 0$, the mixing width profiles exhibit large fluctuations due to the poor image quality at the edges of the image, as well as non-uniform illumination due to flapper motion. Since, all these cases have a stationary flapper, only the inherent wavelengths of the Water Channel are responsible for the growth of RTI. Some of the significant inherent length-scales include the size of the splitter plate, which is responsible for the wake structures, spacing of the wire meshes used for breaking the boundary layers, and the flow laminators used for breaking down large flow structures to uniform size. Other insignificant scales such as the size of the Water Channel, diameter of the piping, and any pump effects may also be present. Plots of the mixing width in this regime along with the curve fit are shown in Figures C.8 and C.9 respectively. From the plots, the exponential growth rate constant, γ, is calculated and tabulated in Table C.2 for all the cases. γ is obtained from Eqn. C.1 and the plots, and Eqn. C.2 is used to calculate non-dimensional growth rate, γ. The initial wavelength, λ_0 is calculated by Eqn. C.3.

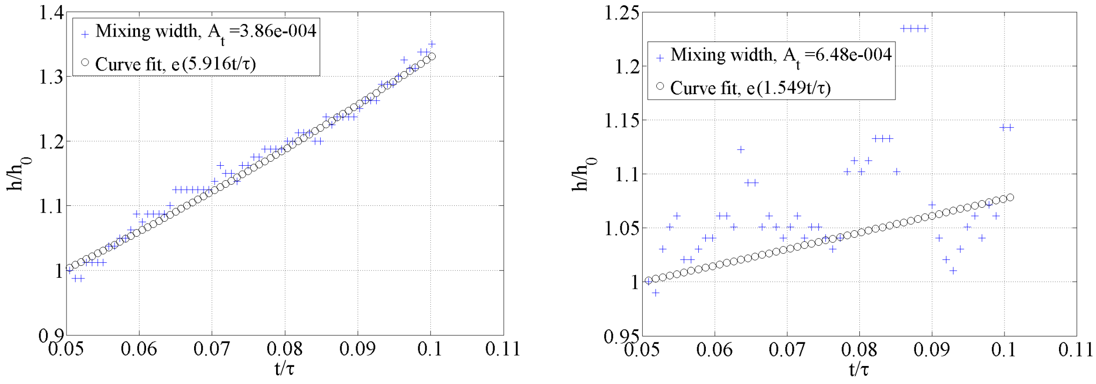

(a) Case 1 (b) Case 2

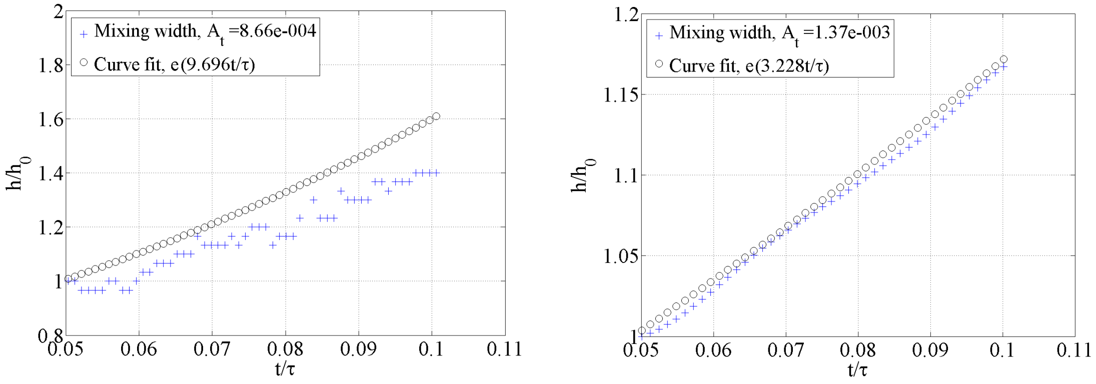

(c) Case 3 (d) Case 4

Figure C.8: Linear growth rates for cases 1-4.

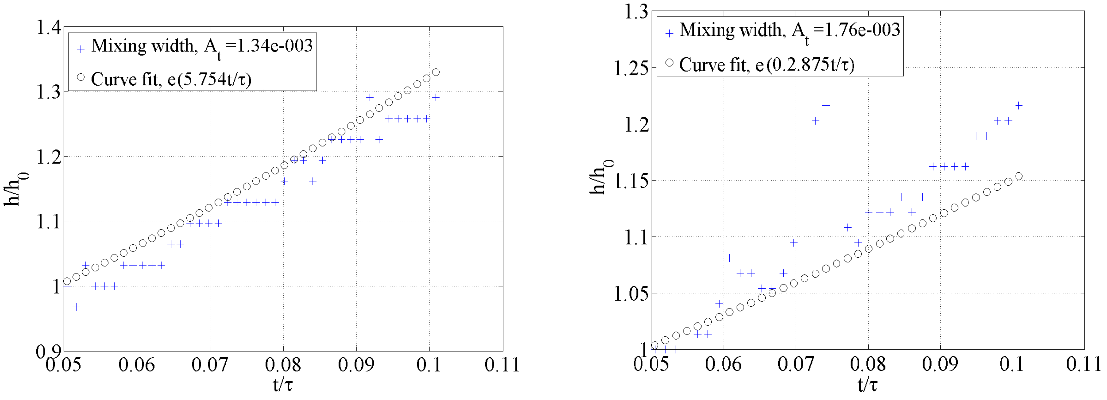

(a) Case 5 (b) Case 6

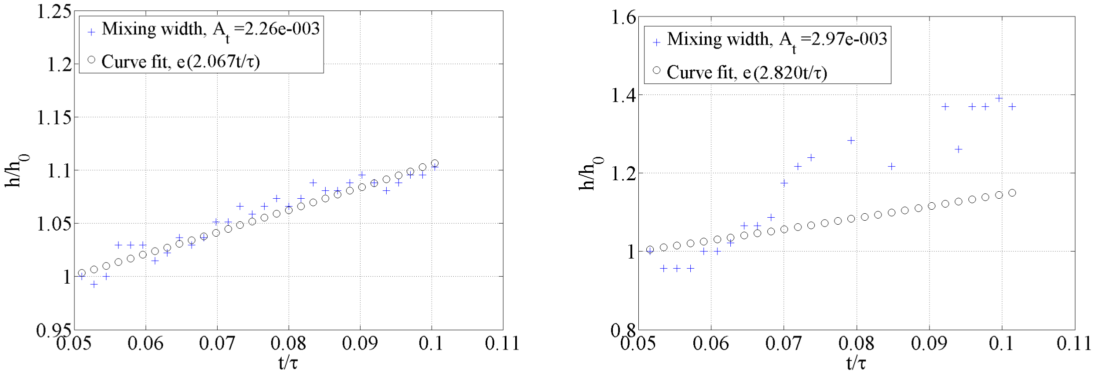

(c) Case 7 (d) Case8

Figure C.9: Linear growth rates for cases 5-8.

$$ln(\frac{h}{h_0}) = e^{\gamma_{fit} t} \tag{C.1}$$

$$\gamma_{nd} = \gamma_{fit} \tau \tag{C.2}$$

$$\lambda_0 = \frac{2\pi A_t g}{\gamma_{fit}^2} \tag{C.3}$$

From these calculations, a great amount of variation in the curve fit method is observed, since there is a large, unrealistic variation in λ_0. Some of the attributed reasons for this discrepancy include *i)* Large fluctuations in the ensemble averaged

Table C.2: Variation of linear growth rate with increasing Atwood number.

Case $\#$	ΔT (°C)	A_t ($\times 10^{-3}$)	γ_{fit} (s^{-1})	γ_{nd}	λ_0 (cm)
1	3.00	0.386	0.646	5.916	5.70
2	4.60	0.648	0.219	1.549	83.14
3	6.10	0.866	1.586	9.696	2.122
4	7.70	1.368	0.664	3.228	19.14
5	8.10	1.341	1.171	5.754	6.02
6	11.05	1.765	0.671	2.875	24.13
7	13.40	2.258	0.546	2.067	46.68
8	16.50	2.967	0.854	2.820	25.07

mixing width: This is caused due to non-uniform backlight, as observed by the presence of sharp lines in the images. These, in turn, result in the curve fit getting inaccurate. Although smoothing functions can be employed to remove outliers, it is difficult to ascertain that only uncertain data points will be removed, given such a wide spread of data and low spatial resolution of the imaging technique. Therefore, caution must be exercised while employing smoothing functions to mixing width data. *ii)* Boundary layer effects: Ensemble averaging of LOS images is always plagued by the boundary layer effects of the side walls of the Water Channel. These layers cause smearing of the flow structures, thereby reducing the sharpness of the fluid interface. This, in turn, results in large uncertainties in the mixing width calculation. *iii)* Three-dimensionality of the flow structures: Due to the presence of flow laminators and meshes, jet like structures are observed in the flow field, resulting in three-dimensional behavior. Under such circumstances, the mixing width growth cannot be assumed to be two-dimensional or in the linear regime. In order to address these uncertainties, use of the PLIF technique, which can address the first two points, is preferred. However, the last source of uncertainty is an artifact of the convective type Water Channel setup, and cannot be completely eliminated.

However, by using thinner meshes and splitter plate, the three-dimensional effects can perhaps be minimized.

From this study, it can be concluded that *a)* A maximum ΔT of about $11.05°C$ is possible in the Water Channel. *b)* Ensemble averaging is useful only for calculation of integral quantities such as integral mixing width, but unsuitable for parameters that are sensitive to local fluctuations, such as the exponential growth constant, γ. *c)* It is best advised to use PLIF technique for density measurement, with the caveat of limited extent of flow field that can be imaged due to restrictions on optical components.

APPENDIX D

LASER SYSTEM SETUP

To setup the laser plane for PLIF or PIV purposes, the following procedure is followed: *i*) The laser system generates a plane, that is generally used for taking images of the flow field in the XY plane, i.e. along the mid-plane of the test section, at different streamwise locations, X. Based on the required plane width, w_{plane}, the selected optics is aligned to give a sharp plane with the least thickness.*ii*) Figure D.1 shows the schematic of the laser plane setup that is implemented. It shows the use of a combination of a spherical convex lens (converging) and a cylindrical plano-concave (diverging) lens to achieve the objective. *iii*) The laser beam of diameter, h_1, passes through a convex lens of focal length, f_1, initially. The beam is then reflected by a plane mirror and passes through the concave lens of focal length, f_2. Finally, a larger planar mirror is used to diverge the beam to the required width, w_{plane}. *iv*) The angle of divergence, θ, of the beam can also be calculated from ray-topics techniques. The formulas used for calculation are given below, while Table D.1 lists typical parameters for the setup:

$$d_{2-1} + d_{2-2} = d_2 \tag{D.1}$$

$$\frac{1}{f_{eq}} = \frac{1}{f_1} + \frac{1}{f_2} - \frac{d_2}{f_1 f_2} \tag{D.2}$$

$$\frac{1}{d_{im-1}} = \frac{1}{f_1} - \frac{1}{d_1} \tag{D.3}$$

$$\frac{1}{M_1} = \frac{h_2}{h_1} = \frac{d_1}{d_{im-1}} \tag{D.4}$$

$$\frac{1}{M_2} = \frac{h_3}{h_2} = \frac{d_2 - d_{im-1}}{d_{im-2}} \tag{D.5}$$

$$\frac{1}{M_3} = \frac{h_3'}{h_2} = \frac{d_2 - d_{im-1}}{d_3} \tag{D.6}$$

At the mid-plane of the Water Channel, the magnification is

$$\frac{1}{M_3} = \frac{h_3'}{h_2} = \frac{d_2 - d_{im-1}}{d_3 + d - 4} \tag{D.7}$$

The width of the laser plane is given by

$$w_{plane} = \frac{h_2}{M_3} \tag{D.8}$$

Divergence of the laser plane is given by the angle,

$$\theta_{plane} = atan(\frac{w_{plane} - h_3}{d_3 + d_4 - d_{im-2}}) \tag{D.9}$$

Finally, the thickness of the laser plane is equal to the circular beam diameter of the image generated by converging lens.

$$t_{plane} = h_2 \tag{D.10}$$

At all times, $h_1 \ll 2.54$ cm, which is the diameter of mirror 1, while $h_3 > 5.08$ cm, which is diameter of mirror 2. Here, two possible scenarios exist: *i*) Mirror 2 is placed at focus of lens 2. *ii*) Mirror 2 at any other location away from focus.Scenario 2 is generally used for the system setup.

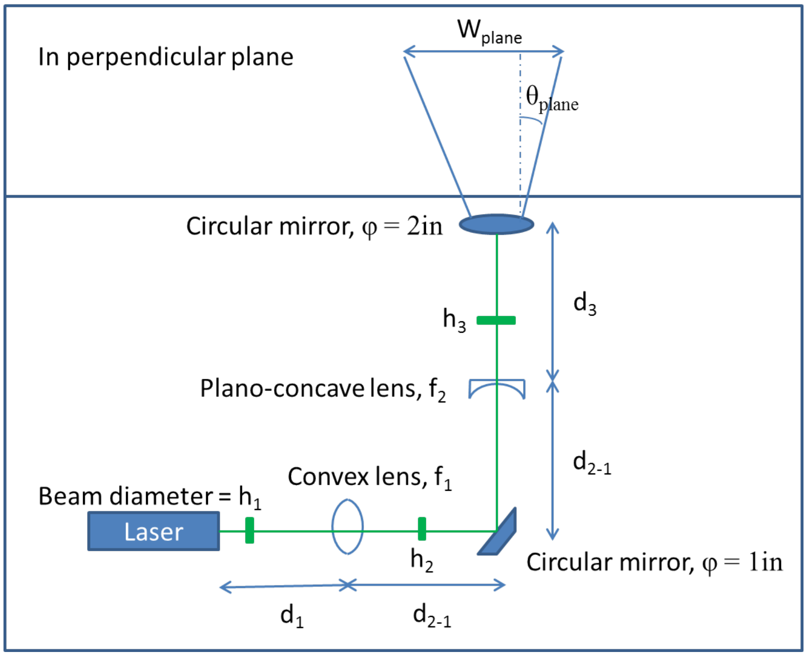

Figure D.1: Laser system setup.

Table D.1: Optical parameters.

f_1 (cm)	f_2 (cm)	d_1 (cm)	d_{2-1} (cm)	d_{2-2} (cm)	d_2 (cm)
2.50	-7.50	26.67	25.40	0.00	25.40
d_3 (cm)	d_4 (cm)	h_1 (cm)	h_2 (cm)	h_3 (cm)	$d_{im,1}$ (cm)
11.43	60.00	0.15	1.45	2.85	2.76
$d_{im,2}$ (cm)	M_1	M_2	M_3	w_{plane}	θ_{plane} (°)
-5.63	9.67	1.98	3.15	0.46	-0.90

APPENDIX E

PLIF CALIBRATION

In order to use PLIF diagnostic for quantitative purposes, a calibration procedure that sets the intensity of the pixels from PLIF images to vary linearly with the density of water is required. This is achieved in two parts: *a)* Calibrating the pixel intensity with dye (Rhodamine 6G) concentration, and *b)* Calibrating the dye concentration with non-dimensional density, ρ^*. While it is well established in literature that PLIF provides excellent images for qualitative purposes (see Walker (1987) and Karasso & Mungal (1997)), challenges are posed in implemeting PLIF for density measurement due to the following reasons: *i*) The application of Beer-Lambert's principle for linear variation of light absorption or extinction with dye concentration is valid only for low solute concentrations. *ii*) Although the measurement of passive scalar such as concentration approximates active scalar such as density only in the mean behavior. The higher order statistics might be different for both scalars. Thus, methods that measure temperature of the fluids directly, e.g. thermocouples are preferred. Density can then be extracted from temperatures by correlation. Therefore, the amount of Rhodamine 6G added to the cold water tank is varied between 0.1 g to 0.8 g, and the channel is filled with dyed water. 200 images of the fluorescent laser plane are acquired and the normalized intensity is given in Fig. E.1.

From these contour plots, it can be clearly seen that the amount of dye significantly changes the intensity distribution in the plane of visualization. It should be noted that for all cases here, the laser power is set to a maximum value of 90 mJ per pulse at an operating frequency of 15 Hz. From these contour plots, the averaged intensity along the crosswise direction (note there is no flow in the Channel) and shown in Fig. E.2. From the plots, the attenuation of laser light by dyed water is nonlinear for concentration greater than 0.3 mgl^{-1}, which corresponds to a molarity of 6.3×10^{-12} moll^{-1}. This is different from the attenuation observed in previous measurements by Ferrier et al. (1993), who observed the nonlinear attenuation around 50 μgl^{-1}, which maybe perhaps due to the higher laser power employed in the experiments. Table E.1 lists the parameters for this set of measurements.

Table E.1: PLIF dye calibration parameters.

Case #	Amount of dye (g)	Concentration ($\times10^{-5}$ mgl^{-1})	Molarity ($\times10^{-10}$ moll^{-1})	Attenuation
1	0.1	0.53	1.10	Linear
2	0.3	1.58	3.31	Linear
3	0.4	2.11	4.41	Linear
4	0.55	2.90	6.07	Linear
5	0.57	3.01	6.29	Nonlinear
6	0.65	3.43	7.17	Nonlinear
7	0.75	3.96	8.27	Nonlinear

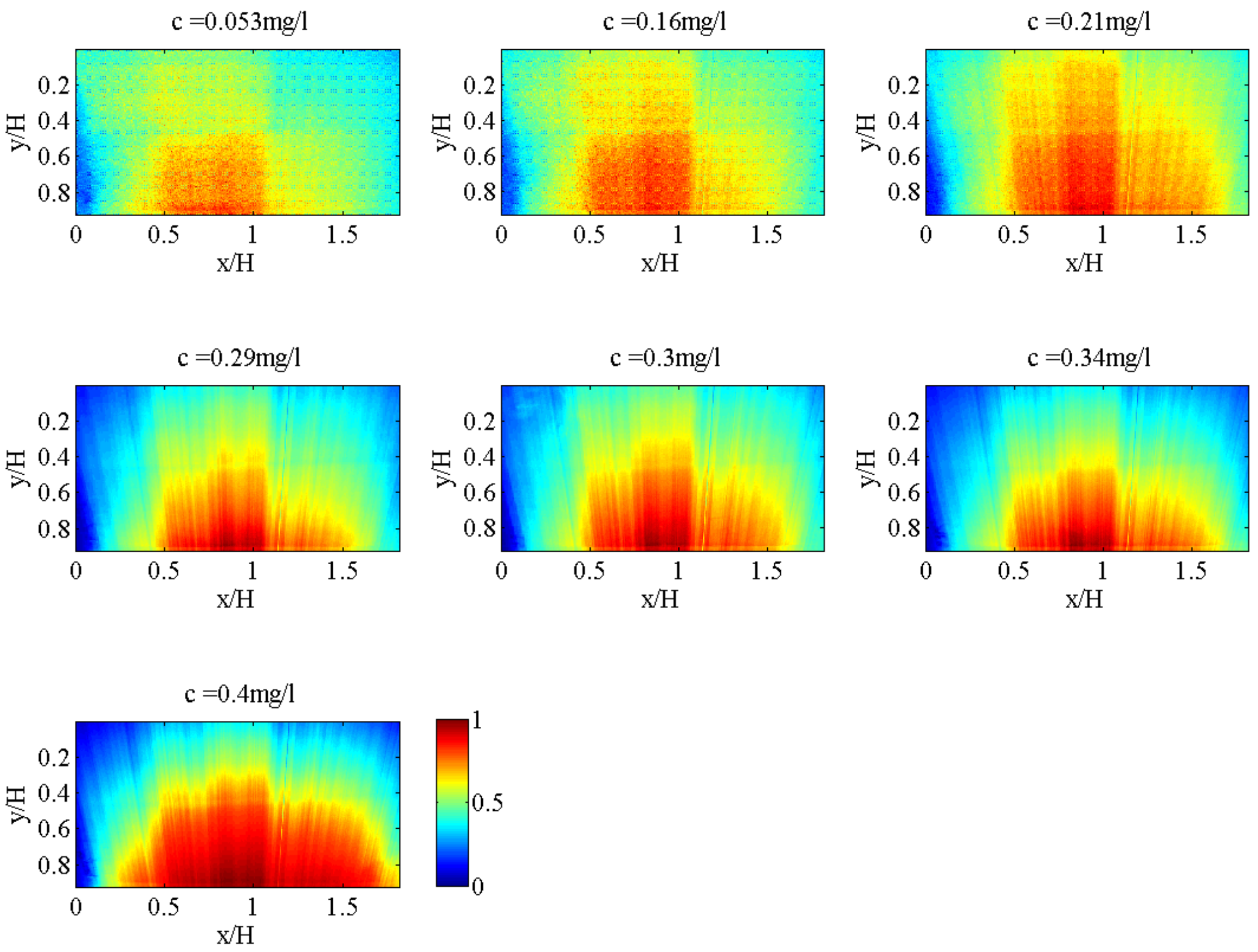

Figure E.1: Images of the illumination plane for different dye concentrations.

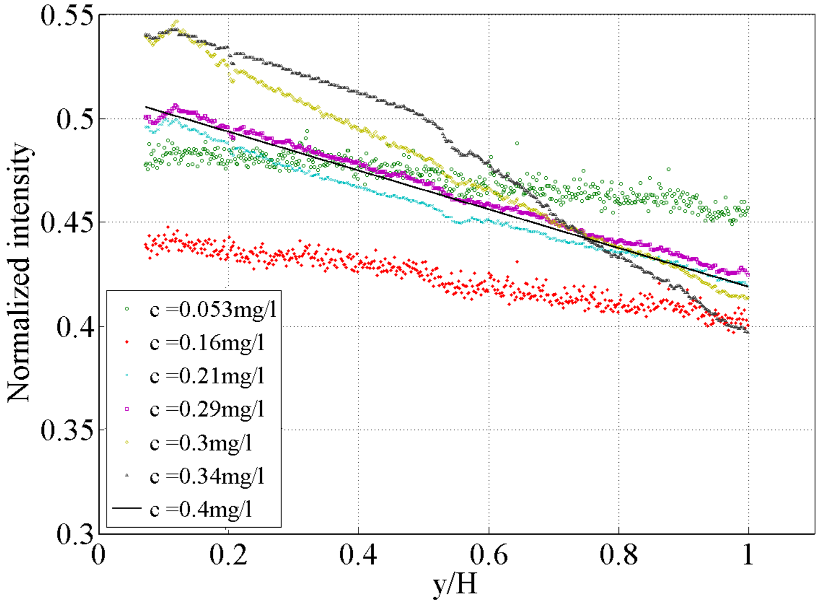

Figure E.2: Plots of intensity vs. y/H for different dye concentrations.

Now that the attenuation of light by concentration is established, about 0.5 g of Rhodamine 6G is used per tank in all experiments listed in §4.5. The variation of pixel intensity in the streamwise direction is plotted in Fig. E.3, which shows a parabolic variation. This variation, when divided by the centerline value to account for the attenuation, collapses all the curves at different y locations to the y averaged curves shown in Fig. E.3. A curve fit to the average is also provided. Here, it must be noted that for dye concentration of 0.3 mgl^{-1}, the curve fit resembles the plot very closely. Thus, it is concluded for all experiments in the study, the use of this curve fit to normalize intensity will account for this non-uniform laser intensity in the visualization plane. The list of experiments for aperture calibration is presented in Table E.2. For all experiments, a camera lens of focal length 50 mm is used.

The source of observed non-uniformity is attributed to the high divergence angle

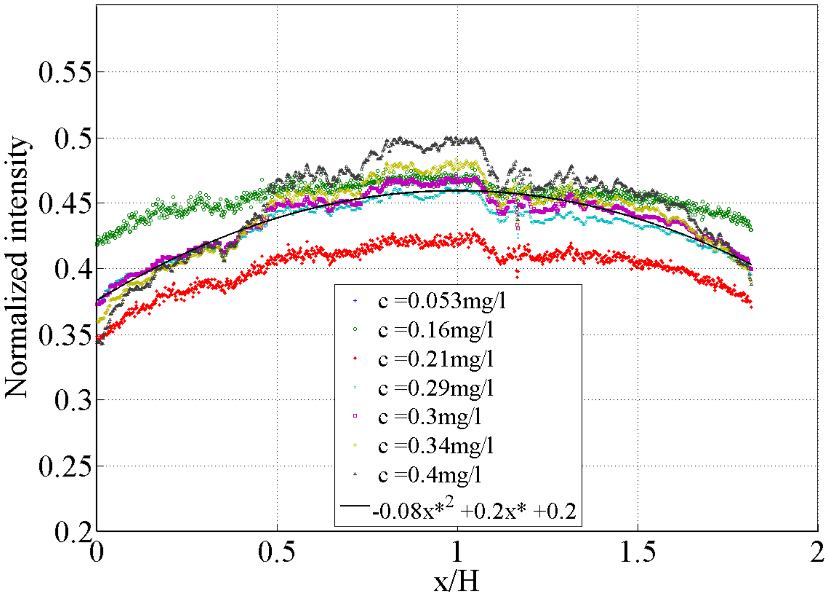

Figure E.3: Plots of intensity vs. x/H for different dye concentrations.

Table E.2: PLIF aperture setting experimental parameters.

Case #	F #	Aperture diameter (mm)	Aperture area (mm^2)	Observations
1	22	0.227	0.162	Too low intensity
2	16	0.312	0.307	Too low intensity
3	11	0.455	0.649	Too low intensity
4	8	0.625	1.227	Too low intensity
5	5.6	0.893	2.504	Optimum
6	4	1.250	4.909	Saturates some images
7	2.8	1.786	3.142	Too high intensity

of the illumination plane, that is required in order to capture most of the flow field for all the experiments. Thus, using a plano-concave lens of high curvature (-8 mm focal length), a non-uniform laser plane is generated. In order to check the effect of aperture settings on the measurements, for the dye concentration of 0.3 mgl^{-1}, 200 images of the plane are taken at different aperture settings and the intensity profiles are recorded, shown in Fig. E.4. From the average intensity profiles shown in Fig. E.5, discerning a trend in the average variation with y is difficult. To get the best dynamic contrast for each image, a setting of f/5.6 is chosen for the experiments. As the aperture diameter increases, the maximum intensity increases, while the variation of intensity profile in the streamwise direction is almost independent of aperture, as can be seen in Fig. E.6. Thus, it is concluded that the high divergence angle of the plane generating lens is responsible for the non-uniform illumination.

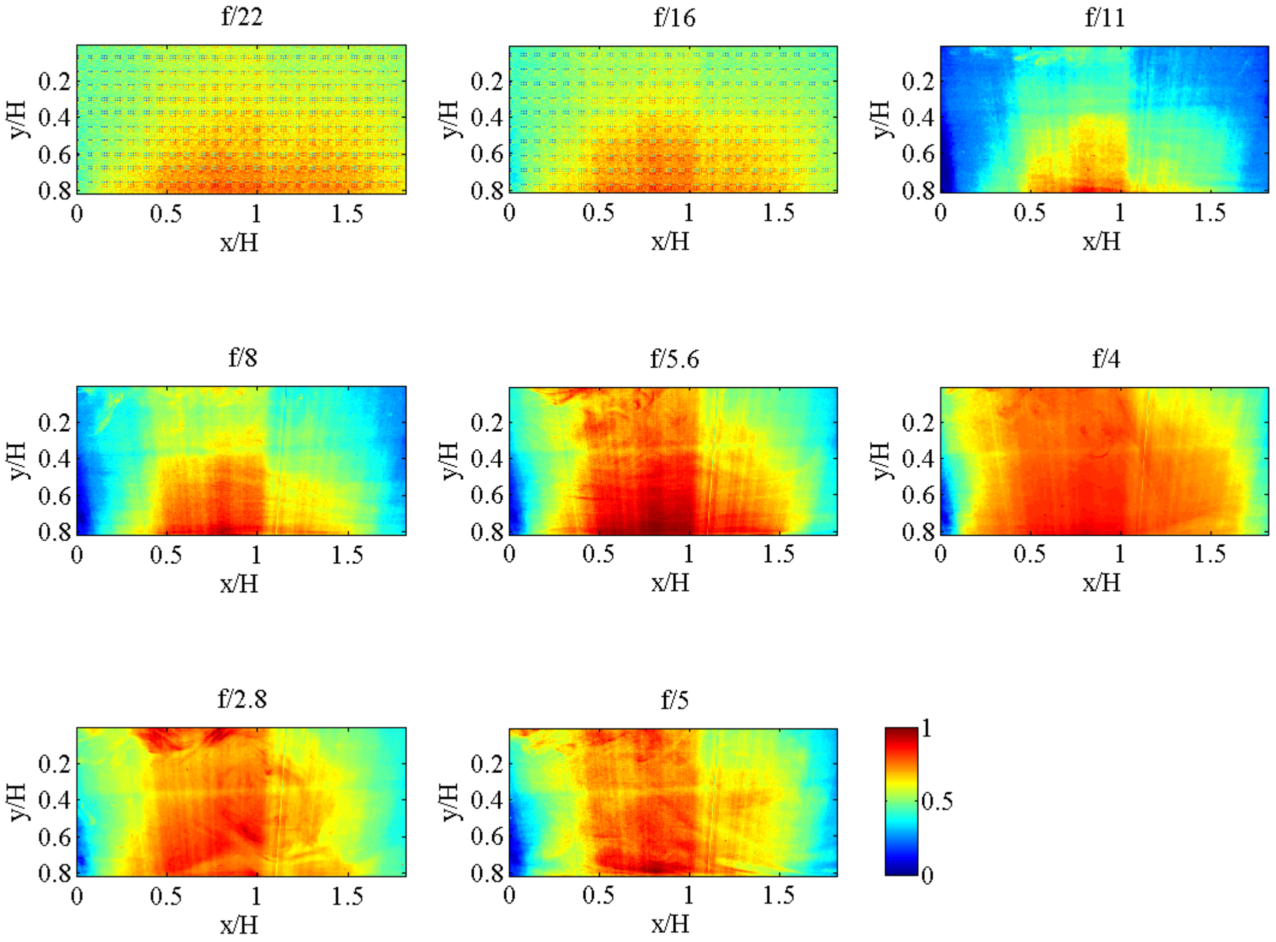

Figure E.4: Images of the illumination plane for different aperture settings.

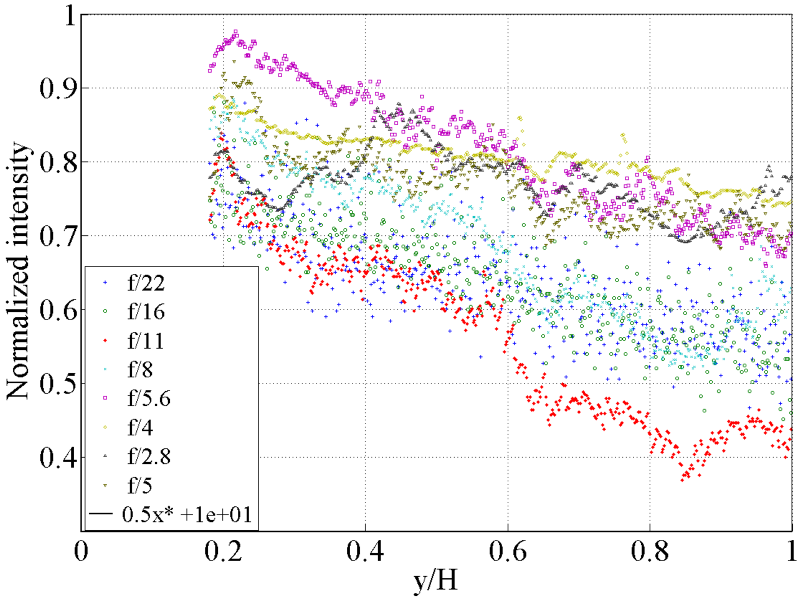

Figure E.5: Plots of intensity vs. y/H for different apertures.

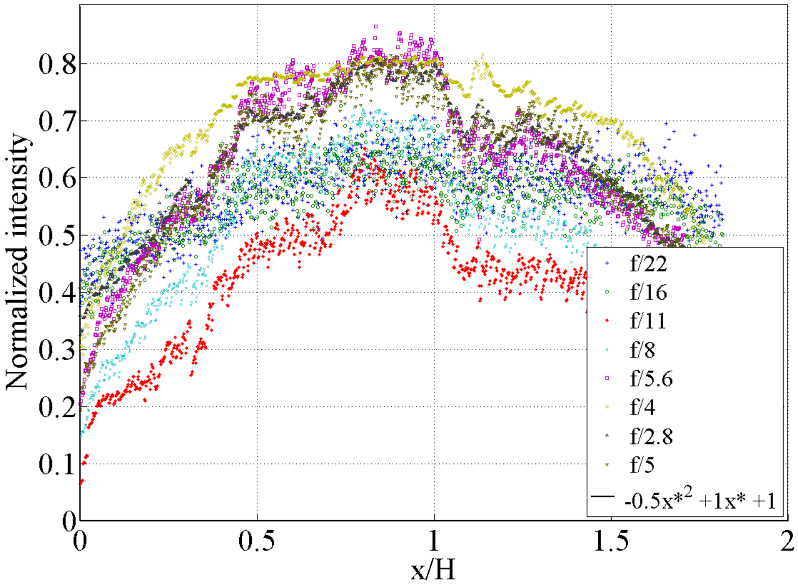

Figure E.6: Plots of intensity vs. x/H for different apertures.

APPENDIX F

PLIF IMAGE CORRECTION

Use of PLIF for density measurements is dependent upon the correction of the RAW images obtained from experiments. While the RAW images obtained using Insight 3G/4G® are obtained in color TIF format, they need to be converted to grayscale for further analysis. Therefore, a correction procedure that takes into account the divergence of the laser plane, nonlinear attenuation of laser light along the height of the Water Channel, removal of vertical striations in images due to varying refractive index of the dyed water within the laser plane *etc.* and dimming of the laser light at left and right the edges of the plane, is listed below:

a) The RAW images (given in Fig. F.1(a)) from Insight are processed for the scalar concentration by selecting a region of interest and masking the remaining region (Fig. F.1(b)). *b)* Using the images of calibration target in a Channel filled with water (Fig. F.1(c)), spatial calibration for the images is performed. *c)* The images are then corrected for absorption by providing dye calibration images (Fig. F.1(d)), which are obtained by filling up the entire channel with dyed water (cold water) and taking the image of the laser plane. This image depicts the nature of the laser attenuation as well as absorption and blurring at the edges. It is interesting to note that this image will not have any vertical striations, therefore, it can be concluded that striations arise from the varying refractive index of the water within the test section. *d)* TSI Insight is used to process the concentration images and correct for dye attenuation. However, the divergence of the laser plane is not accounted for. *e)* Using a software package ImageJ®, the shot or speckle noise in the images is removed (Fig. F.2(a)). *f)* A Matlab® code is developed similar to the procedure adopted by Weber

(2012) that corrects for laser divergence (shown in Fig. F.1 below). *g)* Here, the image is transformed such that the striations become near vertical (Fig. F.2(b)). However, as the source of the laser plane, i.e. the diverging lens, is closer to the test section than in Weber (2012), the striations are not perfectly vertical. This is due to the different angles of incidence of the light into the test section, while Weber (2012) has a large distance between the diverging lens and the test section. Therefore, a procedure using FFTs is not advisable here, as the irregularities do not correspond to either a range of wavenumbers or a range of phase angles. However, by taking the top unmixed layer of the images, a curve is fit to the remainder of the image such that the top layer intensity is uniform in the streamwise direction (Fig. F.2(c)). *h)* Using a 'Haar' wavelet filter provided by Marchal & Mutterer (2005), the images are further cleaned for remaining striations (Fig. F.2(e)), while the removed noise is shown in Fig. F.2(d). The 2D Haar filter can remove Gaussian noise from the images as well. This filter works very well in removing striations in the flow field. *i)* Using a binning procedure is advisable now as all the striations correspond to a greater intensity than the mixing layer. The images are then normalized such that $\rho^* \epsilon$ [0-1], as shown in Fig. F.2(f).

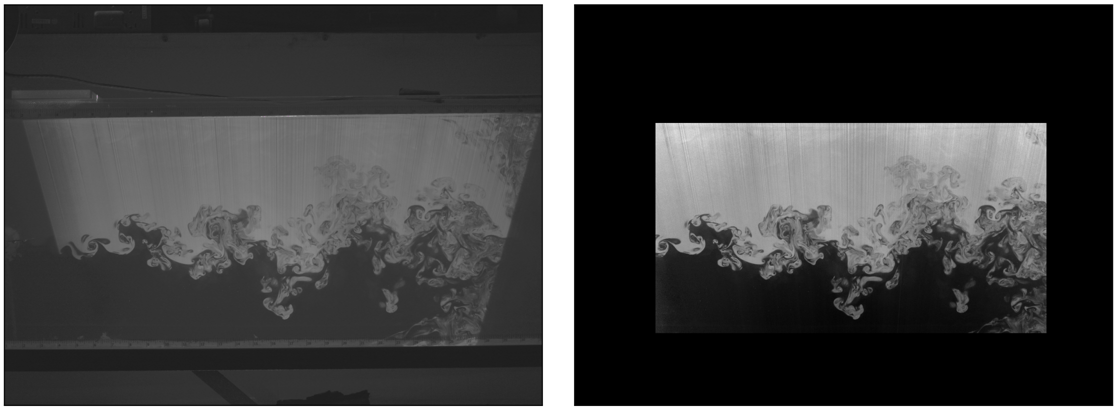

(a) PLIF RAW image

(b) PLIF masked image

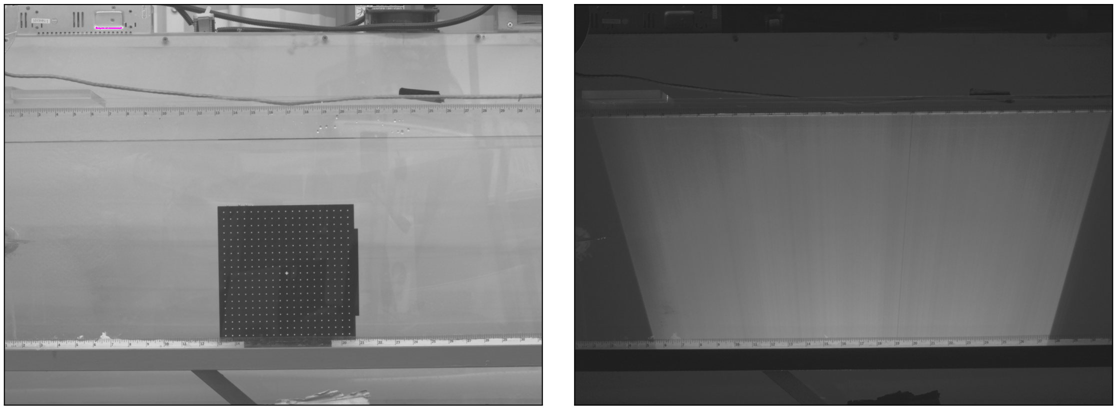

(c) PLIF spatial calibration image

(d) PLIF dye calibration image

Figure F.1: PLIF correction procedure: Part I.

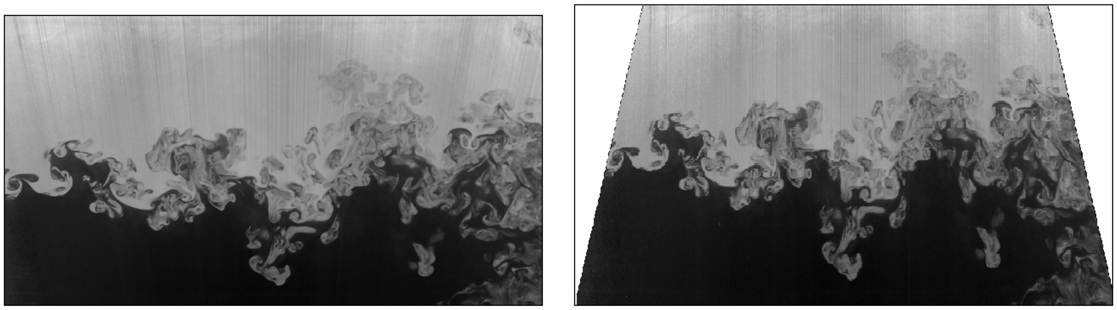

(a) PLIF despeckled image (b) Transformed PLIF image

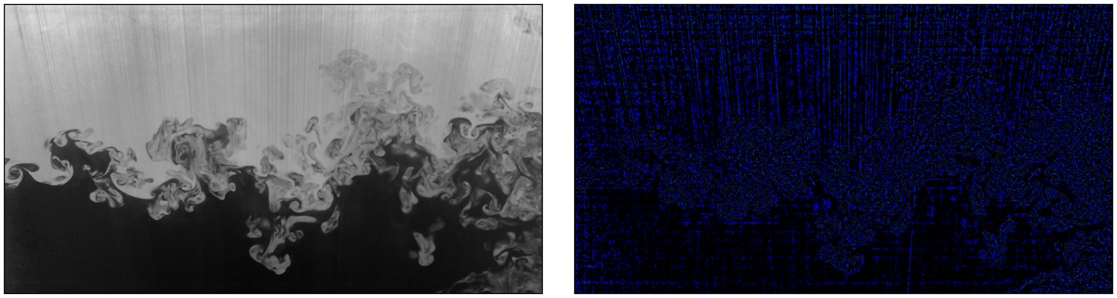

(c) PLIF image after divergence correction (d) Noise from Haar wavelet filter

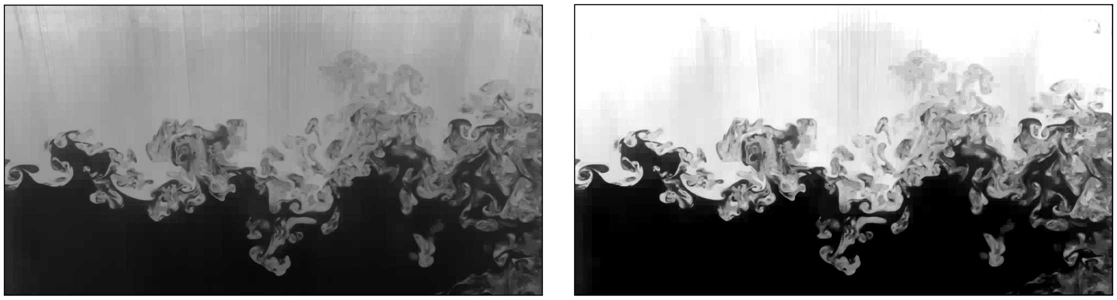

(e) After using Haar wavelet filter (f) Normalized concentration profiles

Figure F.2: PLIF correction procedure: Part II.